UNIVERSITÀ
DEGLI STUDI
DI PADOVA

Host Istitution: Università degli Studi di Padova

Dipartimento di Geoscienze

DOCTORAL COURSE IN EARTH SCIENCES
SERIES XXIX

THE COGNE MAGNETITE DEPOSIT (WESTERN ALPS, ITALY): A LATE JURASSIC SEAFLOOR ULTRAMAFIC-HOSTED HYDROTHERMAL SYSTEM?

Coordinator: Prof. Fabrizio Nestola
Supervisor: Prof. Silvana Martin
Co-Supervisor: Prof. Paolo Nimis

PhD candidate: Luca Toffolo

Table of contents

Abstract

The Cogne magnetite deposit (Western Alps, Italy) is the largest in a series of apatite and sulphide-free magnetite orebodies that are hosted in serpentinites belonging to western Alpine ophiolitic units. The nearly endmember composition of magnetite, which is unusual for an ultramafic setting, and the relatively high tonnage of the deposit ($18 \cdot 10^6$ tons at 45-50 wt% Fe) make Cogne an intriguing case study to explore magnetite-forming processes in ophiolites. The Cogne magnetite shows variable textures, including nodular ores, veins and fine-grained disseminations in serpentinites after mantle peridotites and totally serpentinized melt-impregnated peridotites (troctolites). An increase in Co/Ni ratio from magnetite-poor serpentinized peridotites (0.05) to nodular ores (>1) is observed. Trace element analyses of magnetite from different sites and lithologies by laser-ablation inductively-coupled mass spectrometry indicate that magnetites have typically hydrothermal compositions, characterized by high Mg and Mn (median values up to ~24100 and ~5000 ppm, respectively), and low Cr, Ti and V (median values up to ~30, ~570 and ~60 ppm, respectively). Moreover, the variations in trace element compositions distinguish magnetite that has hydrothermal fluid-controlled composition [highest (Mg, Mn, Co, Zn)/Ni ratios] from magnetite whose composition is affected by host-rock chemistry (highest Ni ± Ti ± V). U-Th-Pb dating of magnetite-associated uraninite constrains the formation of the deposit to the Late Jurassic (ca. 150 Ma), during an advanced stage of the opening of the Alpine Tethys. Thermodynamic modelling of fluid-rock interactions indicates that fluids produced by seawater–peridotite or seawater–Fe-gabbro are not sufficiently Fe-rich to account for the formation of the Cogne deposit. This suggests that fractionation processes such as phase separation were critical to generate hydrothermal fluids capable to precipitate large amounts of magnetite in various types of ultramafic host-rocks. The oceanic setting and geochemical and mineralogical similarities with some modern ultramafic-hosted volcanogenic massive sulphide deposits on mid-ocean ridges suggest that the exposed mineralized section at Cogne may represent

the deep segment of a seafloor, high-temperature (~300–400°C) hydrothermal system. The occurrence of similar magnetite enrichments in present-day oceanic settings could contribute to explain the presence of significant magnetic anomalies centred on active and inactive ultramafic-hosted hydrothermal fields.

1. Introduction

1.1. Motivation and aim of the PhD project

The study of the ophiolites, i.e. fragments of oceanic lithosphere tectonically emplaced in orogenic belts, has been proven a very valuable (and often the only) tool to define and understand a multitude of processes that accompanied the oceanic lithosphere from its early oceanic phase to the following metamorphic stages. The Cogne serpentinite, located in the southern Valle d'Aosta (Western Alps, Italy) and part of the Western Alpine ophiolite, hosts a magnetite ore, which was exploited up to the second half of the XX century. The relatively high-tonnage of the deposit and the nearly endmember composition of magnetite, which is unusual for an ultramafic setting, make Cogne an intriguing and poorly studied example of an ophiolite-hosted magnetite deposit. I considered the specific case of the Cogne deposit to investigate magnetite-forming processes in ophiolites and to establish whether this magnetite ore formed in an oceanic setting or is an effect of alpine metamorphism. Understanding the genesis of the Cogne deposit may have implications for the interpretation of magnetic anomalies reported from modern ultramafic-hosted hydrothermal sites on slow-spreading mid-ocean ridges (Tivey and Dyment, 2010; Szitkar et al., 2014; Fujii et al., 2016).

1.2. Overview of the Cogne magnetite deposit

The Cogne mining district (southern Valle d'Aosta region, Western Alps, Italy; Fig. 1) consists of a set of mines and assays, which exploited a magnetite-rich serpentinite unit from the Middle Ages to 1979. The tonnage of the ore deposit was estimated at 18 Mt (Nazionale "Cogne" S.p.a., 1954), and

the run-of-mine ore produced in the 1960s had an iron grade of 45-50% (Di Colbertaldo et al., 1967). The Cogne deposit is the largest in a series of apatite and sulphide-free serpentinite-hosted magnetite orebodies that crop out in ophiolitic units along the western Alpine collisional suture in Valle d'Aosta (Stella, 1921; Castello, 1981; Diella et al., 1994; Rossetti et al., 2009) and in its southern extension in Corsica (Farinole mine; Routhier, 1963). In southern Valle d'Aosta, most of these magnetite orebodies occur in the Mt. Avic serpentinite massif (located ca. 15 km ENE of the Cogne serpentinite; Fig. 1) and have been interpreted as former metasomatized podiform chromitites, based on their high Cr concentration and the presence of chromite relicts (Diella et al., 1994; Rossetti et al., 2009; Della Giusta et al., 2011). A similar origin has been proposed for analogous Mesozoic (probably Jurassic), ophiolite-hosted magnetite deposits in Greece (Vermion, Olympus and Edessa regions and Skyros island; Paraskevopoulos and Economou, 1980). The Cogne deposit differs from the above occurrences because its magnetite has a nearly pure endmember composition and contains only trace amounts of compatible elements such as Cr, Ti and V (Compagnoni et al., 1981; Carbonin et al., 2014). This geochemical fingerprint, which is unusual for an ultramafic setting, as well as the relatively high tonnage of the deposit, make Cogne an interesting and still poorly studied example of ophiolite-hosted magnetite deposit. Understanding its genesis may have implications for our interpretation of magnetic anomalies reported from modern ultramafic-hosted hydrothermal sites on slow-spreading mid-ocean ridges (Tivey and Dyment, 2010; Szitkar et al., 2014; Fujii et al., 2016).

Several hypotheses have been put forward to explain the genesis of the Cogne deposit. Di Colbertaldo et al. (1967) proposed a genesis by magmatic segregation from an ultramafic melt. Based on the Cr and Ti-poor composition of the magnetite, Compagnoni et al. (1979, 1981) ascribed the formation of the Cogne magnetite to high-temperature serpentinization of oceanic peridotites and consequent Fe mobilization, but they did not discuss this hypothesis in detail. Recently, Carbonin et al. (2014) investigated some of the magnetite-associated lithologies and suggested their possible hydrothermal origin; however, the ore-forming processes were not explored.

1.3. Outline of the work

In this work I will present new petrographic and geochemical data on the Cogne deposit, focusing on the textural relationships between the mineral phases, the compositions of both barren host rocks and magnetite ore, and the trace element content of magnetite. The latter, in fact, can give important hints in the identification of the petrogenetic environment (e.g., Dupuis and Beaudoin, 2011; Boutroy et al., 2014; Dare et al., 2014; Nadoll et al., 2014; Nadoll et al., 2015). To further constrain the environment of formation of the magnetite orebody, I will determine its radiometric age by means of U–Th–Pb dating of uraninite included in magnetite. I will show that the magnetite geochemistry and age support a seafloor oceanic hydrothermal setting for the Cogne deposit, and I will explore the possible formation mechanisms, using constraints from geochemical modelling of seawater-rock reactions.

2. Geology of the Cogne mining area

The Cogne serpentinite is a 2.5 km long sliver, with an average thickness of 100 m (Di Colbertaldo et al., 1967), which is exposed on the S and W slopes of Montzalet (Fig. 1 and 2). The serpentinite is tectonically sandwiched between two different metasedimentary sequences. The foot wall sequence consists of tectonically juxtaposed slivers of calcschists, marbles, dolomitic marbles and quartzites formed in a continental margin and in other palaeogeographic domains (Cogne Unit; Polino et al., 2014). The hanging wall sequence is represented by calcschists, marbles and minor Fe- and Mn-bearing metacherts. The basal contact of the serpentinite is a thrust fault (Elter, 1971), while the upper limit is marked by a few cm- to 3 m-thick boudinaged rodingite, which I tentatively interpret as a tectonically activated, primary serpentinite-sediment interface. According to Elter (1971), the Cogne serpentinite and the hanging wall metasediments form the core of a km-scale isoclinal fold that repeats the Cogne unit in its upper limb (Fig. 2b). The Cogne serpentinite and the hanging wall metasediments are considered to be part of the same greenschist- to blueschist-facies ophiolite-bearing unit (Aouilletta Unit; Polino et al., 2014), which is sandwiched together with the foot wall marbles and quartzites between two eclogite-facies ophiolitic units (Grivola-Urtier Unit and Zermatt-Saas Unit; Dal Piaz et al., 2010). These ophiolitic units are remnants of the Jurassic Piedmont-Liguria ocean (Alpine Tethys; Schmid et al., 2004; Stampfli, 2000). From Late Cretaceous to Eocene, these ophiolitic units followed different P-T paths related to their subduction beneath the Adriatic micro-plate, as a result of Africa-Europe convergence (Schmid et al., 2004). In the Zermatt-Saas Unit (in southern Valle d'Aosta), the high-pressure (eclogitic) metamorphic peak was reached in the Eocene (45-42 Ma; Dal Piaz et al., 2001), contemporaneously with the closure of the ocean (Dal Piaz et al., 2003), and was followed by a greenschist-facies overprint during Late Eocene-Early Oligocene (Dal Piaz et al., 2001, 2003). No P-T-time estimate is available for the Cogne serpentinite and its host Aouilletta Unit.

The Cogne magnetite mineralization is confined to the serpentinite body (Compagnoni et al., 1979; Di Cobertaldo et al., 1967) and it is exposed in three zones, henceforward nominated Site 1, Site 2 and Site 3 (Fig. 2). At Site 1 (which includes the mines of Liconi, 45.612509 N 7.395377 E, Colonna, 45.609716 N 7.391322 E, and Costa del Pino, 45.610466 N 7.378247 E), the orebody is a 50-70 m-thick, 600 m-long continuous lens that dips and wedges out northward (Di Colbertaldo et al., 1967). This orebody was extensively exploited in the second half of the twentieth century by sublevel caving. At Site 2 (western slope of Montzalet, 45.618124 N 7.386316 E) and Site 3 (Larsinaz mine, 45.619119 N 7.377135 E), the intensely mineralized rock volumes are much smaller, and consist of disseminations and veins at Site 2 and of a less than 10 m-thick lens at Site 3 (Stella, 1916). The mineralized serpentinite suffered only low degrees of Alpine deformation and metamorphism (Carbonin et al., 2014), which allowed extensive preservation of the original structures (see below).

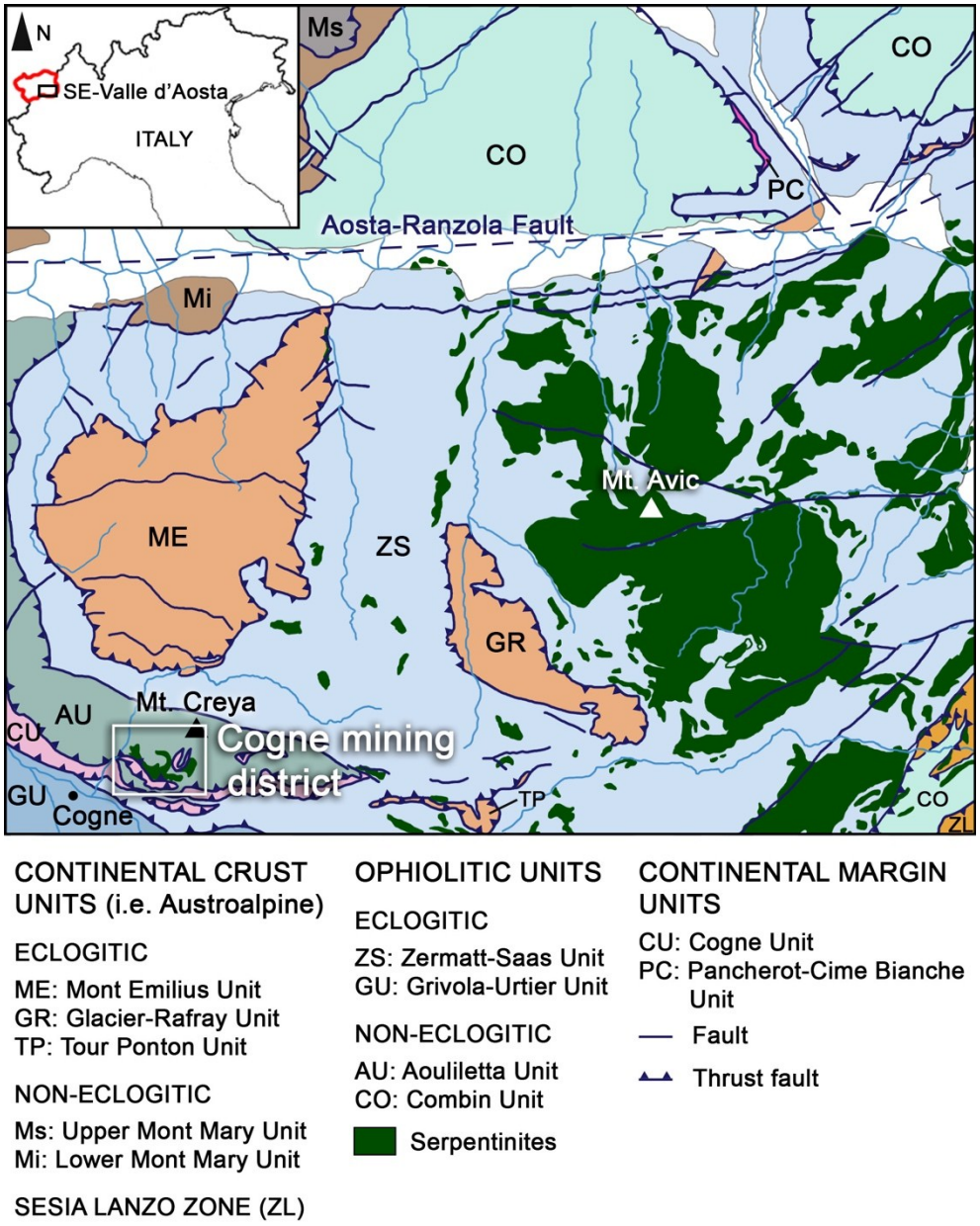

Fig. 1. Geological map of the southern Valle d'Aosta region. Redrawn and modified after De Giusti et al. (2003) and Dal Piaz et al. (2010).

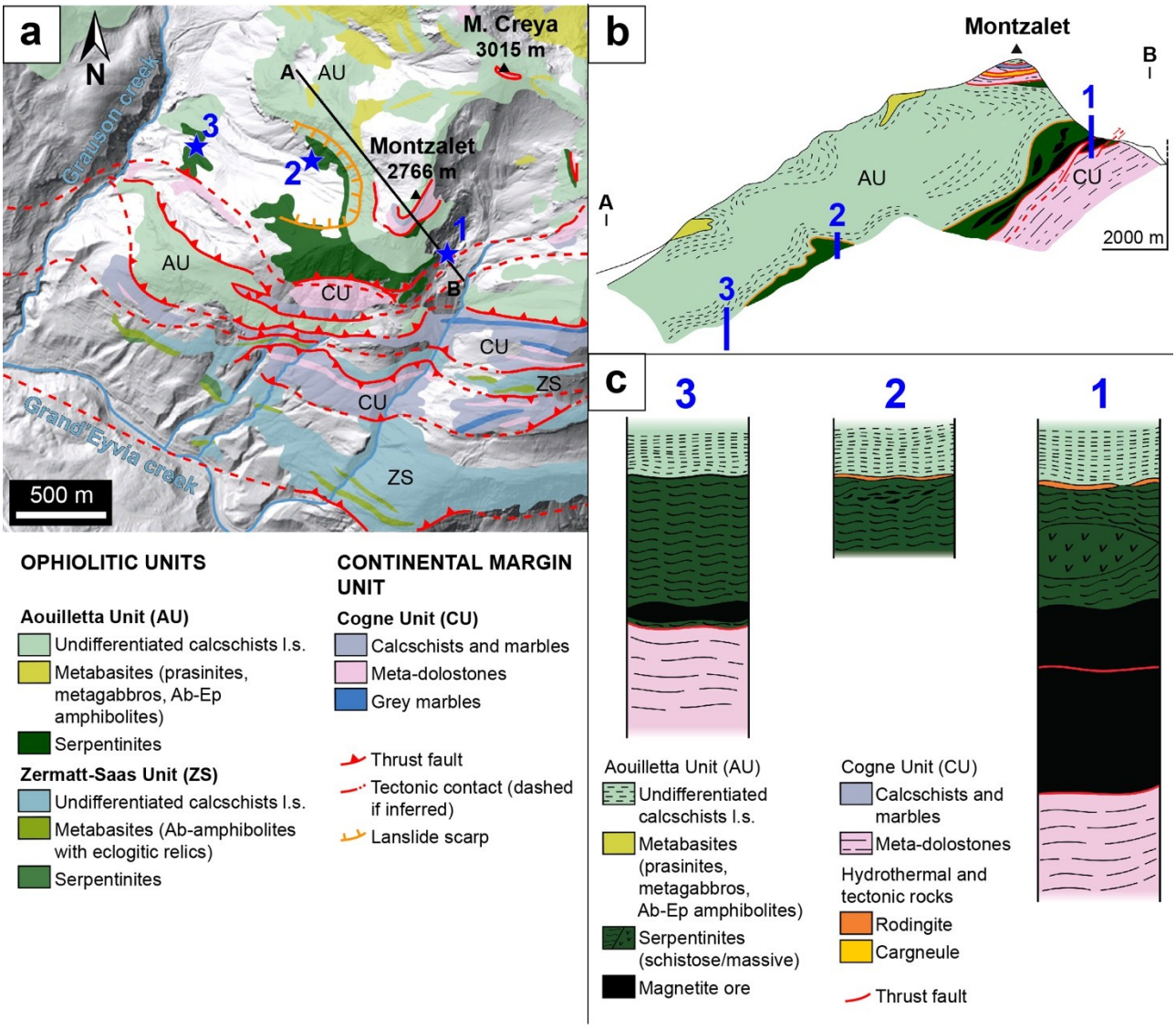

Fig. 2. a) Simplified geologic map of the Cogne mining district depicting the structural relationships between the Cogne serpentinite and the associated units. Numbered stars indicate the sampling sites (see text for details). Units after Dal Piaz et al. (2010); digital terrain map (DTM) from "Agenzia Regionale per la Protezione Ambientale" (ARPA) Piemonte. b) Geological profile through the Cogne serpentinite. Redrawn and modified after Elter (1971). c) Pseudostratigraphic columns of the three sampling sites.

3. Materials and methods

3.1. Rock samples

The rock samples from the Cogne mining area were collected from mine dumps and outcrops. Most of the samples were taken at Site 1, because of the larger extent of the site and the greater inhomogeneity of the lithologies. Most common rock types include magnetite ore and magnetite-poor massive or variably foliated serpentinites. Rare magnetite-rich diopsidites were observed in the Liconi mine dumps and peculiar pegmatoid serpentinites were found along the southern slope of the Montzalet. The rock samples from Site 2 comprise serpentinites, variably enriched in magnetite, and magnetite + chalcopyrite veins. At Site 3, the most common lithologies include the magnetite ore, magnetite-poor massive to foliated serpentinites associated to the magnetite ore and diopside-rich rocks (magnetite-rich diopsidites and diopside-rich magnetite ore). As for Site 1, some of the massive serpentinites exhibit a pegmatoid texture and are variably enriched in magnetite. The complete list of samples is reported in the Appendix.

3.2. Petrographic and mineralogical analysis

Sixty-eight rock samples from the Cogne mining area were collected from mine dumps and outcrops and studied by means of optical microscopy in thin polished sections. No potential source of lead was present during any stage of the sample preparation, to avoid contamination that could invalidate the subsequent geochronological analyses. Mineral identification was aided by micro-Raman spectroscopy, using a Thermo Scientific^{TM} DXR^{TM} confocal Raman system at the Chemistry Department of the University of Padua (Italy). I chose a 532 nm laser working at a power of 5-10

mW. All of the Raman spectra were collected with a 50x LWD objective lens, reaching a spatial resolution of ~1 μm. Raman spectroscopy was crucial for the identification of serpentine minerals, for which I followed the guidelines by Groppo et al. (2006) and Carbonin et al. (2014). Selected samples were further investigated using a scanning electron microscope (SEM). Back-scattered electron (BSE) images were obtained using a CamScan MX 2500 SEM at the Department of Geosciences of the University of Padua (Italy) equipped with a LaB_6 crystal, working at 20 kV accelerating voltage and 140 nA current.

Mineral compositions of major minerals were determined by electron microprobe analysis (EPMA) using a CAMECA SX-50 electron microprobe, equipped with four wavelength-dispersive spectrometers (WDS) and one energy-dispersive spectrometer (EDS), at IGG-CNR, Padua (Italy). The Kα emission lines of ten elements (Na, Mg, Al, Si, K, Ca, Ti, Cr, Mn, Fe) were measured using the following natural and synthetic minerals and oxides as standards: albite (Na), diopside (Si, Ca), orthoclase (K), MgO, Al_2O_3, $MnTiO_3$, Cr_2O_3 and Fe_2O_3. Working conditions were 20 kV, 20 nA, 10 s for peak and 5 s for the background on each side of the peak.

3.3. Bulk rock compositions

Fourteen rock samples, representative of the main lithologies encountered in and around the deposit, were analysed for major, minor and selected trace elements by X-ray fluorescence (XRF). The samples were prepared as fine powder by means of a Retsch M0 agate mortar grinder and a Retsch RS100 vibratory disk mill, equipped with agate disks. The powder samples, fused into beads, were then analysed using a Philips PW2400 XRF wavelength-dispersive sequential spectrometer equipped with a Rh tube at the Department of Geosciences of the University of Padua (Italy). Reference standards were natural geological samples (Govindaraju, 1994). The relative analytical precision is

estimated to within ±0.6% for major and minor elements and within ±3% for trace elements. The relative accuracy is within ±0.5% for Si, ±3% for the other major and minor elements, and ±5% for trace elements. Detection limits are better than 0.01 wt% for Al, Mg and Na, 0.2 wt% for Si and 0.005 wt% for Ti, Fe, Mn, Ca, K and P. For trace elements the detection limits are 3 ppm for Co, Ni, Cu, Zn, Rb, Sr, Y, Zr, Nb, Th, and U, 5 ppm for Sc, V, Ga, and Pb, 6 ppm for Cr, and 10 ppm for Ba, La, Ce, and Nd.

The geochemistry of seven whole-rock samples was further investigated by inductively coupled plasma mass spectrometry and emission spectroscopy (ICP-MS/ES) analyses, which were performed by Bureau Veritas Mineral Laboratories (Canada). The pulverised rock samples were mixed with $LiBO_2/Li_2B_4O_7$ flux and fused. The cooled beads were then digested with ACS grade nitric acid. The detection limits for trace elements are: 1 ppm for Be, Sc, Sn, and Ba; 8 ppm for V; 14 ppm for Cr; 0.2 ppm for Co and Th; 20 ppm for Ni; 0.5 ppm for Ga, Sr and W; 0.1 ppm for Y, Zr, Nb, Cs, Hf, Ta, U, La, Ce; 0.3 ppm for Nd.

3.4. U-Th-Pb dating

Thirteen thin sections of magnetite ore were scanned for uraninite crystals by SEM-BSE imaging. Four of these samples showed uraninite grains of sufficient size to allow their chemical analysis by EPMA and successive dating by the U-Th-Pb method. Uraninite compositions were measured at the Department of Earth Sciences of the University of Milan (Italy), using a JEOL JXA-8200 electron microprobe equipped with five WDS and one EDS spectrometers. An accelerating voltage of 15 kV and a beam current intensity of 20 nA were used. Nine elements were measured by WDS spectrometry using the following X-ray lines: Mg$K\alpha$, Si$K\alpha$, Ti$K\alpha$, Ca$K\alpha$, Cr$K\alpha$, Fe$K\alpha$, U$M\beta$, Th$M\alpha$ and Pb$M\alpha$. The counting time was 60 s for the peak and 30 s for the background for all analysed elements. The

standards were olivine (Mg), grossular (Si and Ca), ilmenite (Ti), fayalite (Fe), pure Cr and synthetic UO_2, ThO_2 and PbO. Detection limits for elements relevant to geochronology are 290 ppm for U, and 170 ppm for Th and Pb. Relative errors (relative standard errors) of 0.1%, 0.5% and 0.7% for U, Th and Pb concentrations, respectively, were calculated on the basis of 5 repetitions of the same measurement. However, a more realistic minimum relative error for U, Th and Pb concentrations >7500 ppm is 2% (Cocherie and Albarede, 2001).

Chemical maps were preliminarily acquired on the uraninite grains to assess the presence of chemical zoning. In order to collect a significant amount of data, I performed both single spot analyses and automated traverses. The latter method allowed me to obtain a large number of data points, although the proportion of mixed or poor-quality analyses increased. Thus, prior to calculating ages, I excluded the analyses which showed obvious contaminations, low totals or anomalously low Pb contents, if compared to adjacent points in the same traverse.

The possibility of dating uraninite with EPMA was discussed by Bowles (1990) and calculated ages were demonstrated to be accurate and consistent with independent isotopic measurements (Bowles, 2015; Cross et al., 2011). According to Bowles (2015), the best accuracy is obtained for ages from ~2 Ma to 700-1000 Ma: the lower limit is imposed by the EPMA detection limit of Pb and the upper limit is linked to metamictization of the uraninite crystal lattice, which may lead to Pb loss. Meaningful ages are obtained if the initial concentration of non-radiogenic Pb is negligible and the U-Th-Pb system remained closed after uraninite crystallization. The former assumption is considered to hold true because Pb^{2+} is incompatible in the uraninite crystal structure (Alexandre and Kyser, 2005), whereas the latter assumption needs to be assessed by careful sample examination.

The formula used to calculate the age *t* (in years) is (Montel et al., 1996):

$$Pb = 208(Th/232) \cdot [\exp(\lambda^{232} \cdot t) - 1] + 206(U/238.04) \cdot [1 - (^{235}U/^{238}U)] \cdot [\exp(\lambda^{238} \cdot t) - 1] +$$

$$+ 207(U/238.04) \cdot (^{235}U/^{238}U)] \cdot [\exp(\lambda^{235} \cdot t) - 1],$$

where Th and U are the measured concentrations in ppm, λ^{232}, λ^{238}, λ^{235} are the decay constants of ^{232}Th, ^{238}U and ^{235}U, respectively, and $^{235}U/^{238}U$ is the bulk Earth's uranium isotopic ratio. The values used in the calculations are: $\lambda^{232} = 4.9475 \cdot 10^{-11}$ a^{-1} (LeRoux and Glendenin, 1963); $\lambda^{238} = 1.55125 \cdot 10^{-10}$ a^{-1} and $\lambda^{235} = 9.8485 \cdot 10^{-10}$ a^{-1} (Jaffey et al., 1971); $^{235}U/^{238}U = 0.0072559$ (Hiess et al., 2012). To obtain an initial guess of *t* I used the formula (modified from Bowles, 2015):

$t = (1/\lambda^{238}) \cdot \ln (1 + Pb/\{[1 - (^{235}U/^{238}U)] \cdot 206(U/238.04)\})$.

Then the difference between the calculated and the measured values of Pb is minimized by least-squares method, varying *t*. Whenever possible, ages were obtained as weighted averages of several analyses, after outlier rejection based on a modified 2σ set of criteria (Ludwig, 2012). To plot geochronological data and to calculate the average weighted ages, ISOPLOT (v. 3.75) Visual Basic add-in for Excel® (Ludwig 2012) was used. For every weighted age, the software also calculates the associated mean square of weighted deviates (MSWD), which is the ratio of the observed scatter of the datapoints, obtained from the best-fit line, to the expected scatter, calculated from assigned uncertainties and error correlations (Ludwig, 2012). The MSWD gives an indication on the source of the uncertainty in the age determination. In particular, if the MSWD is 2.5 or less, the scatter of the points can be attributed to the sole analytical error, if it is greater than 2.5, the scatter is geological (Rollinson, 1993). In the latter case, it is likely that either different populations of crystals were not recognized or that the assumption of a closed system was violated.

3.5. Trace elements in magnetite

Trace elements in magnetite were measured by laser-ablation inductively-coupled plasma mass spectrometry (LA-ICP-MS) at the Petrology of the Ocean Crust Laboratory, University of Bremen (Germany), using a high-resolution double-focussing ThermoFinnigan Element2, equipped with a

solid state laser with a wavelength of 193 nm (New Wave UP193). Magnetite grains were analysed on standard thin polished sections using a 35 μm laser spot size, a pulse frequency of 5 Hz, an irradiance at the sample of ~1.3 GW/cm^2 and an acquisition time of 60 s, comprehensive of 25 s for background measurement. To avoid any risk of contamination on the surface of the rock section, the zone to be investigated was pre-ablated using two laser pulses with 50 μm spot size. The analysed elements (^{25}Mg, ^{29}Si, ^{43}Ca, ^{47}Ti, ^{51}V, ^{53}Cr, ^{55}Mn, ^{57}Fe, ^{59}Co, ^{60}Ni, ^{66}Zn, ^{90}Zr, ^{98}Mo) were measured in low-resolution mode in order to shorten the acquisition time, although preserving high counts per second (cps). I opted for this configuration to avoid deep ablation pits, thus reducing the probability of hitting inclusions or adjacent minerals. The Fe concentration of magnetite as determined by EPMA was used as an internal standard. External standards (reference materials NIST61, BCR-2G and BHVO) were analysed under the same conditions as the samples every 5 to 9 analyses during the same session, in order to check for possible instrumental drift. Signal files, reporting intensities (cps) vs. time, were inspected for possible heterogeneities related to the presence of inclusions and chemical zoning. Integration of the signal and calculation of concentrations were performed with the GeoPro^{TM} software (CETAC Technologies). Detection limits (DL) were calculated on reference materials using the formula:

$$DL_i = [3\sqrt{2}s_{bkgd}/(\bar{X}_{sgl} - \bar{X}_{bkgd})] \cdot C_i,$$

where i is the ith element, s_{bkgd} is the sample standard deviation of the background (in cps), $\bar{X}_{sgl}$ and $\bar{X}_{bkgd}$ are the average signal and the background (in cps) respectively, and C_i is the concentration (in ppm) of the ith element in the reference materials.

3.5.1. Treatment of geochemical data with robust PCA

The statistical relationships between chemical elements in magnetite were explored with a robust principal component analysis (PCA), using the function "pcaCoDa" in the "robCompositions" library for R software (Templ et al., 2011). Robust PCA was preferred to "classical" PCA because it is less sensible to outliers (it uses minimum covariance determinant rather than the arithmetic mean vector and the sample covariance matrix; Filzmoser et al., 2009; Filzmoser and Hron, 2011).

Robust PCA needs the data matrix to be transformed in isometric log-ratio coordinates (ilr; Filzmoser et al., 2009). Log-ratio transformations have the advantage of freeing the compositional data from the closure effect, by allowing them to vary from $-\infty$ to $+\infty$ (Rollinson, 1993, citing Aitchison, 1986). However, ilr-transformation generates new variables that are combinations of the original ones and that cannot be directly interpretable (Filzmoser et al., 2009). Therefore, to overcome this problem and to visualize the results of robust PCA on ilr-transformed data in terms of the original compositional variables, the scores and the loadings need to be back-transformed to a centred log-ratio (clr) space (Filzmoser et al., 2009). The function pcaCODa carries out by default all these transformations.

3.6. Geochemical modelling

In an attempt to simulate the genesis of the Cogne deposit in a seafloor hydrothermal model system, fluid-rock interactions were modelled with the EQ3/6 (Version 8.0a) software package (Wolery, 2013), using the database compiled by Klein et al. (2009), which contains thermodynamic properties of minerals and solutes in the 0-400°C range at the fixed pressure of 500 bar. These consist of thermodynamic equilibrium constants for aqueous dissociation reactions of aqueous species, gases and minerals calculated with SUPCRT92 software (Johnson et al., 1992). The equilibrium constants are reported for 25°C steps. The database was modified to include revised data for $HCl_{(aq)}$ (Ho et al.,

2001), $NaCl_{(aq)}$ (Ho et al., 1994), $KCl_{(aq)}$ (Ho et al., 2000), $FeCl_{2(aq)}$ and $FeCl^{+}_{(aq)}$ (Ding and Seyfried, 1992). In EQ3/6 the activity coefficients for aqueous species were calculated with the B-dot equation (Wolery, 2013). The modelling procedure, which in the first steps follows that of Klein et al. (2009), is described below and is represented in Fig. 3.

First, 1 kg of modern seawater (Table 1; composition from Klein et al., 2009) is speciated at 25°C and 1 bar. Then, seawater is heated and reacted with 1 g of fresh harzburgite (Table 2) in a closed system to the desired temperature (at P = 500 bar), to simulate a downward fluid path towards the reaction zone (Klein et al., 2009). The chosen pressure of 500 bar simulates conditions at ~2000 m below seafloor, which do not exceed the reported depth of magma chambers fuelling hydrothermal fields on slow-spreading ridges (~3 km; Singh et al., 2006), assuming a 3000-m water column, which is a typical value for modern slow-spreading ridge hydrothermal systems (Edmonds, 2010). All the produced minerals are removed at the end of the run, because in a real fluid pathway they would be left behind by downwelling seawater. A positive effect of this step is to narrow down the f_{O_2} range in following calculations, thus improving the code stability (Wolery and Jarek, 2003). In the successive step, which simulates a reaction zone, 1 kg of the resulting hydrothermal fluid is reacted at 400°C with an increasing amount of either fresh harzburgite or Fe-gabbro (Table 2) in a closed system (Wolery and Jarek, 2003). I chose the temperature of 400°C because it maximizes Fe solubility, which is strongly temperature-dependent (Seyfried et al., 2004), and is also compatible with estimates of fluid temperatures in modern subseafloor reaction zones (T >375°C, Berndt et al., 1989; T ~ 400°C based on the maximum amount of heat that water can carry by buoyancy-driven advection, Jupp and Schultz, 2004 and references therein) and with measured temperatures of modern seafloor vent fluids (e.g., Edmonds, 2010). The reaction path is terminated after the maximum value of dissolved Fe is reached. Finally, the Fe-rich hydrothermal fluid is titrated in a closed system with selected lithologies (Table 2) at 300°C or 400°C, in accordance with the temperature range estimated for hydrothermal mineral assemblages by Carbonin et al. (2014). The equilibrium mineral assemblages and the relative abundances of the phases obtained for different water/rock (W/R) ratios are then compared to those

observed in the natural rocks. The model does not account for solid solutions, hence, by suppressing Fe-Mg exchange in secondary phases, it maximizes the extent of magnetite production.

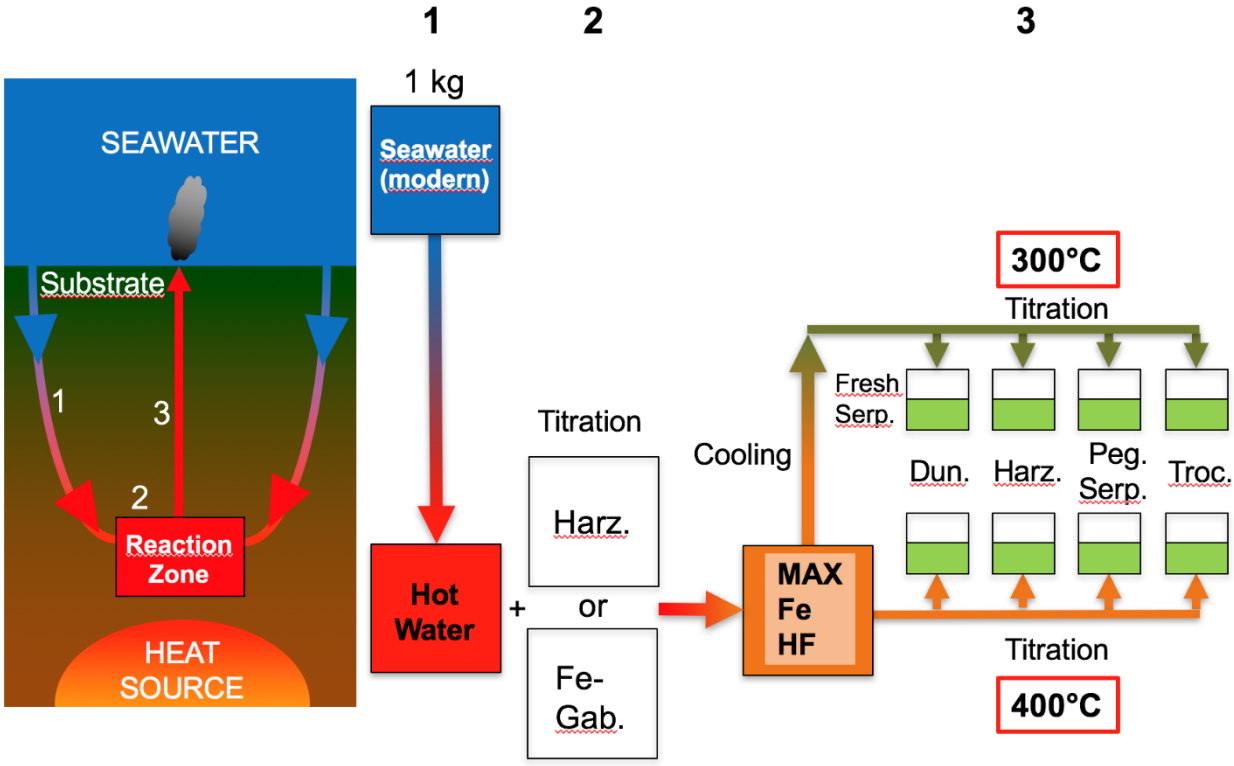

Fig. 3. Model of a seafloor hydrothermal system. 1) Downwelling limb of the hydrothermal convection cell. 2) In the reaction zone, the hot modified seawater reacts with selected lithologies. 3) Upwelling Fe-rich hydrothermal fluids react with a set of fresh and serpentinized substrate rocks at either 300°C or 400°C. See text for details.

Table 1

Seawater composition* (mmol/kg solution)	
Na^{+}	464.0
Cl^{-}	546.0
$HCO3^{-}$	2.34
Ca^{2+}	10.2
Mg^{2+}	53.0
K^{+}	9.8
$SiO_{2(aq)}$	0.11
Fe^{2+}	0.0000015
Al_{3+}	0.000037
SO_4^{2-}	28.2
$O_{2(aq)}$	0.25
pH	7.8

* After Klein et al. (2009).

Table 2

Rock compositions used in thermodynamic modelling.

Rock Type	Fe-gabbro[1]	Dunite[1]	Serp. Dunite[2]	Harzburgite[1]	Serp. Harzburgite[2]	Pegmatoid serpentinite[3]	Troctolite[1]	Serp. Troctolite[4]
Ox. wt%								
SiO_2	47.94	40.87	39.24	44.31	39.38	40.97	42.90	37.95
Al_2O_3	12.19	0.00	0.19	0.42	0.59	0.78	9.58	6.12
FeO	18.87	9.77	7.57	8.97	6.61	9.23	9.06	8.44
MgO	4.85	49.35	38.79	45.81	38.37	37.26	32.39	34.73
CaO	13.17	0.00	0.08	0.48	1.69	0.04	5.39	2.87
Na_2O	2.99	0.00	0.13	0.00	0.05	0.00	0.67	0.41
H_2O	0.00	0.00	13.99	0.00	13.30	11.72	0.00	9.47
Tot.	100.00	100.00	100.00	100.00	100.00	100.00	100.00	100.00

[1] "Artificial" rock.

[2] Andreani et al. (2014).

[3] Sample CDP15, Site 1.

[4] Sanfilippo et al. (2014).

4. Results

4.1. Petrographic features of the magnetite ores and mineral compositions

The Cogne magnetite ore is heterogeneous in terms of both texture and gangue mineral assemblage. Three main textural types of magnetite ore are distinguished, which are termed here *nodular, fine-grained disseminated* and *vein*.

The nodular ores (Fig. 4a, b) are characterized by mm to cm-sized magnetite crystals in a silicate matrix, giving the rock a macroscopic appearance similar to that of nodular chromitites. The nodular textures show a continuum between three major subtypes, which are termed here *leopard*, *harrisitic* and *massive* subtype, respectively. In the leopard subtype, the magnetite crystals, which mostly consist of aggregates of subgrains, are subrounded and constitute up to 50 vol% of the rock. In the harrisitic subtype, the magnetite crystals form up to 10 cm-long rods, mimicking the texture shown by dendritic olivine in harrisite. In the massive subtype, the magnetite content is as high as 80-90 vol%, but subrounded crystals similar to those of the nodular ores are still recognizable.

The fine-grained disseminated ores consist of bands in the host-rock, which contain variable proportions of sub-millimetric magnetite grains (up to ~70 vol%). The vein ores (Fig. 4c) are cm-thick, dismembered veins composed of magnetite, chalcopyrite and antigorite; the proportion of opaque minerals over associated silicates is ~50 vol%.

Since the distribution of the different ore types is not uniform across the deposit, I will treat each sampling site separately.

4.1.1. Site 1

The magnetite orebody lies below magnetite-poor (3-6 vol% Mag) serpentinized harzburgites. The harzburgites show a more or less developed foliation, and are characterized by the presence of lizardite + antigorite + magnetite ± talc pseudomorphs after former olivine and orthopyroxene (distinguished based on the presence of mesh and bastite textures, respectively) and relicts of accessory Mg-Al-rich chromite (Table 3). Magnetite is fine-grained (<20 μm) and Cr-bearing (Carbonin et al., 2014). A detailed description of the mineralogy and conditions of subseafloor serpentinization of these rocks was given in Carbonin et al. (2014; T = 200-300°C, $\log f_{O_2} = -36$ to -30, $\log \Sigma S = -2$ to -1).

Only nodular ores can be found at this site (Fig. 4a, b). Independently of the ore texture, the gangue mineral assemblage is fairly uniform and comprises, in the order of decreasing abundance, antigorite, lizardite, forsterite, brucite, clinochlore, carbonates, and Ti-rich chondrodite (Table 3). Antigorite composes more than 90 vol% of the matrix between the magnetite crystals. It usually shows an interlocking texture (average grain size = 150 μm), but it can form euhedral, randomly oriented blades when in contact with lizardite or magnetite, forming indented crystal boundaries with the latter mineral (Fig. 5a). This feature was already described in rocks from the western Alps by Debret et al. (2014), who interpreted it as a prograde dissolution texture produced during Alpine subduction metamorphism; however, the antigorite studied by Debret et al. (2014) generally has higher Fe content (up to 8 wt% FeO) than antigorite at Cogne (mostly <3 wt% FeO). Lizardite forms yellowish aggregates of submicron-sized crystals, which are interstitial between euhedral antigorite and magnetite. The Al_2O_3 content of lizardite (~5 wt%) is systematically higher than that in antigorite (<1 wt%). Forsterite (Fo_{99}) forms up to 50 μm anhedral crystals, usually arranged into elongated aggregates, which replace and seldom form pseudomorphs after antigorite. The forsterite crystals are often altered to fine-grained antigorite along the rim and the fractures. Brucite is of nearly pure Mg-endmember composition and forms subhedral, tabular crystals up to 200 μm in size. Clinochlore

forms tabular crystals and intergrowths with antigorite. These intergrowths probably result from the breakdown of Al-rich lizardite. The carbonates (calcite, magnesite, dolomite) form anhedral patches which include antigorite, brucite and fine-grained (<50 μm) anhedral magnetite. Calcite is the most common carbonate and is also present as late veins. Ti-rich chondrodite forms up to 500 μm, colourless to pale yellow, anhedral crystals, which are sometimes surrounded by a corona of olivine. Rare accessory minerals are xenotime, sphalerite, Ni-bearing linnaeite, pyrrhotite and uraninite.

Magnetite-rich (~25 vol%) diopsidites have also rarely been found. In these peculiar rocks, magnetite is interstitial between mm- to cm-sized diopside crystals and coexists with antigorite, andradite and clinochlore. The assemblage antigorite + andradite appears to replace diopside. Samples of this kind were thoroughly described by Carbonin et al. (2014).

4.1.2. Site 2

At this site, the serpentinized mantle peridotite can be either replaced by fine-grained magnetite or crosscut by cm-thick magnetite + chalcopyrite + antigorite veins. The disseminated and vein ores are deformed and dismembered into lenses by Alpine deformation, which at small scale results in an anastomosing pattern of mm- to cm-spaced cleavage planes. This deformation is associated with dynamic recrystallization of antigorite and magnetite, the latter forming elongated porphyroclasts.

The disseminations occur as cm-sized bands in antigorite serpentinite and typically show relict features of the former serpentinized peridotite, i.e., bastites (Fig. 5b) and Mg-Al-rich chromite grains (Fig. 5c, d). The Mg-Al-rich chromite grains (Fig. 5d; Table 3) are anhedral and fractured. They are irregularly altered along the rims and fractures into Fe-rich (~41 wt% FeO) chromite ("ferritchromite") + fine-grained Cr-rich (~4–6 wt% Cr_2O_3, determined by SEM-EDS) chlorite and are mantled by a continuous rim of Cr-bearing magnetite intergrown with antigorite and minor secondary diopside.

In the vein ores, magnetite forms elongated, millimetric patches with a chalcopyrite core in an antigorite matrix (Fig. 5e). Magnetite shows well developed crystal boundaries towards chalcopyrite, while the contacts to the surrounding antigorite are irregular. The limit between the vein and the host serpentinite is sharp and is highlighted by a 1-2 mm-thick, magnetite-free band of antigorite that seems to replace massive lizardite in the host serpentinite.

In both disseminations and veins, antigorite shows an interlocking texture. When it is in contact to magnetite or lizardite it forms up to 100 μm-long euhedral lamellar crystals, producing typical indented boundaries. A generation of nearly pure diopside (Table 3) always accompanies magnetite mineralization. In magnetite disseminations, diopside forms up to 400 μm-long isolated needles, intergrown with antigorite (Fig. 5c, d), while in the vein ore, it forms rare aggregates of 10-60 μm long crystals disseminated in the vein selvages. From textural relationships, diopside appears to postdate the formation of bastite pseudomorphs after orthopyroxene in the host serpentinite.

4.1.3. Site 3

At this site, the magnetite ores exhibit nodular textures, but only the leopard and massive subtypes are found. Antigorite is commonly the sole gangue mineral, but the leopard subtype can be characteristically enriched in diopside ± chlorite (Fig. 4d, 4f; Table 3). Antigorite shows an interlocking texture or forms euhedral crystals when in contact to magnetite or diopside. Antigorite veins crosscutting diopside crystals have been observed. Diopside has a nearly pure endmember composition. In the leopard ores, it forms a granofels composed of mm- to cm-sized subhedral crystals, which include subhedral millimetric magnetite. A late generation of smaller subhedral crystals (<50 μm) fills the interstices between larger grains. The diopside crystals may show patchy or concentric oscillatory zoning, determined by slight variations in Fe content. Textural relationships indicate that diopside formed during a late stage of magnetite growth (Fig. 4f), which was then locally overprinted by antigorite. Veins made up of euhedral diopside in a matrix of lizardite ± chlorite are

commonly observed. Clinochlore is found in diopside-rich leopard ores and has variable Mg# ratios and Al contents (Table 3): the Al-rich variety is found as large (up to 1 mm) subhedral tabular crystals associated with diopside and magnetite; the Al-poor clinochlore is fine-grained and fills the interstices between larger clinochlore and diopside crystals and as late veins. Calcite is only found as interstitial material between diopside crystals. Rare accessory minerals are andradite, uraninite, talc and apatite.

4.1.4. Inclusions in magnetite

The magnetite crystals can be rich in mineral inclusions, which, in the largest poikiloblats, are typically concentrated in their cores (Fig. 5a).

At Site 1, the most common inclusions are clinochlore and brucite lamellae (Table 3, often oriented along magnetite (111), anhedral calcite, anhedral sphalerite, rare anhedral pyrite, rare lizardite and forsterite, and very rare euhedral uraninite and apatite. Antigorite inclusions are often present in the outermost zones of the magnetite crystals. Composite inclusions made up of clinochlore + brucite or, rarely, clinochlore + calcite are also observed.

At Site 2, the most abundant inclusions are euhedral antigorite and anhedral sulphides. The sulphides consist of fine lamellar chalcopyrite–cubanite intergrowths and "bornite solid solution" grains, composed of lamellar intergrowths of bornite and chalcocite. Also present are pyrrhotite, which shows exsolution of Co-rich pentlandite, and sphalerite. Other minor included minerals are lamellar clinochlore and anhedral andradite.

At Site 3, the inclusions are mainly composed of clinochlore, which can be associated with rare andradite (Table 3) and very rare diopside and uraninite; antigorite inclusions are only present near the rims of the magnetite crystals.

4.2. Petrography of peculiar host rocks at sites 1 and 3

At sites 1 and 3, serpentinites showing a pegmatoid texture are associated with the magnetite ore and can be variably enriched in magnetite. In the barren rocks (Fig. 4e), cm-sized amoeboid domains made of dominant euhedral coarse-grained (50-300 μm) antigorite that replaces yellow, fine-grained (sub-micron sized) lizardite are interweaved with domains composed of mesh textured antigorite + lizardite and very fine-grained magnetite (magnetite I) lining the rims of the mesh. Lizardite is Al-rich in both domains (Raman peak at 382-385 cm^{-1}, indicating Al substitution for Si in the tetrahedral sites; Groppo et al., 2006). Coronae of interlocking antigorite line the boundaries between the two domains. In magnetite-enriched rocks, the early fine-grained (<30 μm), usually euhedral magnetite (I) associated with Al-rich lizardite (Table 3) is overgrown by a new generation of coarser-grained, subhedral to anhedral magnetite (magnetite II) + euhedral antigorite + lamellar clinochlore. Clinochlore probably forms as consequence of the transformation of Al-rich lizardite to Al-poor antigorite, since its content is proportional to the amount of antigorite that replaces lizardite. The two magnetite generations have similar major element compositions (Table 3). Possible variations in trace element compositions could not be determined because of the small crystal size of magnetite I. Magnetite II can completely replace the lizardite-rich domains, but the amoeboid shape of the domains and the antigorite coronae are usually preserved (Fig. 4f, Fig. 5g, h). On the contrary, the antigorite domains and coronae show only scarce anhedral magnetite (Fig. 5g, h). A magnetite-rich diopsidite, composed of dominant fine-grained diopside (<50 μm), subordinate magnetite and minor euhedral antigorite (<150 μm; Fig. 4f; Tables 3 and 4), has been observed in contact with the magnetite-rich pegmatoid serpentinite.

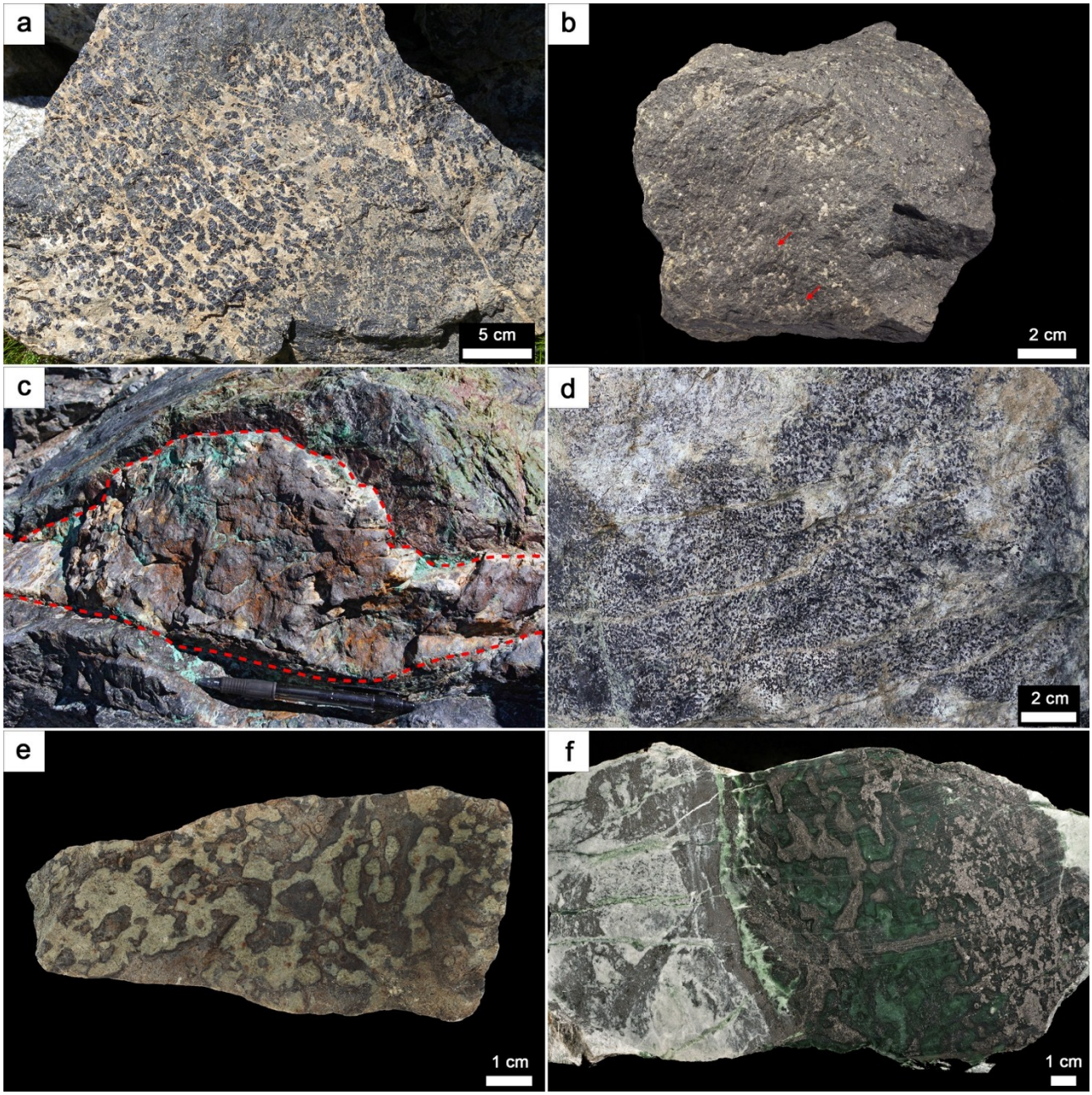

Fig. 4. Typical magnetite ore and rock samples from Site 1 (a, b, e), Site 2 (c) and Site 3 (d, f). a) Nodular ore sample, showing leopard (lower left corner), harristic (cm-sized iso-oriented rods of magnetite in the centre) and massive (upper portion) texture. The light matrix is serpentine (+ brucite + olivine). b) Massive ore, with minor serpentine gangue. Arrows indicate rounded magnetite crystals. c) Deformed magnetite (+ chalcopyrite + antigorite) vein (outlined by dashed lines) in serpentinized peridotite. Chalcopyrite is completely weathered into Fe-oxyhydroxides and secondary copper minerals. The pen is 14 cm-long. d) Fine-grained leopard ore in diopside gangue. e) Magnetite-poor pegmatoid serpentinite. Note the presence of dark and light interlobate domains. The former are composed of antigorite and minor magnetite, the latter are formed by antigorite only.

f) Contact between a magnetite-rich diopsidite (left) and a pegmatoid serpentinite (right) with amoeboid magnetite-rich domains (light grey) interweaved with magnetite-free domains. Dark antigorite coronae contour the two domains. Magnetite content increases in the right part of the sample, but embayed boundaries are still recognizable. Cut and polished sample.

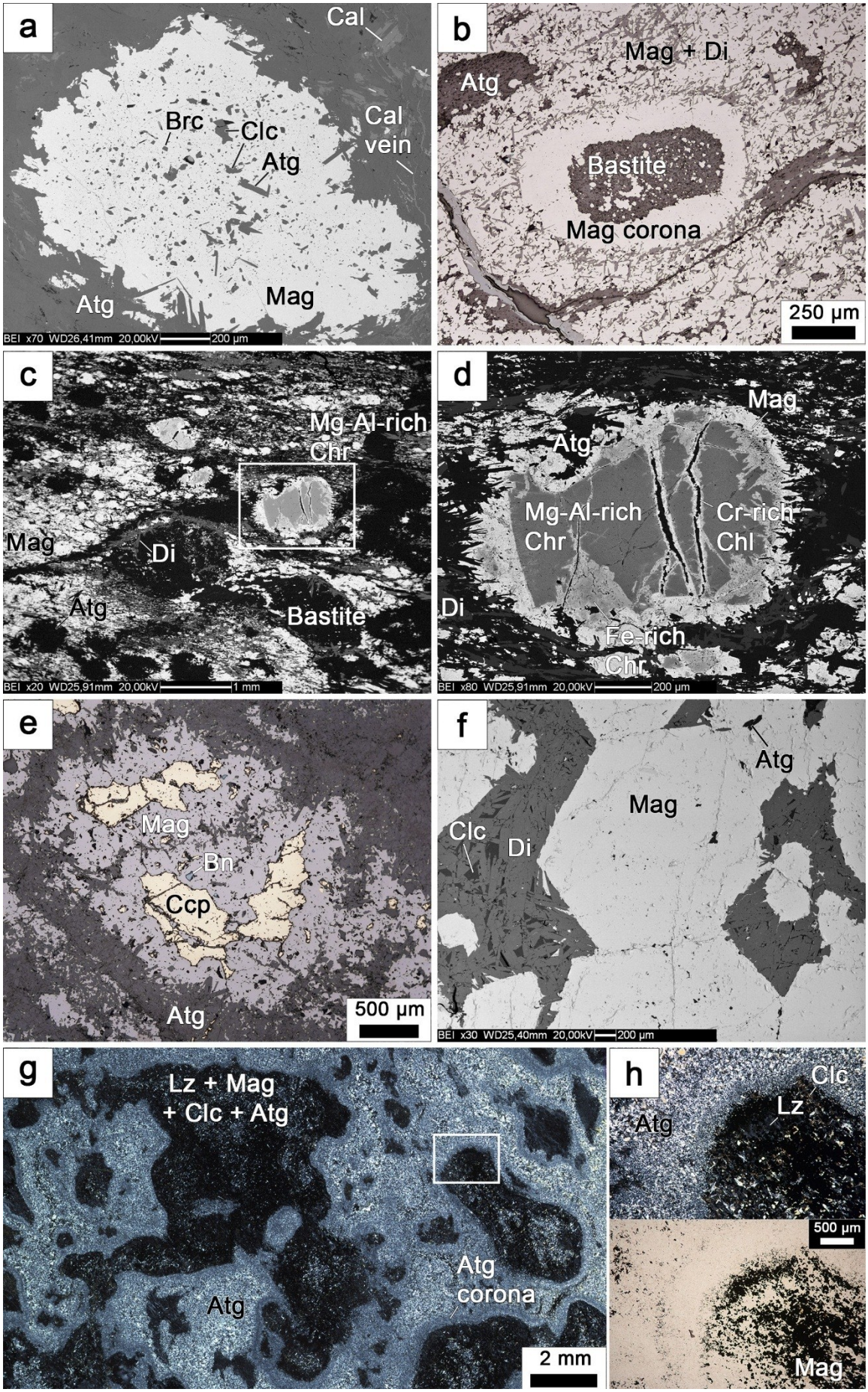
a
Cal
Brc
Clc
Cal vein
Atg
Atg
Mag
BEI x70 WD26,41mm 20,00kV 200 µm
b
Mag + Di
Atg
Bastite
Mag corona
250 µm
c
Mg-Al-rich Chr
Mag
Di
Atg
Bastite
BEI x20 WD25,91mm 20,00kV 1 mm
d
Mag
Atg
Mg-Al-rich Chr
Cr-rich Chl
Di
Fe-rich Chr
BEI x80 WD25,91mm 20,00kV 200 µm
e
Mag
Bn
Ccp
Atg
500 µm
f
Atg
Mag
Clc
Di
BEI x30 WD25,40mm 20,00kV 200 µm
g
Lz + Mag + Clc + Atg
Atg
Atg corona
2 mm
h
Clc
Lz
Atg
500 µm
Mag

Fig. 5. Microstructural features in Cogne rocks. a) Magnetite poikiloblast in leopard ore from Site 1, showing indented boundaries with antigorite. Inclusions in magnetite are clinochlore (usually anhedral), brucite (small and euhedral) and antigorite (large euhedral crystals). Gangue is antigorite with minor calcite, which forms late impregnations and thin veins. SEM-BSE image. b) Nearly massive fine-grained disseminated ore from Site 2. Magnetite (white) is associated with acicular diopside (grey) and forms a corona around an antigorite (dark grey) bastite. Reflected plane-polarized light. c) Fine-grained disseminated ore from Site 2. Magnetite (white), antigorite (black) and diopside (medium grey) replace former silicates, but bastite sites (round black areas) and Mg-Al-rich chromites (framed; see Fig. 5d for a close-up) are still preserved. SEM-BSE image. d) Mg-Al-rich chromite crystal (medium grey), partly altered along the rims and fractures into Fe-rich chromite (light grey) + Cr-rich chlorite (black) and mantled by magnetite, intergrown with antigorite (black) and diopside (dark grey). e) Magnetite + chalcopyrite patch associated with antigorite in a dismembered vein from Site 2. Bluish inclusions in magnetite are bornite. Antigorite occurs both within and around the magnetite, forming indented boundaries with it. Reflected plane-polarized light. f) Euhedral magnetite crystals in a diopside-rich portion of a leopard ore sample from Site 3. Diopside forms randomly-oriented subhedral prismatic crystals (medium grey) with interstitial antigorite (dark grey). Black mineral included in magnetite or interstitial between diopside crystals (right) is clinochlore. SEM-BSE image. g) Serpentinized pegmatoid ultramafic rock from Site 3 (see Fig. 3f), showing interlobate domains separated by coronae structures. Transmitted light, crossed polars. h) Enlargement of framed area in c). Light-coloured domain (upper left) is composed of coarse-grained interlocking antigorite; dark domain (right) is made up of isotropic lizardite, clinochlore (anomalous brown interference colour), antigorite (white-light grey) and magnetite (opaque). Fine-grained interlocking antigorite lines the boundary between the two domains. Transmitted light, crossed polars (upper) and plane polarized light (lower). Mineral abbreviations (after Whitney and Evans, 2010) – Mag: magnetite; Atg: antigorite; Clc: clinochlore; Brc: brucite; Cal: calcite; Di: diopside; Lz: lizardite; Ccp: chalcopyrite; Bn: bornite; Chr: chromite; Chl: chlorite.

Table 3

EPMA mineral compositions.

Location	Site 1					Site 1																		
Sample	LIC12					LIC14, LIC15																		
Rock type	Serpentinized peridotite					Nodular ore																		
Mineral	Antigorite		Spinel			Magnetite		Antigorite		Lizardite				Forsterite		Brucite				Clinochlore		Ti-rich chondrodite	
Additional information			core Mg-Al-rich chromite	middle Fe-rich chromite	rim Magnetite	Included in Mag				Included in Mag								Included in Mag		Included in Mag			
Ox. wt%	Mean (6)	s				Mean (9)	s	Mean (22)	s	Mean (5)	s	Mean (9)	s	Mean (4)	s	Mean (6)	s	Mean (5)	s	Mean (10)	s	Mean (19)	s		
SiO_2	42.80	2.03	0.00	0.34	0.01	0.13	0.20	44.69	0.58	44.55	0.53	37.99	2.06	38.84	0.88	41.55	1.65	3.62	2.14	0.46	1.29	33.97	1.27	34.89	34.73
TiO_2	0.01	0.02	0.03	0.14	0.01	0.01	0.02	0.01	0.01	0.02	0.01	0.02	0.03	0.02	0.00	0.09	0.13	0.00	0.00	0.01	0.01	0.01	0.01	5.24	5.42
Al_2O_3	1.00	0.51	25.73	0.62	0.00	0.04	0.04	0.57	0.26	0.79	0.41	4.65	0.25	5.16	0.91	0.00	0.00	0.30	0.24	0.01	0.02	14.70	3.02	0.00	0.11
Cr_2O_3	0.44	0.16	43.72	38.69	3.51	0.01	0.01	0.01	0.01	0.02	0.03	0.00	0.01	0.02	0.02	0.01	0.01	0.01	0.01	0.01	0.02	0.02	0.02	0.01	0.00
FeO	1.87	0.44	17.89	46.45	87.50	88.15	1.37	1.30	0.45	1.75	0.43	4.61	0.84	4.64	0.45	1.12	0.08	0.65	0.11	1.94	1.08	3.59	0.75	2.70	2.58
MnO	0.09	0.01	0.29	4.73	0.57	0.60	0.07	0.04	0.03	0.05	0.02	0.02	0.02	0.03	0.02	0.36	0.05	0.08	0.02	0.11	0.04	0.06	0.04	0.81	0.80
MgO	41.09	1.12	12.80	3.94	1.45	4.52	1.01	41.44	0.50	40.72	0.22	39.06	0.31	38.42	0.42	56.99	1.18	68.98	1.28	72.96	3.03	35.40	1.04	52.64	52.11
CaO	0.02	0.02	0.00	0.02	0.01	0.01	0.01	0.02	0.02	0.02	0.02	0.02	0.02	0.04	0.04	0.00	0.00	0.02	0.02	0.01	0.01	0.02	0.02	0.01	0.00
K_2O	0.00	0.01	0.00	0.00	0.00	0.01	0.01	0.01	0.01	0.00	0.00	0.01	0.01	0.01	0.01	0.00	0.01	0.00	0.01	0.00	0.01	0.01	0.01	0.00	0.01
Na_2O	0.00	0.01	0.00	0.07	0.00	0.00	0.00	0.00	0.00	0.00	0.00	0.00	0.00	0.01	0.01	0.00	0.01	0.01	0.01	0.00	0.00	0.01	0.01	0.00	0.00
Total	87.32		100.46	95.00	93.06	93.48		88.09		87.92		86.38		87.19		100.12		73.67		75.51		87.79		96.30	95.76
Mg#	97.5		58.1	25.5	8.4			98.2		98.1		97.0		95.0		98.9		99.5		98.5		96.0			

Location	Site 2												Site 3							Site 3					
Sample	ECL1												LAR4A							LAR2C					
Rock type	Fine-grained disseminated ore												Serpentinized peridotite							Mag-rich diopsidite				Mag-rich diopsidite	
Mineral	Magnetite	Antigorite					Diopside	Lizardite		Spinel			Magnetite		Antigorite		Lizardite	Clinochlore		Magnetite		Diopside		Diopside	
Additional information				Bastite core	 rim	Atg vein			Lz vein	core Mg-Al-rich chromite	middle Fe-rich chromite	rim Magnetite										Fine-grained		Di + Lz vein	
Ox. wt%		Mean (3)	s										Mean (4)	s	Mean (6)	s		Mean (5)	s	Mean (8)	s	Mean (5)	s		
SiO_2	0.07	44.72	0.30	45.56	43.70	44.59	55.98	41.68	41.22	0.03	2.42	0.12	0.03	0.02	43.78	0.32	39.38	35.63	0.47	0.16	0.21	55.42	0.36	55.39	55.35
TiO_2	0.08	0.01	0.01	0.01	0.02	0.05	0.00	0.04	0.05	0.10	0.43	0.09	0.06	0.01	0.01	0.01	0.03	0.02	0.01	0.06	0.03	0.01	0.01	0.00	0.03
Al_2O_3	0.02	0.94	0.32	3.89	1.79	1.35	0.00	4.39	5.07	23.76	2.11	0.04	0.00	0.00	1.42	0.23	6.64	11.67	1.18	0.00	0.01	0.05	0.05	0.07	0.17
Cr_2O_3	0.60	0.07	0.06	0.90	0.90	0.07	0.07	0.07	0.06	45.20	39.04	0.47	1.90	1.43	0.39	0.09	0.14	0.96	0.73	0.00	0.01	0.00	0.00	0.00	0.00
FeO	90.53	2.27	0.90	1.91	2.03	1.98	0.82	3.39	3.70	18.00	40.94	90.38	89.59	1.72	2.28	0.05	4.06	3.22	0.50	90.93	0.25	0.98	0.22	1.48	1.00
MnO	0.38	0.08	0.00	0.06	0.05	0.05	0.06	0.06	0.05	0.48	4.34	0.34	0.41	0.20	0.14	0.01	0.10	0.09	0.02	0.40	0.05	0.13	0.03	0.11	0.05
MgO	1.05	40.09	0.68	35.43	38.89	39.77	18.33	37.26	36.85	12.52	6.13	1.13	0.54	0.07	40.09	0.32	37.80	36.24	0.29	1.17	0.20	18.26	0.23	18.05	18.41
CaO	0.07	0.02	0.01	0.02	0.05	0.02	26.01	0.02	0.04	0.00	0.01	0.00	0.05	0.06	0.00	0.00	0.05	0.02	0.01	0.10	0.06	25.73	0.32	25.94	26.01
K_2O	0.02	0.01	0.02	0.00	0.00	0.00	0.00	0.06	0.06	0.00	0.01	0.00	0.00	0.01	0.00	0.00	0.00	0.00	0.00	0.00	0.00	0.00	0.00	0.01	0.00
Na_2O	0.02	0.01	0.01	0.01	0.00	0.03	0.00	0.02	0.05	0.00	0.00	0.00	0.00	0.01	0.00	0.00	0.00	0.00	0.01	0.02	0.03	0.01	0.00	0.00	0.02
Total	92.84	88.22		87.79	87.43	87.91	101.27	86.99	87.15	100.09	95.43	92.57	92.58		88.11		88.20	87.85		92.84		100.59		101.05	101.04
Mg#		96.9		97.1	97.2	97.3	97.6	95.1	94.7	57.7	34.2	6.5			96.9		94.3	95.6				96.9		95.6	97.0

Table 3 (continued)

Location	Site 3				Site 3																Site 3			
Sample	LAR2C (continued)				LAR2B																CGN8			
Rock type					Mag-rich pegmatoid serpentinite																Nodular ore			
Mineral	Lizardite		Antigorite		Magnetite				Antigorite						Lizardite		Clinochlore				Magnetite		Antigorite	
Additional information	Di + Lz vein				2nd generation		1st generation (<30 μm crystals)		Atg-only amoeboid domains		Corona around amoeboid domains		Lz + Clc + Mag amoeboid domains		Lz + Clc + Mag + Atg amoeboid domains		Lz + Clc + Mag amoeboid domains		Included in Mag					
Ox. wt%			Mean (6)	s	Mean (22)	s			Mean (4)	s	Mean (4)	s	Mean (9)	s	Mean (13)	s	Mean (4)	s	Mean (4)	s	Mean (6)	s	Mean (5)	s
SiO_2	40.62	40.77	44.11	0.69	0.09	0.16	0.08	0.27	44.17	0.26	43.77	0.62	44.08	0.36	38.17	1.16	35.38	1.28	34.18	0.97	0.22	0.20	43.94	1.08
TiO_2	0.03	0.01	0.01	0.01	0.04	0.02	0.03	0.06	0.00	0.01	0.00	0.00	0.00	0.01	0.04	0.01	0.01	0.02	0.02	0.00	0.00	0.00	0.01	0.01
Al_2O_3	5.63	5.67	1.26	0.65	0.00	0.01	0.00	0.00	1.24	0.44	1.01	0.19	1.20	0.20	6.93	0.49	13.45	2.44	15.21	2.22	0.10	0.05	1.57	0.88
Cr_2O_3	0.00	0.00	0.01	0.02	0.01	0.01	0.01	0.00	0.01	0.01	0.01	0.01	0.02	0.01	0.01	0.01	0.02	0.02	0.01	0.01	0.01	0.02	0.01	0.02
FeO	3.48	3.67	2.49	0.52	92.15	1.39	90.99	90.07	2.21	0.17	2.21	0.19	2.53	0.34	4.02	0.22	3.25	0.37	4.01	1.31	93.53	0.47	2.83	0.46
MnO	0.09	0.05	0.12	0.02	0.38	0.04	0.37	0.36	0.10	0.02	0.11	0.02	0.10	0.04	0.05	0.02	0.07	0.03	0.09	0.01	0.46	0.05	0.12	0.02
MgO	37.63	37.78	40.14	0.42	0.82	0.17	0.65	0.86	40.41	0.14	40.41	0.14	40.16	0.54	37.65	0.37	35.42	0.75	35.52	0.79	1.15	0.29	39.47	0.62
CaO	0.09	0.05	0.03	0.02	0.03	0.08	0.01	0.02	0.00	0.01	0.00	0.01	0.01	0.01	0.03	0.01	0.01	0.02	0.02	0.01	0.02	0.04	0.01	0.01
K_2O	0.01	0.01	0.00	0.00	0.01	0.01	0.01	0.00	0.00	0.00	0.00	0.00	0.01	0.01	0.01	0.01	0.00	0.01	0.01	0.01	0.01	0.01	0.01	0.01
Na_2O	0.00	0.00	0.00	0.00	0.01	0.01	0.02	0.00	0.00	0.01	0.01	0.01	0.01	0.01	0.01	0.01	0.00	0.00	0.00	0.00	0.01	0.01	0.01	0.01
Total	87.58	88.01	88.17		93.54		92.17	91.64	88.14		87.53		88.12		86.92		87.61		89.07		95.51		87.98	
Mg#	95.1	94.8	96.6						97.0		97.0		96.6		94.5		95.1		95.5				96.1	

Location	Site 3								Site 3											
Sample	CGN8 (continued)								CGN3											
Rock type									Di-rich nodular ore											
Mineral	Antigorite		Clinochlore		Lizardite		Andradite		Diopside	Magnetite		Diopside		Clinochlore					Antigorite	Andradite
Additional information	Included in Mag		Included in Mag		Included in Mag		Included in Mag		Included in Mag					Fine-grained, interstitial		Large tabular crystals		Included in Mag		Included in Mag
Ox. wt%	Mean (7)	s	Mean (10)	s	Mean (2)	s	Mean (3)	s		Mean (7)	s	Mean (10)	s			Mean (7)	s	Mean (6)	s	
SiO_2	44.12	0.49	34.29	1.07	39.59	0.33	35.21	0.31	56.07	0.07	0.06	55.47	0.20	35.68	35.64	32.07	1.32	33.60	1.32	42.45	34.77
TiO_2	0.00	0.01	0.01	0.01	0.02	0.03	0.14	0.13	0.01	0.03	0.02	0.00	0.01	0.01	0.02	0.01	0.01	0.01	0.01	0.00	0.26
Al_2O_3	0.99	0.35	13.42	2.26	6.40	0.10	0.28	0.17	0.00	0.02	0.04	0.03	0.04	11.91	11.54	18.06	1.92	14.92	2.80	3.35	0.34
Cr_2O_3	0.01	0.01	0.02	0.02	0.01	0.01	0.01	0.01	0.00	0.01	0.01	0.01	0.01	0.00	0.00	0.01	0.01	0.00	0.01	0.00	0.00
FeO	2.88	0.46	4.22	0.45	4.77	0.20	29.31	0.44	1.46	91.06	0.34	0.86	0.25	3.65	3.69	4.02	0.61	3.78	0.76	4.09	27.26
MnO	0.14	0.03	0.09	0.03	0.10	0.03	0.17	0.11	0.08	0.39	0.06	0.13	0.08	0.08	0.04	0.09	0.03	0.07	0.02	0.06	0.27
MgO	39.51	0.42	34.96	0.86	37.14	0.02	0.20	0.02	18.41	1.10	0.05	18.46	0.16	36.23	36.53	33.08	1.07	35.57	1.00	38.61	0.29
CaO	0.01	0.01	0.04	0.03	0.10	0.02	33.57	0.31	26.45	0.01	0.01	25.97	0.19	0.00	0.06	0.03	0.02	0.04	0.04	0.03	33.39
K_2O	0.00	0.01	0.01	0.01	0.00	0.00	0.00	0.00	0.01	0.00	0.01	0.00	0.01	0.00	0.00	0.01	0.01	0.01	0.01	0.01	0.00
Na_2O	0.00	0.01	0.00	0.01	0.00	0.00	0.03	0.02	0.04	0.00	0.01	0.01	0.01	0.00	0.01	0.00	0.01	0.00	0.01	0.02	0.00
Total	87.66		87.06		88.13		98.92		102.53	92.69		100.94		87.56	87.53	87.38		88.00		88.62	96.58
Mg#	96.1		94.2		93.3				95.70			97.5		94.6	94.6	93.6		95.7		94.40	

s: sample standard deviation.

Mineral abbreviations – Mag: magnetite; Atg: antigorite; Lz: lizardite; Clc: clinochlore; Di: diopside

4.3. Bulk rock geochemistry

Bulk rock compositions are reported in Table 4. The magnetite-poor (Fe_2O_3 <8.5 wt%) serpentinized peridotites have major and trace element concentrations typical for refractory peridotites (cf. Bodinier and Godard, 2003; Niu, 2004; Paulick et al., 2006; Andreani et al., 2014), such as low Al_2O_3 (~1-3 wt%) and TiO_2 (0.02-0.1 wt%), high Ni (~1400-2800 ppm) and Cr (~1900-2600 ppm) and low Co/Ni ratio (~0.05-0.07). The Cu and Zn contents (~20 and ~40-50 ppm, respectively) are also typical for upper mantle peridotites (cf. O'Neill and Palme, 1998; Niu, 2004; Fouquet et al., 2010). The pegmatoid serpentinites have variable Al_2O_3 (~0.8-2.6 wt%), Fe_2O_3 (~4.5-10 wt%), Ni (~500-2000 ppm), and Cr (~10-2700 ppm) contents and Co/Ni ratios (~0.05-0.2). However, Cu and Zn show very little variation (~20 and ~30-40 ppm, respectively).

The magnetite-enriched (Fe_2O_3 >28 wt%) serpentinites have different compositions reflecting their distinct host rocks. That after pegmatoid serpentinite has a high Al_2O_3 content (~2 wt%) and a high Co/Ni ratio (~0.4), but low Ni, Cr, Cu and Zn contents (~280, ~10, ~70, ~60 ppm, respectively). That after serpentinized peridotite (fine-grained disseminated ore) has Al_2O_3, Cr and Ni contents (~1 wt%, ~2200, ~1200 ppm, respectively) in the same range as the magnetite-poor serpentinized peridotites, but has higher Cu and Zn contents (~200 and ~120 ppm, respectively) and a higher Co/Ni ratio (~0.1). With further increase in magnetite content, i.e. in the nearly massive fine-grained disseminated ore, the contents of Cr (~1300 ppm) and Ni (~240 ppm) decrease, but the Co/Ni ratio increases (~0.6). The magnetite vein ore (Fe_2O_3 ~44 wt%) has low Ni (~500 ppm) and Cr (~70 ppm) contents and an intermediate Co/Ni ratio (~0.3). Moreover, it exhibits moderately high Zn (130 ppm) and the highest Cu content (~14000 ppm), which reflects the presence of chalcopyrite. The magnetite-rich diopsidite (Fe_2O_3 ~21 wt%) has a trace element composition similar to that of the pegmatoid serpentinite it is in contact with, but it has a higher Co/Ni ratio (~0.9).

In the nodular ores, the SiO_2 and MgO contents are inversely proportional to the amount of magnetite present. The Al_2O_3 and CaO concentrations are variable and reflect the different relative abundances of clinochlore and diopside (or carbonates), respectively. The TiO_2 content is generally low (0.02 wt%), but in the ore from Site 1 it can be slightly higher (~ 0.06 wt%), consistently with the presence of Ti-rich chondrodite. The nodular ores are virtually Cr-free (~10 ppm), have low Ni (~10-110 ppm) and relatively high Co (~320-440 ppm) contents, which translate into the highest observed Co/Ni ratios (~3-30). Moreover, compared to serpentinized peridotites and pegmatoid serpentinites, they show somewhat higher Cu and Zn (~30-50 ppm and ~80-100 ppm, respectively). The nodular ores, the magnetite-rich pegmatoid serpentinite and the magnetite-rich diopsidite share significant U and Th contents, which reach the maximum values at Site 1 (U = 2.9 ppm; Th = 0.9 ppm). In both magnetite-poor and magnetite-enriched serpentinized mantle peridotites, U and Th contents are below the detection limits of ICP-MS analysis (<0.01 and <0.02 ppm, respectively).

The relationships between magnetite enrichment, Co/Ni ratio and Cr content are shown in Fig. 6. Magnetite enrichment is generally accompanied by an increase in the Co/Ni ratio, but shows no correlation with the Cr content. In particular, the Cr content is very low (< 30 ppm) in the nodular ores, in the diopsidites and in most pegmatoid serpentinites (both magnetite-poor and magnetite-enriched) and is higher (Cr > 1200 ppm) in both barren and magnetite-enriched serpentinites after peridotites.

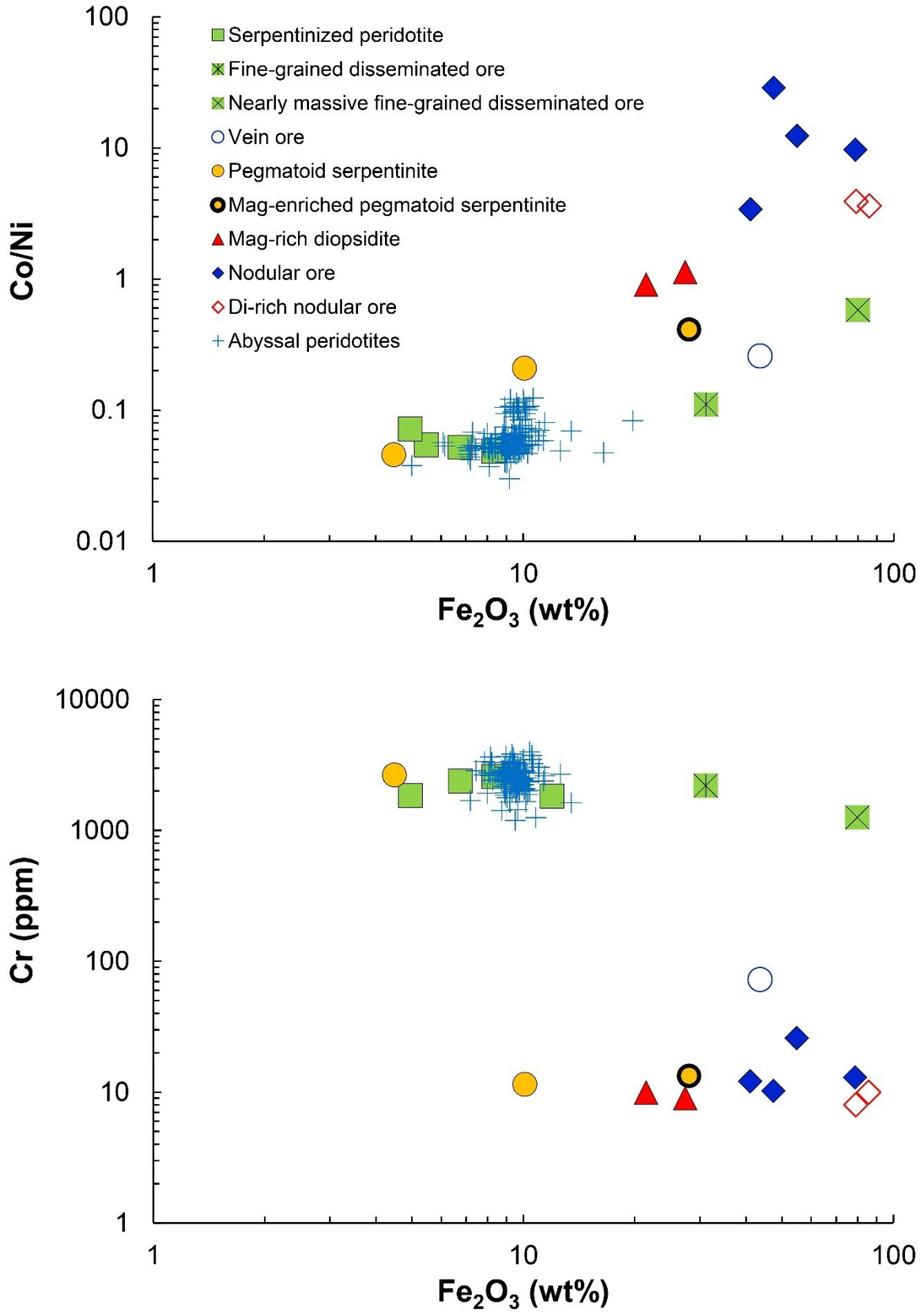

Fig. 6. Covariation of Co/Ni ratio and Cr content vs Fe_2O_3 content in Cogne rocks and ores (this work and Carbonin et al., 2014). Data for abyssal peridotites after Niu (2004), Paulick et al. (2006), Andreani et al. (2014) are shown for comparison.

Table 4

Bulk chemistry of representative rock types.

Location	Site 1	Site 1	Site 1	Site 1	Site 1	Site 1	Site 2	Site 2	Site 2	Site 3	Site 3	Site 3	Site 3	Site 3
Sample	LIC1B	CDP15	MZ18	LIC12	LIC14	LIC15	ECL1	MZL3	CRY1	LAR4	LAR2-1	LAR2-2	CGN3	CGN8
Rock type	Serpentinized peridotite	Pegmatoid serpentinite	Pegmatoid serpentinite	Serpentinized peridotite	Nodular ore	Nodular ore	Fine-grained disseminated ore	Nearly massive fine-grained disseminated ore	Vein ore	Serpentinized peridotite	Mag-rich pegmatoid serpentinite	Mag-rich diopsidite	Di-rich nodular ore	Nodular ore
Mineral assemblage	Atg, Mag, sulph.	Atg, Lz, Mag	Atg, Lz, Mag, sulph.	Atg, Lz, Mag, Tlc, Mg-Al-Chr, sulph.	Mag, Atg, Fo, Brc, Clc, Lz, Ti-Chn, sulph.	Mag, Atg, Cal, Clc, Brc, Lz	Mag, Atg, Di, Lz, Mg-Al-Chr, Chl, sulph.	Mag, Di, Atg, Lz, sulph.	Mag, Atg, Ccp, sulph.	Atg, Mag, Clc, Lz, Cal, sulph.	Atg, Mag, Lz, Clc, Di	Di, Mag, Atg	Mag, Di, Clc, Atg, Cal, Adr	Mag, Atg, Clc, Lz, Adr, Di
Ox. wt%														
SiO_2	41.95	40.22	40.92	39.54	22.39	20.51	32.20	9.08	24.65	39.10	33.15	42.40	6.52	10.06
TiO_2	0.02	0.03	0.03	0.02	0.06	0.02	0.04	0.01	0.04	0.10	0.03	0.02	0.02	0.02
Al_2O_3	1.04	0.77	2.59	1.01	0.62	1.08	0.92	1.15	0.43	2.67	2.31	0.27	0.86	0.31
Fe_2O_3	5.46	10.07	4.47	8.32	41.05	47.36	31.10	79.89	43.51	4.95	28.04	21.44	85.73	78.71
MgO	38.31	36.58	37.91	37.61	28.22	21.07	25.72	5.03	22.39	33.42	30.69	16.01	3.90	9.17
MnO	0.11	0.16	0.18	0.10	0.31	0.31	0.17	0.30	0.20	0.16	0.17	0.17	0.35	0.40
CaO	0.26	0.04	0.04	0.02	0.11	2.21	2.63	3.01	0.04	5.85	0.14	18.19	1.50	0.03
Na_2O	0.04	0.03	0.03	0.03	0.02	0.02	0.03	0.01	0.02	0.03	0.04	0.02	0.02	0.01
K_2O	0.01	0.01	0.01	0.01	0.01	0.01	0.01	0.01	0.00	0.01	0.01	0.01	0.01	0.01
P_2O_5	0.01	0.01	0.01	0.01	0.02	0.01	0.01	0.01	0.01	0.01	0.01	0.01	0.02	0.01
LOI	12.19	11.51	12.63	12.57	6.88	7.09	7.09	0.01	6.75	13.21	5.18	0.72	0.21	0.32
Total	99.40	99.42	98.83	99.25	99.68	99.68	99.91	98.51	98.02	99.50	99.77	99.27	99.13	99.04
ppm														
Be*	-	-	-	<1	<1	-	1	-	-	-	<1	<1	<1	<1
S*	-	-	-	1800	<200	-	3500	-	-	-	<200	<200	<200	<200
S	47	<10	23	1044	228	179	881	169	3068	821	118	103	14	<10
Sc*	-	-	-	6	<1	-	6	-	-	-	2	1	<1	<1
Sc	18	12	22	9	9	<5	<5	<5	10	<5	6	<5	9	13
V*	-	-	-	26	<8	-	31	-	-	-	20	12	<8	<8
V	27	5	57	26	13	12	37	32	51	41	20	14	11	11
Cr*	-	-	-	2395	<14	-	2196	-	-	-	<14	<14	21	<14
Cr	2100	12	2668	2580	12	10	2199	1256	73	1850	13	10	10	13
Co*	-	-	-	117.4	236.8	-	97.8	-	-	-	105.8	72.3	260.9	295.2
Co	76	111	88	133	330	321	129	139	124	96	145	95	407	436
Ni*	-	-	-	2403	93	-	1005	-	-	-	275	97	110	42
Ni	1401	531	1927	2727	97	11	1168	239	477	1338	352	105	113	45
Cu	19	15	18	17	34	27	194	217	13670	20	66	76	45	38
Zn	41	34	40	47	76	103	120	115	131	38	63	38	83	84
Ga*	-	-	-	0.8	1.3	-	<0.5	-	-	-	8.3	2.0	3.5	0.8
Ga	<5	7	8	<5	<5	8	<5	45	<5	7	15	<5	13	<5
Rb*	-	-	-	<0.1	<0.1	-	<0.1	-	-	-	0.1	<0.1	<0.1	<0.1
Rb	6	7	5	7	<3	7	15	<3	8	6	8	17	8	8
Sr*	-	-	-	<0.5	1.3	-	1.0	-	-	-	<0.5	12.4	1.8	0.6
Sr	7	5	5	4	6	81	6	5	7	100	6	18	8	<3
Y*	-	-	-	0.5	0.5	-	0.2	-	-	-	1.0	3.4	0.5	0.4
Y	<3	<3	<3	<3	<3	<3	<3	<3	<3	<3	<3	<3	13	10
Zr*	-	-	-	3.4	5.8	-	0.7	-	-	-	1.9	2.8	1.0	0.8
Zr	9	15	10	9	16	13	9	13	11	14	9	12	9	10
Nb*	-	-	-	<0.1	0.6	-	<0.1	-	-	-	<0.1	0.9	0.4	<0.1
Nb	<3	<3	<3	<3	<3	<3	<3	<3	<3	<3	<3	<3	<3	<3
Sn*	-	-	-	<1	<1	-	<1	-	-	-	<1	<1	<1	<1
Cs*	-	-	-	<0.1	<0.1	-	<0.1	-	-	-	<0.1	<0.1	<0.1	<0.1
Ba*	-	-	-	1.0	<1	-	<1	-	-	-	1.0	3.0	<1	<1
Ba	<10	<10	11	<10	<10	<10	<10	<10	<10	15	<10	<10	<10	<10
Hf*	-	-	-	<0.1	0.2	-	<0.1	-	-	-	<0.1	0.1	<0.1	<0.1
Ta*	-	-	-	<0.1	<0.1	-	<0.1	-	-	-	<0.1	<0.1	<0.1	<0.1
W*	-	-	-	1.1	4.0	-	<0.5	-	-	-	<0.5	<0.5	<0.5	<0.5
Pb	8	11	9	33	15	9	9	<5	18	14	27	22	10	<5
Th*	-	-	-	<0.2	0.9	-	<0.2	-	-	-	0.3	0.5	<0.2	<0.2
Th	9	9	9	<3	12	11	6	10	10	4	<3	8	14	12
U*	-	-	-	<0.1	2.9	-	<0.1	-	-	-	1.3	2.0	0.8	2.4
U	6	9	4	<3	4	<3	4	<3	6	<3	<3	<3	<3	<3
La*	-	-	-	0.9	0.4	-	0.2	-	-	-	0.8	3.3	0.9	0.3
La	<10	<10	<10	<10	<10	<10	<10	<10	<10	<10	<10	<10	<10	<10
Ce*	-	-	-	0.7	0.6	-	0.1	-	-	-	0.9	5.8	1.1	0.7
Ce	<10	<10	<10	<10	<10	<10	16	<10	<10	10	11	<10	<10	<10
Nd*	-	-	-	0.4	0.7	-	<0.3	-	-	-	0.3	3.8	0.7	0.4
Nd	12	28	20	23	19	17	22	27	24	17	18	29	22	27

* element concentrations measured by ICP-MS.

- = not determined.

Mineral abbreviations not used before – Adr: andradite; Chn: chondrodite; Fo: forsterite; Tlc: talc; sulph: sulphides.

4.4. Age of the deposit

The high U (+ Th) contents in nodular ores from Site 1 and Site 3 can be attributed to the presence of uraninite inclusions in magnetite. Uraninite forms anhedral to euhedral cuboctahedral crystals, ranging in size from ~1 to 40 μm (Fig. 7a-c, e, g). Textural evidence suggests that uraninite and magnetite (+clinochlore) were contemporaneous (Fig. 7b, g). The compositions of the uraninite crystals are reported in Table 5. The U/Th ratios are variable (3 to 21), especially at Site 1, where both the highest and the lowest Th contents were measured. The FeO and CaO concentrations are relatively high (FeO = 0.8-4.9 wt%; CaO = 0.06-1.2 wt%), but they are unrelated to PbO contents, which excludes late-stage alteration (Alexandre and Kyser, 2005). Excitation of the host magnetite within the microprobe interaction volume could explain the presence of Fe in the analyses. On the contrary, the Ca content is considered to be primary and ascribed to lattice-bound substitutions of Ca for U. A less than 1 μm-thick, U-rich rim is sometimes observed in uraninite crystals (Fig. 7e), and is ascribed to partial alteration.

The U-Th-Pb ages calculated for a group of three small (<10 μm) uraninite grains from Site 1 (Fig. 7a-c) are plotted in Fig. 7d. Due to the small grain size, only single-spot analyses were acquired. The weighted average age is 161.8 ± 3.5 Ma (MSWD = 0.51). Fig. 7f shows the ages obtained for an aggregate of zoned grains from Site 1 (Fig. 7e). The crystals have a U-rich rim, which testifies for partial alteration. Therefore, I only considered sixteen analyses that form a plateau for PbO, UO_2 and ThO_2 concentrations (Fig. 8). The weighted average age for the plateau, after rejecting two outliers, is 150.8 ± 2.0 Ma (MSWD = 1.03). The weighted average age calculated for a big (~ 40 μm), unzoned uraninite crystal from Site 3 (Fig. 7g), which is intergrown with magnetite and contains chlorite, is 151.9 ± 1.4 Ma (MSWD = 0.91) (Fig. 7h). Also in this case only plateau PbO values were considered (Fig. 8). The two age determinations that yield the lowest uncertainties and best MSWD values (i.e., close to unity) are within errors of each other and are considered to be the most reliable. However,

considering the limited age scatter, it is reasonable to combine all the data into a single age determination, which yields a value of 152.8 ± 1.3 Ma (MSWD = 1.3; Fig 7i).

Fig. 7. Uraninite microstructural features and U-Th-Pb dating. a-d) Uraninite in Site 1 leopard ore and related dating [b) and c) from the same ore sample]. e-f) Aggregate of uraninite crystals in Site 1 leopard ore and related dating. Chemical map shows a U-rich rim. g-h) Inclusion-rich (magnetite, dark grey; clinochlore, black) uraninite crystal in Site 3 leopard ore and related dating. The chemical map reveals a homogeneous composition. i) Combination of all single-spot ages. Images and maps were obtained by SEM-BSE and EPMA, respectively. Geochronological data plotted using ISOPLOT (v. 3.75) Visual Basic add-in for Excel® (Ludwig, 2012).

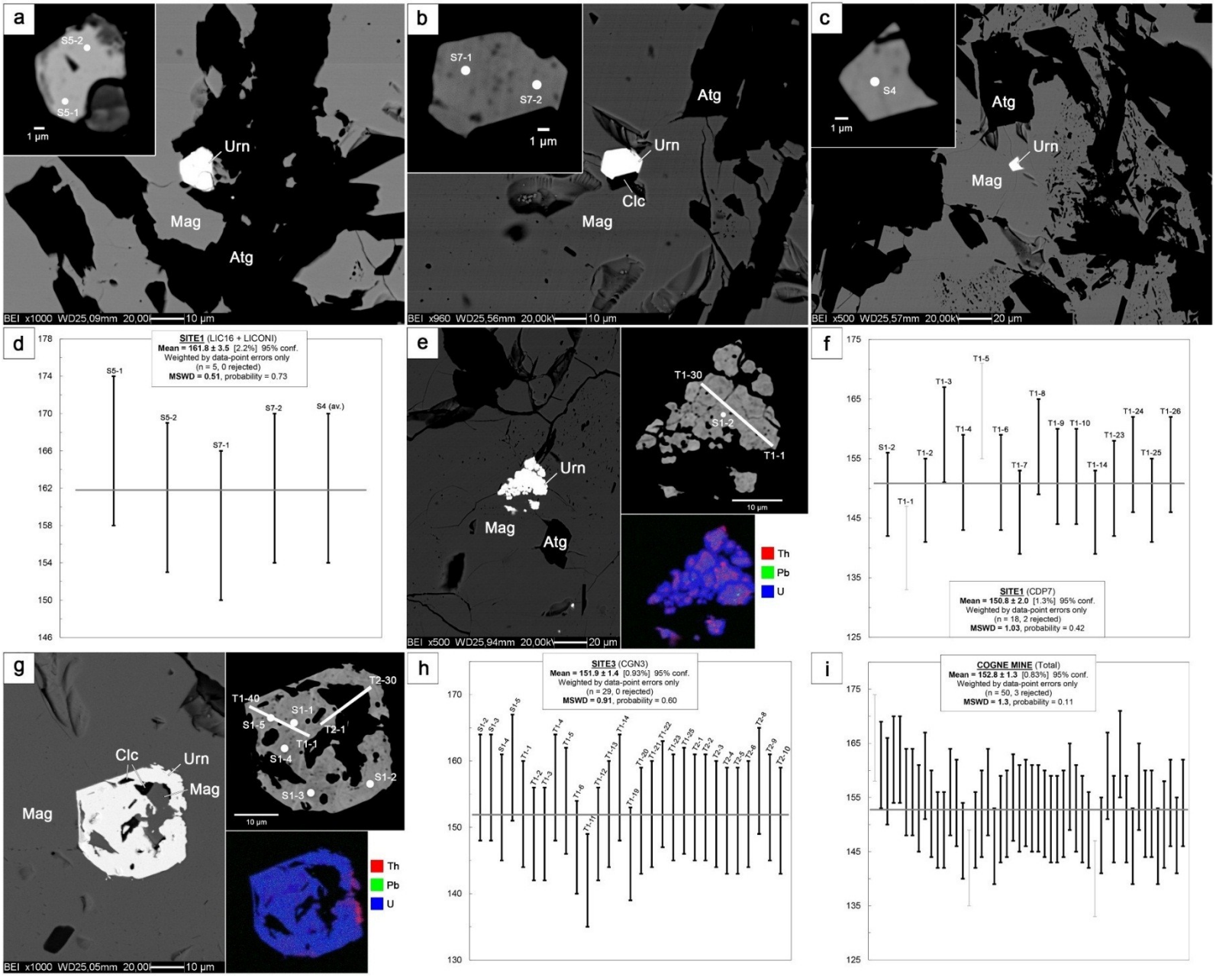
a
S5-2
S5-1
1 µm
Urn
Mag
Atg
BEI x1000 WD25,09mm 20,00kV 10 µm
b
S7-1
S7-2
1 µm
Atg
Urn
Clc
Mag
BEI x960 WD25,56mm 20,00kV 10 µm
c
S4
1 µm
Atg
Urn
Mag
BEI x500 WD25,57mm 20,00kV 20 µm
d
SITE1 (LIC16 + LICONI)
Mean = 161.8 ± 3.5 [2.2%] 95% conf.
Weighted by data-point errors only
(n = 5, 0 rejected)
MSWD = 0.51, probability = 0.73
S5-1
S5-2
S7-1
S7-2
S4 (av.)
178
174
170
166
162
158
154
150
146
e
Urn
Mag
Atg
BEI x500 WD25,94mm 20,00kV 20 µm
T1-30
S1-2
T1-1
10 µm
Th
Pb
U
f
SITE1 (CDP7)
Mean = 150.8 ± 2.0 [1.3%] 95% conf.
Weighted by data-point errors only
(n = 18, 2 rejected)
MSWD = 1.03, probability = 0.42
175
165
155
145
135
125
g
Clc
Urn
Mag
Mag
BEI x1000 WD25,05mm 20,00kV 10 µm
T2-30
T1-40
S1-1
S1-5
T2-1
T1-1
S1-4
S1-2
S1-3
10 µm
Th
Pb
U
h
SITE3 (CGN3)
Mean = 151.9 ± 1.4 [0.93%] 95% conf.
Weighted by data-point errors only
(n = 29, 0 rejected)
MSWD = 0.91, probability = 0.60
170
160
150
140
130
i
COGNE MINE (Total)
Mean = 152.8 ± 1.3 [0.83%] 95% conf.
Weighted by data-point errors only
(n = 50, 3 rejected)
MSWD = 1.3, probability = 0.11
175
165
155
145
135
125

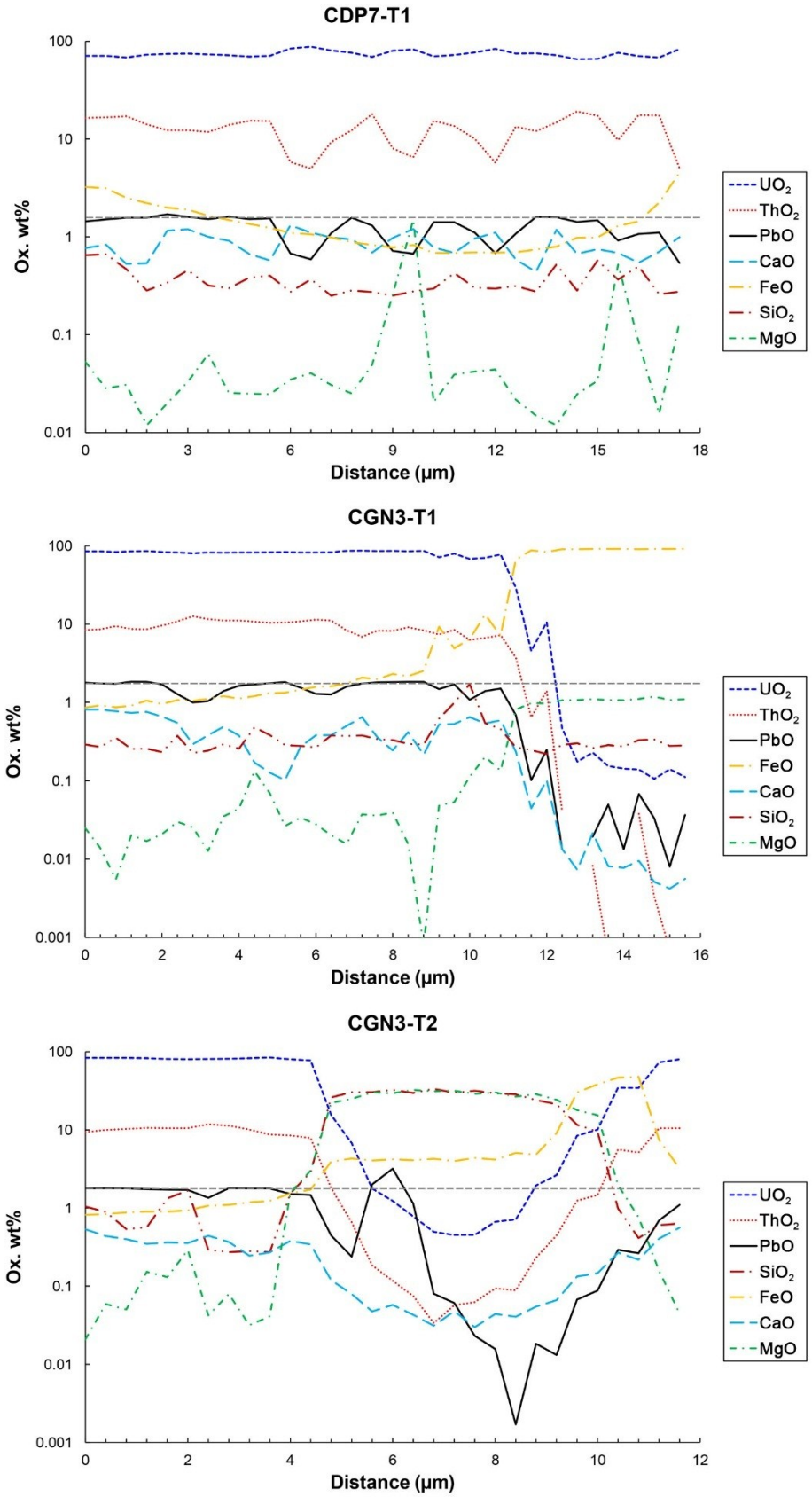

Fig. 8. Electron microprobe traverses across uraninite crystals (see Fig. 7 for their position). Horizontal dashed lines indicate PbO plateaux.

Table 5

Uraninite compositions and calculated single-spot ages. Rejected analyses, i.e out of the plateau beacuse of Pb loss or mixed/contaminated (cont.), are in italics.

Location	Sample	S = single spot, T = traverse	Site and analysis number	Ox. wt%[1]								ppm			U/Th	Age (Ma)	Error[2] ± (Ma)	Notes
				UO_2	ThO_2	PbO	MgO	SiO_2	FeO	CaO	Total	U	Th	Pb				
Site 1	LIC16	S	5-1	86.81	7.06	1.99	0.04	0.40	1.92	0.06	98.28	765231	62044	18474	12	166	8	
		S	5-2	86.79	6.84	1.93	0.04	0.20	1.72	0.15	97.67	765054	60111	17917	13	161	8	
Site 1	LICONI	S	7-1	91.68	4.34	1.98	0.04	0.34	2.36	0.11	100.84	808160	38140	18381	21	158	8	
		S	7-2	87.14	7.92	1.95	0.02	0.34	2.50	0.05	99.92	768140	69602	18102	11	162	8	
		S	4[3]	88.37	7.01	1.98	0.03	0.32	2.13	0.09	99.92	778982	61570	18344	13	162	8	
Site 1	CDP7	S	1-2	74.22	13.00	1.57	0.01	0.27	1.08	1.07	91.21	654250	114246	14575	6	149	7	
		T	1-1	71.24	16.43	1.44	0.05	0.65	3.24	0.77	93.83	627981	144389	13368	4	140	7	
		T	1-2	70.91	16.68	1.51	0.03	0.66	3.14	0.83	93.76	625072	146586	14018	4	148	7	
		T	1-3	68.18	17.13	1.57	0.03	0.47	2.52	0.53	90.43	601007	150540	14575	4	159	8	
		T	1-4	72.72	14.15	1.57	0.01	0.28	2.22	0.54	91.49	641027	124352	14575	5	151	8	
		T	1-5	74.19	12.28	1.71	0.02	0.34	2.00	1.16	91.70	653985	107918	15874	6	163	8	
		T	1-6	74.97	12.34	1.60	0.03	0.46	1.91	1.20	92.51	660861	108445	14853	6	151	8	
		T	1-7	73.58	11.84	1.52	0.06	0.32	1.65	1.00	89.98	648608	104051	14110	6	146	7	
		T	1-8	71.99	13.94	1.61	0.03	0.30	1.49	0.91	90.27	634592	122506	14946	5	157	8	
		T	1-9	69.77	15.37	1.52	0.03	0.38	1.36	0.67	89.10	615023	135073	14110	5	152	8	
		T	1-10	71.17	15.32	1.55	0.02	0.40	1.24	0.58	90.28	627364	134634	14389	5	152	8	
		T	*1-11*	*84.63*	*5.84*	*0.68*	*0.03*	*0.27*	*1.10*	*1.31*	*93.87*							
		T	*1-12*	*88.19*	*5.00*	*0.59*	*0.04*	*0.37*	*1.06*	*1.11*	*96.36*							Pb loss
		T	*1-13*	*80.50*	*9.34*	*1.09*	*0.03*	*0.25*	*0.99*	*0.99*	*93.19*							
		T	1-14	76.19	12.33	1.57	0.03	0.28	0.88	0.94	92.23	671615	108358	14575	6	146	7	
		T	*1-15*	*69.01*	*18.10*	*1.31*	*0.05*	*0.27*	*0.83*	*0.69*	*90.27*							
		T	*1-16*	*79.82*	*8.04*	*0.72*	*0.26*	*0.25*	*0.78*	*0.98*	*90.85*							
		T	*1-17*	*82.57*	*6.53*	*0.68*	*1.49*	*0.28*	*0.83*	*1.20*	*93.58*							
		T	*1-18*	*70.16*	*15.44*	*1.41*	*0.02*	*0.30*	*0.69*	*0.78*	*88.80*							
		T	*1-19*	*72.26*	*13.55*	*1.41*	*0.04*	*0.43*	*0.68*	*0.69*	*89.06*							Pb loss
		T	*1-20*	*77.04*	*10.07*	*1.11*	*0.04*	*0.30*	*0.70*	*0.96*	*90.23*							
		T	*1-21*	*83.87*	*5.76*	*0.69*	*0.04*	*0.30*	*0.69*	*1.11*	*92.45*							
		T	*1-22*	*74.85*	*13.37*	*1.08*	*0.02*	*0.32*	*0.70*	*0.59*	*90.92*							
		T	1-23	75.35	12.05	1.60	0.01	0.28	0.74	0.44	90.47	664211	105897	14853	6	150	8	
		T	1-24	72.12	14.77	1.59	0.01	0.52	0.80	1.18	90.99	635738	129801	14760	5	154	8	
		T	1-25	65.48	19.20	1.42	0.02	0.28	0.98	0.68	88.07	577207	168732	13182	3	148	7	
		T	1-26	65.97	17.38	1.48	0.03	0.58	0.99	0.75	87.18	581526	152737	13739	4	154	8	
		T	*1-27*	*76.54*	*9.75*	*0.92*	*0.52*	*0.37*	*1.30*	*0.69*	*90.08*							
		T	*1-28*	*70.36*	*17.59*	*1.07*	*0.09*	*0.50*	*1.44*	*0.54*	*91.59*							
		T	*1-29*	*68.29*	*17.48*	*1.11*	*0.02*	*0.26*	*2.25*	*0.71*	*90.11*							Pb-loss
		T	*1-30*	*83.32*	*5.04*	*0.54*	*0.13*	*0.28*	*4.53*	*0.99*	*94.84*							
Site3	CGN3	S	1-2	84.95	9.61	1.84	0.03	0.26	1.41	0.14	98.24	748835	84454	17081	9	156	8	
		S	1-3	84.91	8.92	1.84	0.02	0.23	1.71	0.60	98.24	748482	78390	17081	10	156	8	
		S	1-4	85.75	8.28	1.82	0.03	0.27	1.25	0.65	98.05	755887	72766	16895	10	153	8	
		S	1-5	83.56	10.35	1.86	0.02	0.22	1.22	0.31	97.55	736582	90957	17267	8	159	8	
		T	1-1	85.17	8.37	1.79	0.03	0.29	0.86	0.81	97.31	750774	73557	16617	10	152	8	
		T	1-2	84.53	8.61	1.75	0.01	0.27	0.92	0.81	96.90	745133	75666	16246	10	149	7	
		T	1-3	83.51	9.46	1.73	0.01	0.35	0.87	0.77	96.70	736141	83136	16060	9	149	7	
		T	1-4	84.90	8.68	1.84	0.02	0.26	0.91	0.73	97.34	748394	76281	17081	10	156	8	
		T	1-5	85.45	8.57	1.83	0.02	0.26	1.06	0.76	97.94	753242	75314	16988	10	154	8	
		T	1-6	83.44	9.60	1.71	0.02	0.23	0.95	0.66	96.61	735524	84366	15874	9	147	7	
		T	*1-7*	*81.99*	*10.85*	*1.28*	*0.03*	*0.37*	*1.07*	*0.55*	*96.14*							
		T	*1-8*	*80.25*	*12.60*	*0.99*	*0.03*	*0.23*	*1.05*	*0.29*	*95.44*							
		T	*1-9*	*82.19*	*11.57*	*1.04*	*0.01*	*0.24*	*1.11*	*0.38*	*96.54*							Pb loss
		T	*1-10*	*81.58*	*11.11*	*1.40*	*0.04*	*0.29*	*1.20*	*0.49*	*96.11*							
		T	1-11	82.11	11.08	1.63	0.04	0.26	1.12	0.38	96.62	723800	97372	15132	7	142	7	
		T	1-12	81.94	10.71	1.71	0.13	0.48	1.21	0.17	96.35	722302	94121	15874	8	149	7	
		T	1-13	82.81	10.44	1.76	0.07	0.39	1.32	0.13	96.91	729971	91748	16338	8	152	8	
		T	1-14	83.48	10.49	1.82	0.03	0.29	1.33	0.10	97.53	735877	92187	16895	8	156	8	
		T	*1-15*	*82.37*	*10.84*	*1.54*	*0.03*	*0.28*	*1.45*	*0.27*	*96.78*							Pb loss

Table 5 (continued)

Location	Sample	S = single spot, T = traverse	Site and analysis number	Ox. wt% UO_2	ThO_2	PbO	MgO	SiO_2	FeO	CaO	Total	ppm U	Th	Pb	U/Th	Age (Ma)	Error ± (Ma)	Notes
Site3	CGN3	T	*1-16*	*82.18*	*11.36*	*1.29*	*0.03*	*0.27*	*1.58*	*0.38*	*97.09*							
		T	*1-17*	*82.82*	*11.07*	*1.26*	*0.02*	*0.38*	*1.61*	*0.38*	*97.54*							Pb loss
		T	*1-18*	*86.21*	*8.31*	*1.60*	*0.02*	*0.37*	*1.75*	*0.50*	*98.76*							
		T	1-19	86.98	6.88	1.75	0.04	0.38	2.08	0.65	98.76	766729	60462	16246	13	146	7	
		T	1-20	85.81	8.27	1.80	0.04	0.34	1.97	0.36	98.58	756416	72678	16710	10	151	8	
		T	1-21	86.35	8.19	1.82	0.04	0.33	2.31	0.25	99.28	761176	71975	16895	11	152	8	
		T	1-22	84.73	9.10	1.83	0.02	0.30	2.17	0.42	98.56	746896	79972	16988	9	155	8	
		T	1-23	86.42	8.31	1.83	0.00	0.29	2.53	0.22	99.60	761793	73029	16988	10	153	8	
		T	*1-24*	*71.05*	*7.37*	*1.48*	*0.05*	*0.62*	*9.28*	*0.52*	*90.37*							Mag cont.
		T	1-25	79.68	8.45	1.70	0.05	0.99	4.91	0.53	96.31	702380	74260	15781	9	154	8	
		T	*1-26*	*68.06*	*6.29*	*1.08*	*0.11*	*1.71*	*6.43*	*0.65*	*84.34*							
		T	*1-27*	*70.34*	*6.67*	*1.40*	*0.20*	*0.55*	*13.20*	*0.54*	*92.90*							Mag cont.
		T	*1-28*	*77.26*	*7.21*	*1.50*	*0.13*	*0.46*	*7.12*	*0.59*	*94.27*							
		T	*1-29*	*29.24*	*3.76*	*0.69*	*0.81*	*0.27*	*66.02*	*0.24*	*101.02*							
		T	*1-30*	*4.54*	*0.65*	*0.10*	*0.98*	*0.25*	*87.94*	*0.04*	*94.50*							
		T	*1-31*	*10.58*	*1.41*	*0.25*	*0.97*	*0.22*	*83.28*	*0.10*	*96.81*							
		T	*1-32*	*0.47*	*0.04*	*0.01*	*1.06*	*0.29*	*90.47*	*0.01*	*92.36*							
		T	*1-33*	*0.18*	*0.00*	*0.00*	*1.08*	*0.30*	*90.93*	*0.01*	*92.49*							
		T	*1-34*	*0.23*	*0.01*	*0.02*	*1.10*	*0.26*	*91.09*	*0.02*	*92.73*							
		T	*1-35*	*0.15*	*0.00*	*0.05*	*1.07*	*0.29*	*91.43*	*0.01*	*93.00*							Mag
		T	*1-36*	*0.14*	*0.00*	*0.01*	*1.06*	*0.28*	*91.25*	*0.01*	*92.75*							
		T	*1-37*	*0.14*	*0.04*	*0.07*	*1.11*	*0.33*	*90.99*	*0.01*	*92.68*							
		T	*1-38*	*0.11*	*0.00*	*0.03*	*1.19*	*0.34*	*91.11*	*0.01*	*92.78*							
		T	*1-39*	*0.14*	*0.00*	*0.01*	*1.07*	*0.28*	*91.49*	*0.00*	*93.00*							
		T	*1-40*	*0.11*	*0.00*	*0.04*	*1.10*	*0.28*	*91.56*	*0.01*	*93.10*							
		T	2-1	83.84	9.41	1.78	0.02	1.05	0.82	0.53	97.45	739050	82696	16524	9	153	8	
		T	2-2	83.66	10.01	1.79	0.06	0.89	0.83	0.44	97.68	737463	87969	16617	8	153	8	
		T	2-3	83.57	10.31	1.77	0.05	0.54	0.87	0.40	97.51	736670	90606	16431	8	152	8	
		T	2-4	82.66	10.59	1.75	0.15	0.57	0.90	0.35	96.97	728648	93066	16246	8	151	8	
		T	2-5	81.14	10.56	1.71	0.13	1.32	0.90	0.36	96.12	715250	92803	15874	8	151	8	
		T	2-6	80.17	10.56	1.70	0.29	1.68	0.94	0.36	95.69	706699	92803	15781	8	152	8	
		T	*2-7*	*81.04*	*11.83*	*1.35*	*0.04*	*0.29*	*1.07*	*0.44*	*96.07*							Pb loss
		T	2-8	81.46	11.34	1.79	0.08	0.27	1.10	0.37	96.41	718070	99657	16617	7	157	8	
		T	2-9	83.04	10.10	1.77	0.03	0.28	1.19	0.25	96.65	731998	88760	16431	8	153	8	
		T	2-10	84.43	8.72	1.77	0.04	0.27	1.23	0.27	96.74	744251	76632	16431	10	151	8	
		T	*2-11*	*80.24*	*8.46*	*1.52*	*1.56*	*1.55*	*1.54*	*0.38*	*95.25*							
		T	*2-12*	*77.39*	*7.90*	*1.47*	*3.01*	*2.88*	*1.71*	*0.34*	*94.70*							Pb loss
		T	*2-13*	*15.58*	*1.81*	*0.44*	*22.15*	*25.96*	*3.93*	*0.12*	*69.99*							
		T	*2-14*	*6.79*	*0.66*	*0.24*	*24.85*	*30.41*	*4.32*	*0.08*	*67.35*							
		T	*2-15*	*1.77*	*0.19*	*2.01*	*30.08*	*30.31*	*4.07*	*0.05*	*68.47*							
		T	*2-16*	*1.23*	*0.12*	*3.19*	*29.35*	*32.56*	*4.19*	*0.06*	*70.69*							
		T	*2-17*	*0.78*	*0.08*	*1.14*	*32.48*	*29.60*	*4.09*	*0.04*	*68.21*							
		T	*2-18*	*0.49*	*0.03*	*0.08*	*31.29*	*33.54*	*4.27*	*0.03*	*69.74*							Clc cont.
		T	*2-19*	*0.45*	*0.06*	*0.06*	*31.76*	*29.96*	*4.01*	*0.05*	*66.35*							
		T	*2-20*	*0.45*	*0.06*	*0.02*	*28.89*	*31.78*	*4.38*	*0.03*	*65.62*							
		T	*2-21*	*0.67*	*0.09*	*0.02*	*30.20*	*29.41*	*4.18*	*0.04*	*64.61*							
		T	*2-22*	*0.71*	*0.09*	*0.00*	*26.53*	*28.45*	*5.08*	*0.04*	*60.90*							
		T	*2-23*	*1.94*	*0.23*	*0.02*	*28.73*	*24.13*	*4.84*	*0.05*	*59.94*							
		T	*2-24*	*2.64*	*0.44*	*0.01*	*24.24*	*21.32*	*9.06*	*0.07*	*57.78*							
		T	*2-25*	*8.42*	*1.24*	*0.07*	*17.84*	*11.61*	*30.10*	*0.13*	*69.41*							
		T	*2-26*	*10.07*	*1.47*	*0.09*	*15.36*	*9.57*	*38.33*	*0.15*	*75.03*							Mag + Clc cont.
		T	*2-27*	*34.76*	*5.62*	*0.29*	*1.96*	*0.99*	*46.75*	*0.27*	*90.63*							
		T	*2-28*	*34.48*	*5.12*	*0.26*	*0.76*	*0.41*	*47.89*	*0.22*	*89.15*							
		T	*2-29*	*73.21*	*10.51*	*0.69*	*0.16*	*0.60*	*7.42*	*0.40*	*93.00*							Mag cont.
		T	*2-30*	*80.12*	*10.55*	*1.10*	*0.04*	*0.63*	*3.21*	*0.56*	*96.22*							Pb loss

[1] Ti and Cr are systematically below the detection limit, therefore they are not reported.

[2] 5% relative error (equivalent to the accuracy on Pb analysis; Bowles, 1990).

[3] Average of 5 repetitions on the same point.

4.5. Geochemistry of Cogne magnetite

The compositions of the Cogne magnetites are reported in Tables 3 and 6. The magnetites show significant substitutions of Fe by Mg and Mn (Fig. 9). The concentrations of these metals are the highest at Site 1 (median = ~24100 ppm and ~5000 ppm, respectively). Concentrations of Ca, Si, Mo, Zr and Cr are generally below or close to the ICP-MS detection limits; only magnetite forming the disseminated ore from Site 2 has significant Cr contents, which can be as high as ~150 ppm. Among the other trace elements, the concentrations of Ni, Co, Ti, and Zn are generally an order of magnitude higher than those of V (Fig. 9). The highest concentrations of Co are found at Site 1 (median = ~570 ppm), whereas the lowest concentrations are in magnetite in disseminated ore from Site 2 (median = ~80 ppm). In spite of across-site variations, the Co content is fairly constant in magnetite from the same sample. The Ti content is the highest in magnetite from disseminated ore from Site 2 (median = ~570 ppm) and the lowest in magnetite from diopside-rich rocks from Site 1 and Site 3 (median = ~60 ppm). The Ni and V contents are highest in magnetite from the magnetite-rich pegmatoid serpentinite (median = ~670 ppm and ~60 ppm, respectively). The lowest Ni and V contents are observed in Site 1 ore (median = ~80 ppm) and in vein magnetite (median = ~6 ppm), although in the latter both elements are highly variable. The Zn contents show minor variability: the highest values are found in the vein magnetite (median: ~160 ppm) and the minimum values are found in magnetite from Site 3 (median: ~80 ppm).

Robust PCA indicates that the two first principal components (PC1 and PC2) can explain 97% of the variability of the magnetite compositional data and thus can adequately be used to describe the various magnetite populations. As shown by the loading plot (Fig. 10), Mg, Mn, Co and Zn are highly correlated, while Ni is anti-correlated and V and Ti vary independently from the other elements. In the PC1 vs. PC2 plot, one cluster of samples, which encompasses the magnetites in the nodular ores from Site 1 and Site 3 and the magnetite-rich diopsidite, is characterized by the highest (Mg, Mn, Co,

Zn)/Ni ratios. High Ni contents are instead distinctive of magnetite in disseminated ore from Site 2 and in magnetite-rich pegmatoid serpentinite from Site 3 (Fig. 9, 10). These high-Ni magnetites form two distinct groups, in which high Ni is associated with high Ti (and Cr) and high V, respectively. Vein magnetites, having a very variable Ni and low overall V, plot in an intermediate position between high-Ni and low-Ni magnetites. When plotted on the Zn vs. Co plane (Fig. 11), most of the magnetites show a nearly constant Zn/Co ratio of ~0.28. Magnetites in the veins and in fine-grained disseminated ore from Site 2 have higher Zn/Co ratios (~1).

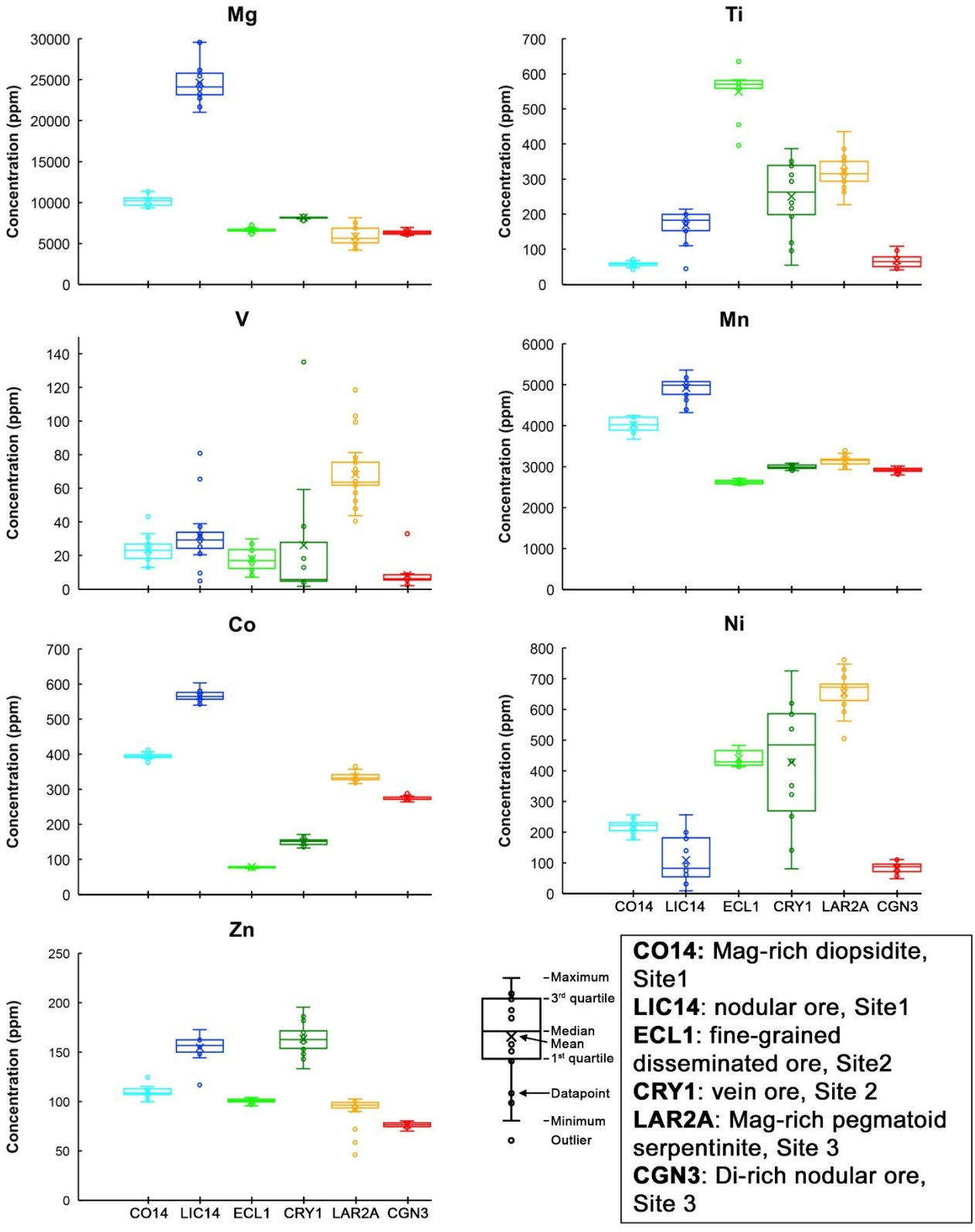

Fig. 9. Box and whiskers plot of magnetite trace element composition.

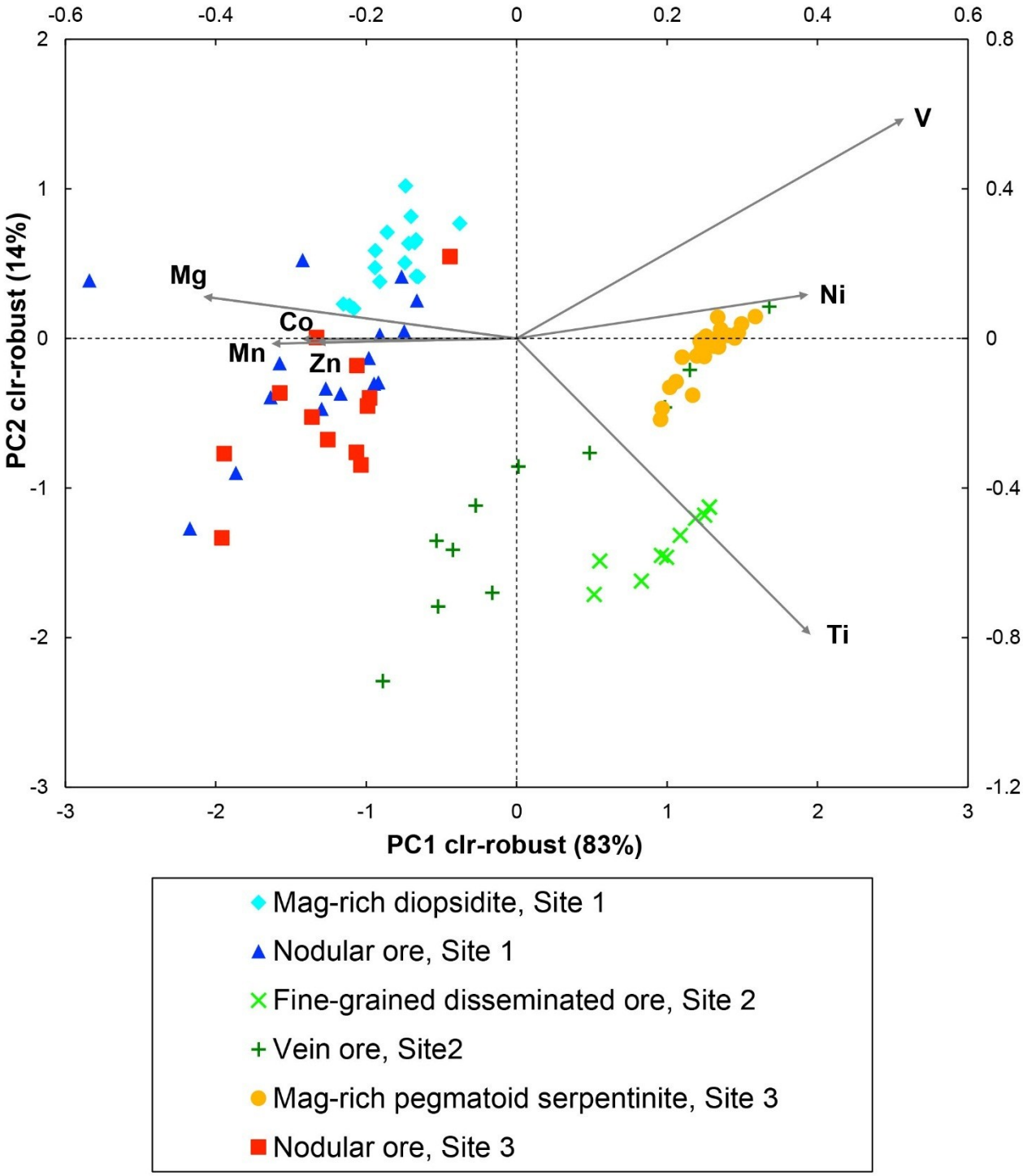

Fig. 10. Robust-PCA of magnetite trace element composition. Coordinates of datapoints (scores) are on left and lower horizontal axes. Coordinates of variables (loadings) are on right and upper horizontal axes.

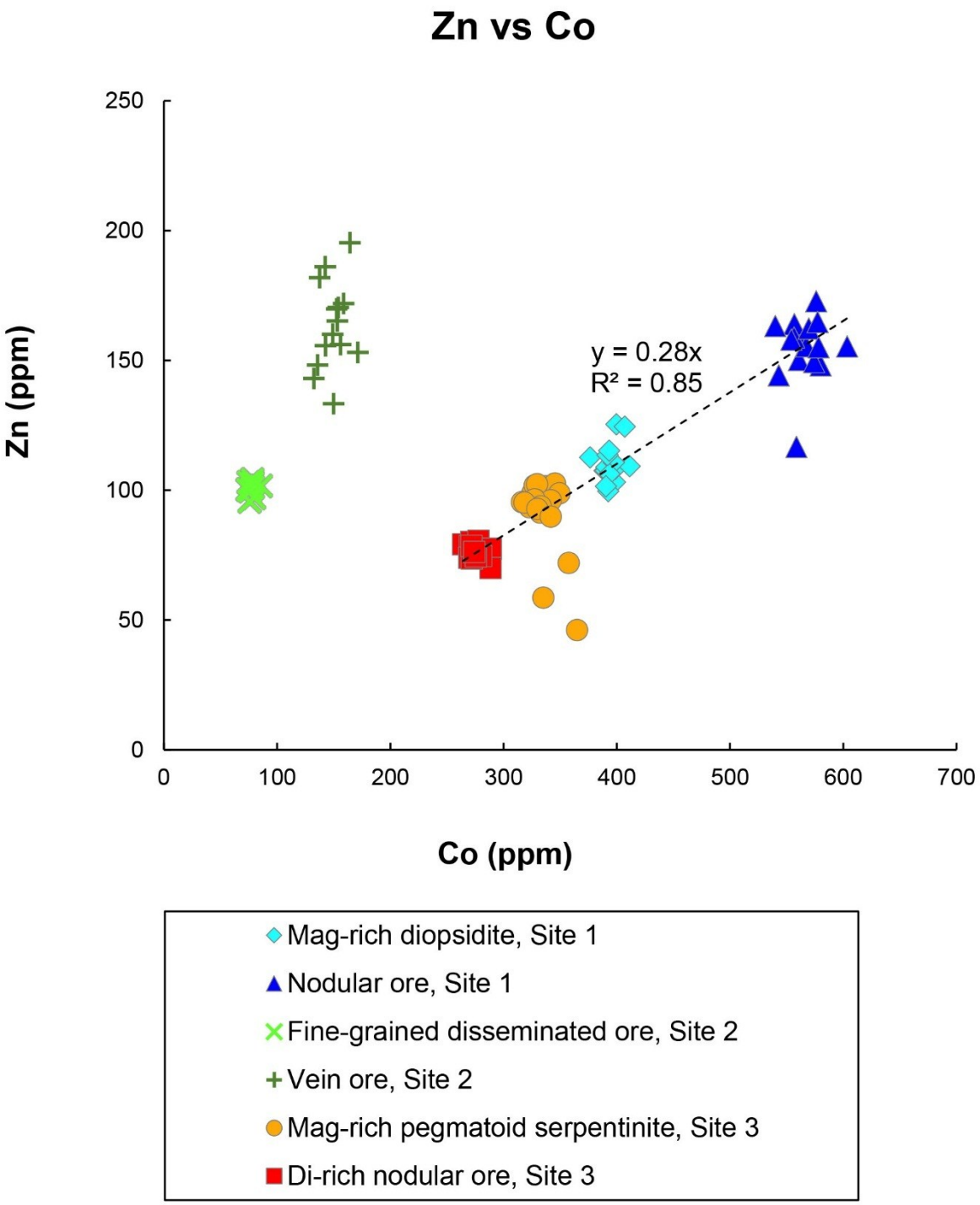

Fig. 11. Co vs. Ni relationships in magnetite. Regression line (dashed) for magnetite-rich samples from Site 1 and 3 shows linear relationship between Co and Ni.

Table 6

Trace element composition of magnetite (LA-ICP-MS).

Location		Site 1			Site 1			Site 2		
Sample		CO14			LIC14			ECL1		
Rock Type		Mag-rich diopsidite			Nodular ore			Fine-grained disseminated ore		
Element (ppm)	DL (ppm) ± 2s	n = 16			n = 16			n = 10		
		min	Max	Median	min	Max	Median	min	Max	Median
^{25}Mg	11 ± 7	9357	11350	10216	21021	29568	24112	6149	7259	6696
^{29}Si	1020 ± 1895	<1020	1348	<1020	BDL			<1020	1572	<1020
^{43}Ca	325 ± 93	BDL			BDL			BDL		
^{47}Ti	6 ± 4	42	75	59	44	214	182	396	635	570
^{51}V	0.3 ± 0.2	13	43	23	5	81	29	7	30	17
^{53}Cr	8 ± 3	BDL			BDL			<8	154	32
^{55}Mn	4 ± 1	3669	4246	4025	4318	5360	4991	2558	2706	2620
^{59}Co	0.3 ± 0.2	376	411	393	540	603	565	74	86	78
^{60}Ni	8 ± 5	175	257	223	9	256	82	413	482	429
^{66}Zn	2 ± 1	100	125	109	117	173	157	96	104	101
^{98}Mo	0.5 ± 0.3	BDL			<0.5	1.3	<0.5	<0.5	0.2	<0.5
^{90}Zr	0.1 ± 0.1	BDL			<0.1	0.7	<0.1	0.1	0.6	0.3
Co/Ni				1.8			6.9			0.2

Location		Site 2			Site 3			Site 3		
Sample		CRY1			LAR2A			CGN3		
Rock Type		Vein ore			Mag-rich pegmatoid serpentinite			Di-rich nodular ore		
Element (ppm)	DL (ppm) ± 2s	n = 14			n = 25			n = 13		
		min	Max	Median	min	Max	Median	min	Max	Median
^{25}Mg	11 ± 7	7773	8481	8146	4173	8150	5629	5992	6945	6311
^{29}Si	1020 ± 1895	BDL			<1020	2303	<1020	BDL		
^{43}Ca	325 ± 93	BDL			BDL			BDL		
^{47}Ti	6 ± 4	54	387	263	227	435	315	41	108	70
^{51}V	0.3 ± 0.2	<0.3	135	5	40	118	64	<0.3	33	6
^{53}Cr	8 ± 3	<8	14	<8	<8	64	<8	BDL		
^{55}Mn	4 ± 1	2903	3086	2984	2927	3394	3154	2797	3016	2940
^{59}Co	0.3 ± 0.2	132	171	151	316	365	332	264	289	273
^{60}Ni	8 ± 5	80	726	484	505	762	672	49	111	89
^{66}Zn	2 ± 1	133	195	163	46	103	96	70	80	77
^{98}Mo	0.5 ± 0.3	BDL			<0.5	1.3	<0.5	<0.5	1.8	1.1
^{90}Zr	0.1 ± 0.1	nd			<0.1	2.1	0.1	<0.1	1.7	0.4
Co/Ni				0.3			0.5			3.1

s = sample standard deviation.

BDL = below detection limit.

nd = not determined.

4.6. Thermodynamic modelling

I attempted to reproduce the mineral assemblages observed at Cogne in a model seafloor hydrothermal system. The fluids produced by interaction at 400°C of modified seawater with harzburgite and Fe-gabbro (Table 2), respectively, provide two potential endmember compositions for fluids circulating in and reacting with the original oceanic substrate rocks. Harzburgite composes the uppermost part of the Cogne deposit and is the most common type of abyssal peridotite (Mével, 2003). Fe-gabbro is the most Fe-rich rock that can be found in the ophiolitic units of southern Valle d'Aosta (Benciolini et al., 1988; Bocchio et al., 2000; Dal Piaz et al., 2010; Polino et al., 2014) and it can be an efficient source of iron if altered at high temperature. Based on these calculations, dissolved Fe in the harzburgite-reacted fluid (Fig. 12a) increases from W/R ~1 to W/R ~7 where it reaches a maximum value of ~11 mmol/kg (604 ppm). The increase in Fe concentration follows the pH decrease that is in turn controlled by hydrolysis of mantle orthopyroxene, which is much more reactive than olivine at 400°C (Charlou et al., 2002). In general, the Fe-gabbro-reacted fluids are more acidic and more Fe-rich. The Fe concentration is up to one order of magnitude higher (Fig. 12b), reaching a maximum value of ~26 mmol/kg (1439 ppm) at W/R ~80. Such a high dissolved Fe content again reflects a pH minimum, which immediately follows the total breakdown of plagioclase. This is consistent with experimental evidence that plagioclase alteration to Mg-silicates (chlorite, epidote, talc) by seawater at 400°C and high W/R buffers pH to low values (Seyfried, 1987; Seyfried et al., 2010). Other major differences between the two fluid types at their Fe peak concern the concentrations of Mg and Si, which are about one order of magnitude lower and two order of magnitude higher, respectively, in the Fe-gabbro-reacted fluid. The high W/R ratios required to maximize the Fe contents could potentially be achieved in a highly fractured substrate, such as at the foot wall of a detachment fault in an oceanic core complex (e.g., McCaig et al., 2007).

The harzburgite-reacted and Fe-gabbro-reacted fluids carrying the maximum dissolved Fe were further reacted at either 300°C or 400°C with the different lithologies listed in Table 2. I considered temperatures ≥ 300°C to account for the ubiquitous presence of antigorite (predominant at T > 300°C; Evans, 2004, 2010) in all ore assemblages at Cogne and because these high temperatures disfavour substitution of Fe for Mg in minerals (especially in brucite; Klein et al., 2009), thus accounting for the very high $100 \cdot Mg/(Mg+Fe)_{mol}$ ratios (Mg# > 90) of gangue minerals in the Cogne deposit (Table 3). Moreover, at the high temperatures considered, and especially at high W/R ratios, the thermodynamic properties of the very Mg-rich gangue minerals are well approximated by their Mg endmembers, hence neglecting solid solutions can be considered to be a minor problem. The only mineral phase that significantly deviates from the ideal composition is lizardite, which is always Al-rich (Table 3). However, textural evidence indicates that lizardite is a minor relict phase that was formed during an early serpentinization event and rarely survived the successive higher temperature ore-forming process (cf. section 4.2). Accounting for the presence of Al-rich lizardite would not have significantly influenced the modelling of the fluid-rock system at high temperature.

The mineral assemblages produced by hydrothermal fluid-rock interactions are shown in Fig. 13. Magnetite is stable for both fluids over the whole considered W/R range at both 300°C and 400°C (with the exception of fresh troctolites reacting with harzburgite-reacted fluid at 300°C). Under *rock-dominated conditions* (W/R <1), the final alteration mineral assemblages are similar for both fluids: forsterite and brucite are generally formed in addition to magnetite, but their stability is dependent on temperature, with forsterite being stable at higher temperature (Fig. 13b, d) than brucite (Fig. 13a, c). Fayalite is predicted to form at both 300°C and 400°C in fresh troctolites and pegmatoid serpentinites. The presence of pure fayalite may be an artefact induced by neglecting solid solutions in olivine. Clinochlore is present in all mineral assemblages at 400°C (with the exception of the model of a fresh dunite reacting with harzburgite-reacted fluid), but at 300°C it forms in abundant quantities only in troctolites (both fresh and serpentinized) and pegmatoid serpentinites. Diopside is abundant only in Ca-rich rocks, i.e. harzburgites and troctolites (Table 2), and in troctolites it is associated with

tremolite. In these rocks also minor anhydrite forms. At 300°C in fresh harzburgites and serpentinized dunites the diopside is soon destabilized and the liberated Mg and Si combine with dissolved Al to form clinochlore. At higher temperatures this reaction is limited to higher W/R ratios. Some phlogopite is produced during alteration of fresh troctolites. At *intermediate W/R ratios*, diopside disappears at both 300°C and 400°C. In troctolites, diopside breakdown is accompanied by an increase in the modal amount of tremolite (and fayalite at 300°C). In serpentinized harzburgites, diopside reacts at 300°C with brucite and magnetite to form andradite and antigorite (cf. reaction n. 44 in Frost and Beard, 2007; Fig. 13a, c). Talc becomes abundant in pegmatoid serpentinites at 400°C, but at 300°C it only forms when the rocks react with Fe-gabbro derived fluid. Formation of talc is enhanced by the low pH, high Si and low Ca activities of the Fe-gabbro-reacted hydrothermal fluid. At *high W/R ratios*, in both fresh and serpentinized dunites and harzburgites, brucite reacts with either the harzburgite-reacted fluid or the Fe-gabbro reacted fluid to form antigorite or clinochlore, respectively. Talc is formed in Si-rich systems, i.e. those involving Si-rich lithologies (troctolites, pegmatoid serpentinite) or fluids (Fe-gabbro-reacted fluids). In the systems dominated by Fe-gabbro-reacted fluids, talc replaces forsterite and antigorite, thus forming talc + magnetite + clinochlore assemblages.

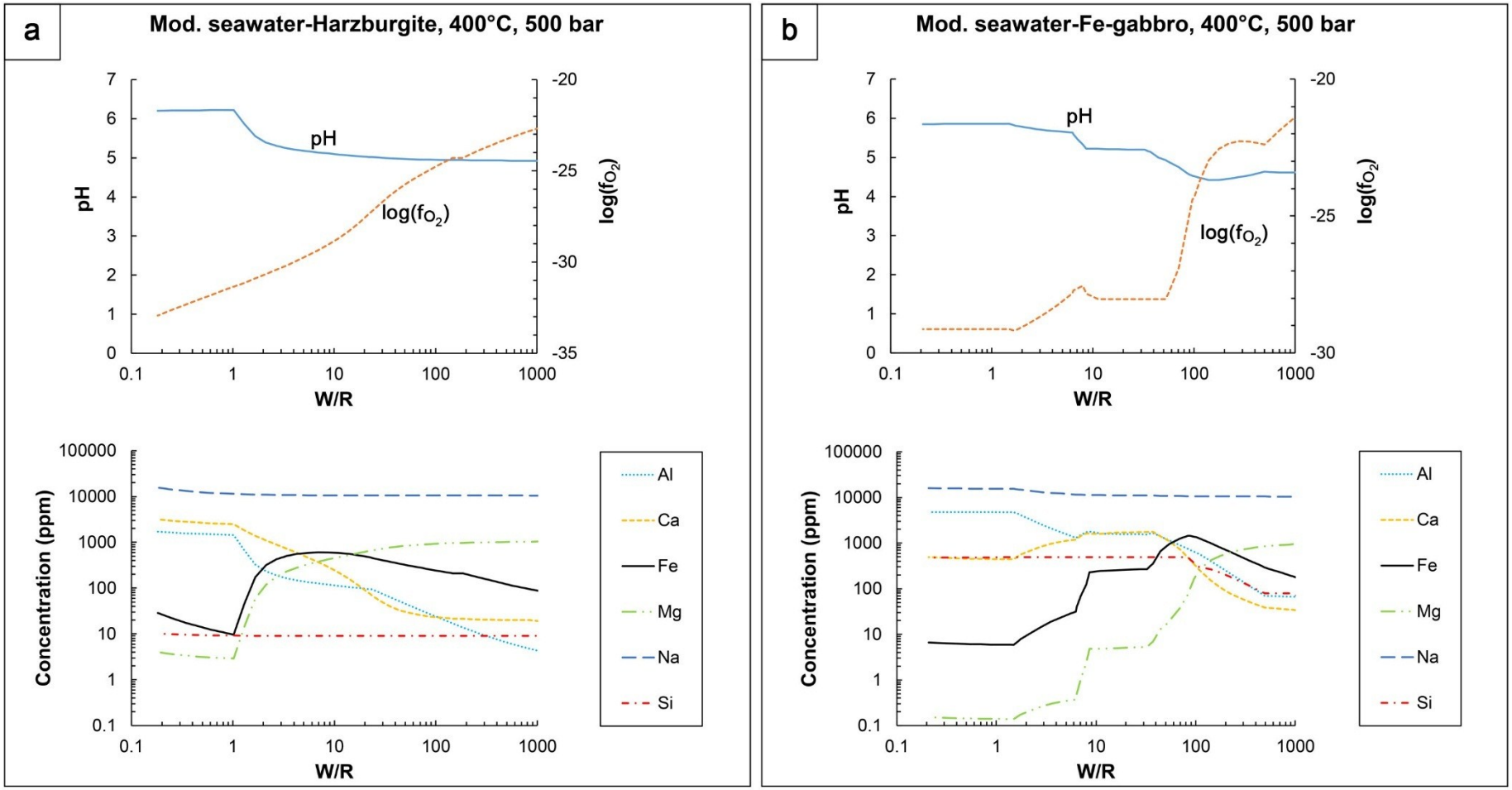

Fig. 12. Variation in pH, f_{O_2} and element concentrations in modified seawater equilibrated with harzburgite (a) or Fe-gabbro (b) at 400°C at various W/R.

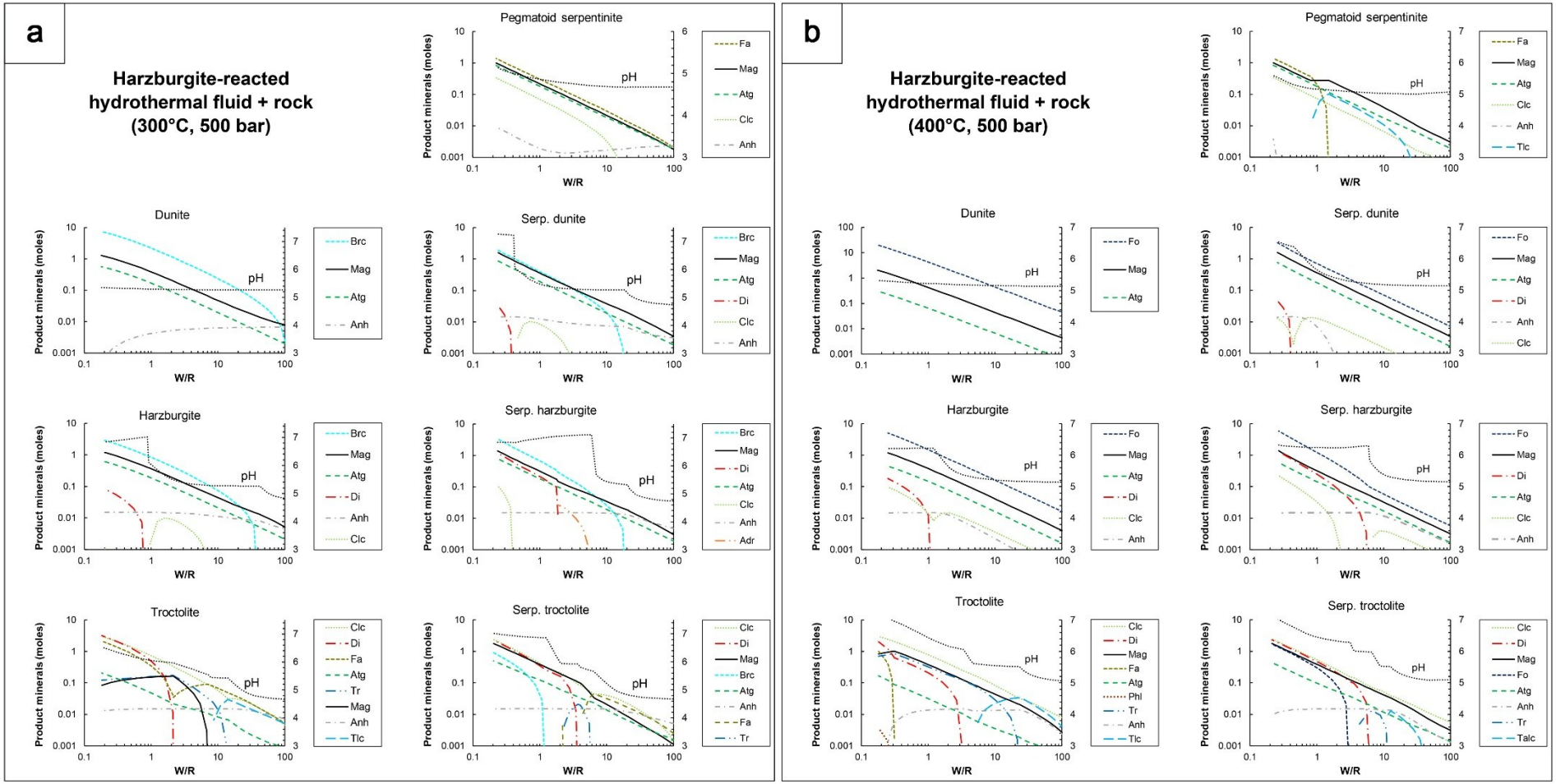
a
Harzburgite-reacted hydrothermal fluid + rock (300°C, 500 bar)
Pegmatoid serpentinite
Dunite
Serp. dunite
Harzburgite
Serp. harzburgite
Troctolite
Serp. troctolite
b
Harzburgite-reacted hydrothermal fluid + rock (400°C, 500 bar)
Pegmatoid serpentinite
Dunite
Serp. dunite
Harzburgite
Serp. harzburgite
Troctolite
Serp. troctolite
Product minerals (moles)
W/R
pH

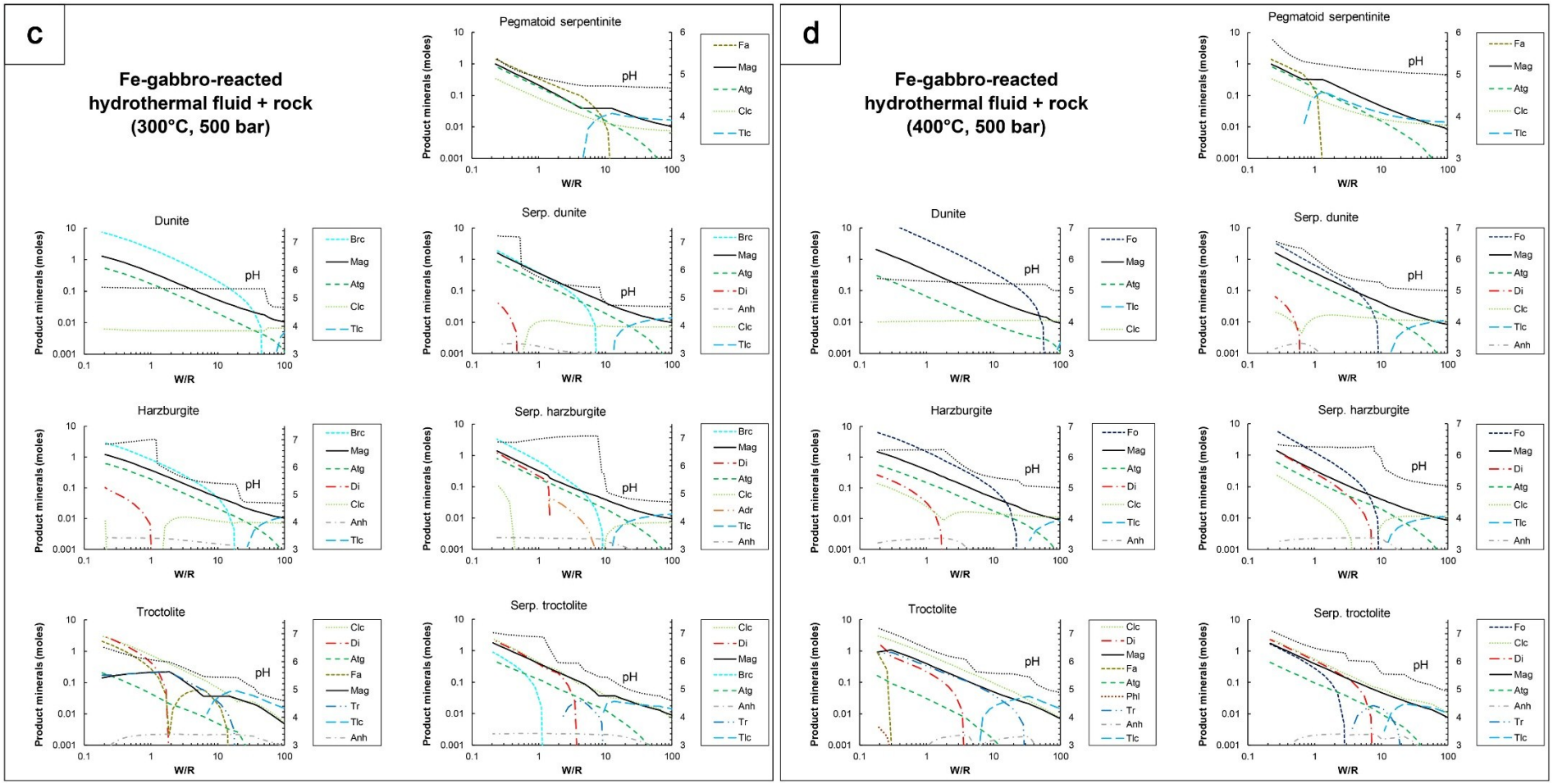

Fig. 13. Mineral assemblages and variation in pH produced by reaction of model hydrothermal fluids with selected rock types. Harzburgite-reacted fluid reacting with rocks at a) 300°C and 500 bar b) 400°C and 500 bar. Fe-gabbro-reacted fluid reacting with rocks at c) 300°C and 500 bar d) 400°C and 500 bar.

5. Discussion

5.1. Cogne as an ultramafic-hosted subseafloor hydrothermal deposit

5.1.1. Constraints from magnetite geochemistry and ocean seafloor studies

Important clues about the origin of the Cogne magnetite can be derived from the comparison with existing published datasets for magnetite from various genetic environments. The Cogne magnetite is poor in Ti and Cr (<640 ppm and <150 ppm, respectively), which is a typical feature for hydrothermal magnetite (Fig. 14). In fact, based on the data compiled by Dare et al. (2014), hydrothermal magnetite can be distinguished from magmatic magnetite, because the former has generally low Ti contents (<10000 ppm) and high Ni/Cr ratios (≥1), in virtue of the higher mobility of Ni in aqueous fluids. Cogne magnetite is also poor in V (<140 ppm) and rich in Mn (>2500 ppm), similar to hydrothermal magnetite from skarn deposits (Fig. 15). However, the Cogne magnetite ore was not emplaced in carbonate rocks but in mantle serpentinites, as testified by the geochemical and textural features of the host rocks.

Serpentinization of peridotites can produce magnetite that is depleted in Cr, Ti, V and Ni compared to the primary magmatic magnetite (Boutroy et al., 2014). However, serpentinization alone cannot account for the amount of magnetite observed in most of Cogne rocks. In fact, magnetite production during serpentinization is limited by the amount of FeO available in the peridotite, which is commonly less than 10 wt% (Bodinier and Godard, 2003). Therefore, an efficient mechanism of mobilization and concentration of Fe is needed to explain the formation of the Cogne deposit.

Low-T (100-300°C) hydrothermal fluids causing peridotite serpentinization at high W/R can leach Fe from the peridotite and precipitate it as magnetite in veins (up to a few cm-thick), as reported for the Bou Azzer ophiolite, Morocco (Gahlan et al., 2006). However, the compositions of Bou Azzer

vein magnetites, although considerably depleted in trace elements as a consequence of their low formation temperatures (Nadoll and Koenig, 2011), are very different from those of Cogne magnetites. The latter have higher Co/Ni ratios (0.2-67 vs. 0.004-0.12) and are richer in Mn (2600-5000 vs. 400-470 ppm), Zn (80-160 vs. 3-20 ppm) and Mg (5600-24000 vs. 97-1000 ppm). These differences suggest that the formation of Cogne magnetite took place under substantially dissimilar physicochemical conditions.

Some indications on the various factors that controlled the composition of Cogne magnetite can be derived from the PCA (Fig. 10). The PC1 clearly discriminates high-(Mg, Mn, Co, Zn) magnetites in nodular ores and diopsidites from high-(Ni, V, Ti) magnetites in fine-grained disseminated ore and in magnetite-rich pegmatoid serpentinite. The relatively low Mn, Co and Zn contents in the host rocks and the fluid-compatible nature of these metals suggests that the composition of the high-(Mg, Mn, Co, Zn) magnetites was controlled by an externally-buffered fluid (cf. Dare et al., 2014; Nadoll et al., 2014). The high Co/Ni ratios of these magnetites (Table 6) also support this hypothesis, because it would suggest a mafic metal source (cf. Melekestseva et al., 2013), which is in contrast with the ultramafic nature of most of the Cogne host rocks. On the contrary, the high-(Ni, V, Ti) magnetites are more enriched in elements that are weakly mobile and/or relatively abundant in the host rocks, suggesting formation under rock-buffered conditions (cf. Nadoll et al., 2014). The PC1 may thus be interpreted as reflecting magnetite formation under different W/R ratios from possibly similar parent fluids. The PC2 further discriminates between the different host rocks (i.e. high-V magnetite in pegmatoid serpentinite and high-Ti magnetite in serpentinized mantle peridotites). Magnetite in veins shows intermediate geochemical features between hydrothermal fluid-buffered and host rock-affected compositions.

Hydrothermal fluids carrying a significant load of transition metals (high Fe, Mn, Cu, Zn ± Co ± Ni) issue from ultramafic substrates in high-T (>350°C) hydrothermal systems associated with oceanic core complexes in slow-spreading mid-oceanic ridges, such as at Rainbow and Logatchev on the Mid-Atlantic Ridge (Douville et al., 2002; Andreani et al., 2014). In particular, the hydrothermal

vent fluids at Rainbow are the richest in Co (Douville et al., 2002), have the highest Co/Ni ratios (~4) and are probably saturated in magnetite + chlorite + talc (Seyfried et al., 2011). The surveyed portion of the Rainbow hydrothermal deposit is almost entirely made up of sulphides (Fouquet et al., 2010; Marques et al., 2006, 2007), as expected for the upper part of a seafloor hydrothermal system, where the hot hydrothermal fluid mixes with seawater (Janecky and Seyfried, 1984). Notwithstanding this, at Rainbow, hydrothermal magnetite is locally abundant in serpentinites hosting sulphide stockworks and in semi-massive sulphides, where magnetite sometimes replaces pyrite (Marques, 2005). Magnetite forming coarse-grained disseminations in the serpentinites that host stockworks at Rainbow precipitated later than the sulphides during a distinct hydrothermal stage (Marques et al., 2006) and, notably, has a similar geochemical fingerprint as magnetite in fine-grained disseminations in serpentinized peridotite at Cogne (the concentrations of the trace elements, with the exception of Si, are in the same order of magnitude). Recently, Yıldırım et al. (2016) described a hydrothermal magnetite mineralization in a non-metamorphic volcanogenic massive-sulphide (VMS) deposit from the Upper Triassic-Upper Cretaceous Koçali complex, a Tethyan ophiolite in Turkey. These findings and the above observations support the possibility that Cogne magnetite has directly formed in a seafloor hydrothermal system. The presence of a positive magnetic anomaly at Rainbow has been ascribed to a ~$2 \cdot 10^6$ m^3 magnetite-rich stockwork zone (Szitkar et al., 2014). If this volume was entirely composed of magnetite, it would correspond to 10 Mt of mineral, which is on the same order of magnitude as the estimated amount of magnetite at Cogne (~12 Mt). It is worth noting that the Rainbow hydrothermal system is still highly active (Fouquet et al., 2010) and its vent fluids are magnetite-saturated (Seyfried et al., 2011). It can thus be inferred that the Rainbow hydrothermal system may eventually produce at depth a magnetite deposit of comparable size as Cogne.

In such a scenario, the general scarcity of sulphides at Cogne, along with their presence in the veins above the main magnetite bodies, suggest that the exposed mineralized section represents the deep segment of a seafloor, ultramafic-hosted, high-temperature hydrothermal system, which was possibly associated with shallower, now eroded, sulphide-rich bodies. According to this

interpretation, the magnetite + sulphide veins and fine-grained disseminations in the hangingwall serpentinite (Site 2) may mark the transition between the magnetite-rich and the sulphide-rich portions of the hydrothermal system (Fig. 16).

5.1.2. Geological, geochronological and textural constraints

The Cogne mantle peridotites underwent complete serpentinization at 200-300°C beneath the seafloor of the Jurassic Piedmont-Liguria ocean (Carbonin et al., 2014). The radiometric data on magnetite-associated uraninite (152.8 ± 1.3 Ma) presented above places the ore-forming event in proximity of the Kimmeridgian-Tithonian boundary (152.1 ± 0.9 Ma). This age overlaps with that of the spreading of the Piedmont-Liguria ocean, as inferred by biochronological dating of supra-ophiolitic deep-sea sediments (radiolarites), whose oldest ages span from Late Bajocian to Middle Bathonian (~ 168 Ma; Cordey et al., 2012), and by radiometric dating of magmatic rocks, which places the latest magma pulses (mainly plagiogranites) in the Western Alps and Liguria in the Kimmeridgian-Tithonian (~157.3 ± 1.0 - ~145.5 Ma; Lombardo et al., 2002; Manatschal and Müntener, 2009 and references therein).

Very little information can be obtained about the original lithological and thermal structure of the oceanic lithosphere at Cogne, because of the limited exposure. Some indirect information can be obtained from the nearby Mt. Avic serpentinite massif (Fig. 1). Although located in a different structural position in the orogen (see Dal Piaz et al., 2010), the Mt. Avic massif provides the most complete section of the oceanic lithosphere of the Alpine Tethys in the southern Valle d'Aosta region. In the Mt. Avic massif, dominant serpentinized mantle peridotites, associated with gabbroic intrusions (Mg-metagabbros), rodingitic dykes, minor Fe-Ti-oxide metagabbros and other metabasites (Dal Piaz et al., 2010; Fontana et al. 2008, 2015; Panseri et., al 2008), are thought to have been exposed on the seafloor in an oceanic core complex (Tartarotti et al., 2015). This is consistent with the proposed slow- to ultra-slow nature of the Piedmont-Liguria ocean (Manatschal et al., 2011;

Manatschal and Müntener, 2009; Piccardo et al., 2008). Jurassic magmatic activity in the Mt. Avic massif was sufficient to sustain high-temperature hydrothermal convection cells, as testified by widespread, small, massive sulphide (Cu-Fe-Zn) deposits, which are mostly associated with metabasites (Castello et al., 1980; Castello, 1981; Martin et al., 2008; Dal Piaz et al., 2010; Fantone et al., 2014) and are thought to have formed in the seafloor (Martin et al., 2008). The distinctive enrichment in Co and Cu observed in Cogne nodular and vein magnetite ores, respectively, as well as the low Ni content in all magnetite ore types, suggests a contribution from mafic sources or a combined contribution from ultramafic and mafic sources, as observed in some ultramafic-hosted, mid-ocean ridge, hydrothermal deposits (e.g. Rainbow, Fouquet el al., 2010; Marques et al., 2006; Semenov, Melekestseva et al., 2014) and in other ultramafic-hosted VMS deposits in ophiolitic belts (Melekestseva et al., 2013). In analogy with these modern and ancient examples, also at Cogne the presence of deep magmatic intrusions (gabbro) would be required to provide heat and suitable chemical conditions (low pH) to produce metal-rich fluids (e.g., Marques et al., 2006; Seyfried et al., 2011). Gabbroic intrusions, mainly represented by gabbros and Fe-Ti gabbros, are not observed in the small Cogne unit, but are common in the wider Mt. Avic area (see above) and in the other ophiolitic units in southern Valle d'Aosta (Grivola-Urtier and Zermatt-Saas units; Benciolini et al., 1988; Bocchio et al., 2000; Dal Piaz et al., 2010; Polino et al., 2014). Therefore, I infer that similar rock types could have occurred also at Cogne in the original oceanic lithosphere section.

The texture, geochemistry (low Co/Ni, high Cr) and relict mineralogy (bastites, Mg-Al-rich chromite) of Site 2 magnetite-enriched serpentinites suggest that the host rock was a mantle harzburgite, with composition comparable with that of modern abyssal peridotites. However, chemical and textural evidence from both Site 1 and Site 3 indicates that part of the hydrothermal ore was emplaced in more atypical serpentinites, which exhibit a ghost pegmatoid texture marked by interlobate domains separated by coronitic structures (Fig. 4f). Similar textures have been described in some troctolites from modern oceanic and ancient ophiolitic settings (Blackman et al., 2006; Renna and Tribuzio, 2011). These rocks are interpreted to have formed from melt-impregnation and melt-

peridotite reactions, which dissolved orthopyroxene and partially dissolved olivine producing rounded or embayed grain boundaries (Drouin et al., 2009; Renna and Tribuzio, 2011; Suhr et al., 2008). In particular, olivine-rich troctolites originating from melt-peridotite reactions are usually coarse-grained and can show a harrisitic texture (Renna and Tribuzio, 2011), which is reminiscent of the "harrisitic" texture of some nodular ores at Cogne. This suggests that many, if not most, nodular ores at Cogne formed by hydrothermal alteration of original serpentinized troctolites, with magnetite preferentially replacing the original olivine domains.

5.1.3. Insights from thermodynamic modelling

From a qualitative point of view, interaction of various types of fresh or serpentinized mantle rocks with either a harzburgite-reacted fluid at intermediate to high W/R or a Fe-gabbro-reacted hydrothermal fluid at intermediate W/R (Fig. 13) can produce mineral assemblages made of magnetite + antigorite + clinochlore ± brucite (at 300°C) ± forsterite (at 400°C), which resemble the most common mineral assemblages in the Cogne magnetite ores. However, even when the natural mineral assemblage is qualitatively reproduced, the calculated modal magnetite content invariably remains too low to produce a magnetite ore. This indicates that the model fluids are not sufficiently Fe-rich to account for the formation of the Cogne deposit. Note that a Rainbow-type fluid (Table 7) would produce broadly similar mineral assemblages as the model fluids, since its Na, Mg, Si, Fe, Cl concentrations are fairly similar. I could not envisage any other reasonable substrate lithology which could have released significantly higher Fe to the hydrothermal fluids under reasonable conditions. This suggests that additional processes other than simple seawater/rock reactions have played a role in the formation of the magnetite parent fluids.

One such process could be phase separation in the hydrothermal fluid, which could have produced brines enriched in weakly volatile Fe. Phase separation is commonly invoked to explain the wide chlorinity range observed in modern seafloor hydrothermal vent fluids (e.g., Bischoff and

Rosenbauer, 1987; Charlou et al., 2002; Douville et al., 2002; Foustoukos and Seyfried, 2007; Seyfried et al., 2011; Pester et al., 2014). A higher chlorinity would enhance solubility of metals as chloride complexes. At the same time, H_2S partitioning into the vapour phase would cause sulphide undersaturation in the brine (Bischoff and Rosenbauer, 1987; Von Damm, 2004; Seyfried et al., 2004; Seyfried at al., 2010; Fouquet et al., 2010), thus delaying sulphide precipitation. This is in agreement with the general scarcity of sulphides in the Cogne magnetite ores. The presence of chalcophile metals in the fluid is still testified by Cu sulphides in magnetite veins from Site 2. In this case, the transition from bornite + magnetite to chalcopyrite + magnetite assemblages suggests a progressive variation in the parent fluids towards higher H_2S activity or lower Cu/Fe ratios (cf. Seyfried et al., 2004, 2010).

Another process which could potentially lead to enhanced Fe concentrations in the fluid is the incorporation of a magmatic gaseous component, which could promote acidification and thus increase Fe solubility (cf. de Ronde et al., 2011; Berkenbosch et al., 2012). However, assuming a gas composition similar to that of gases emitted from mafic lavas (Erta 'Ale volcano, Ethiopia; Sawyer et al., 2008), it can be calculated that a relatively high condensed gas/fluid mass ratio of 1:10 would increase the Fe concentrations only by a factor of ~2.3. This increase is too small to allow a significant increase in the final amount of precipitated magnetite. Therefore, phase separation remains the most likely hypothesis.

Another feature that is not explained by my models is the diopside-rich gangue observed at Site 3. Textural relationships suggest that diopside formed during a late stage of magnetite mineralization, most likely from a fluid with higher pH and/or higher Ca^{2+} activity (see Fig. 9 in Bach and Klein, 2009). This fluid could have derived from serpentinization of country peridotites and troctolites, and may thus have some affinity with rodingite-forming fluids. Alternatively, a higher Ca content could result from more extensive interaction with gabbroic rocks. The possible role of gabbroic rocks in producing Ca-Si-(Al)-rich fluids has been suggested, for instance, for fluids responsible for strong calcic metasomatism in fault zones in modern oceanic core complexes (Boschi et al., 2006).

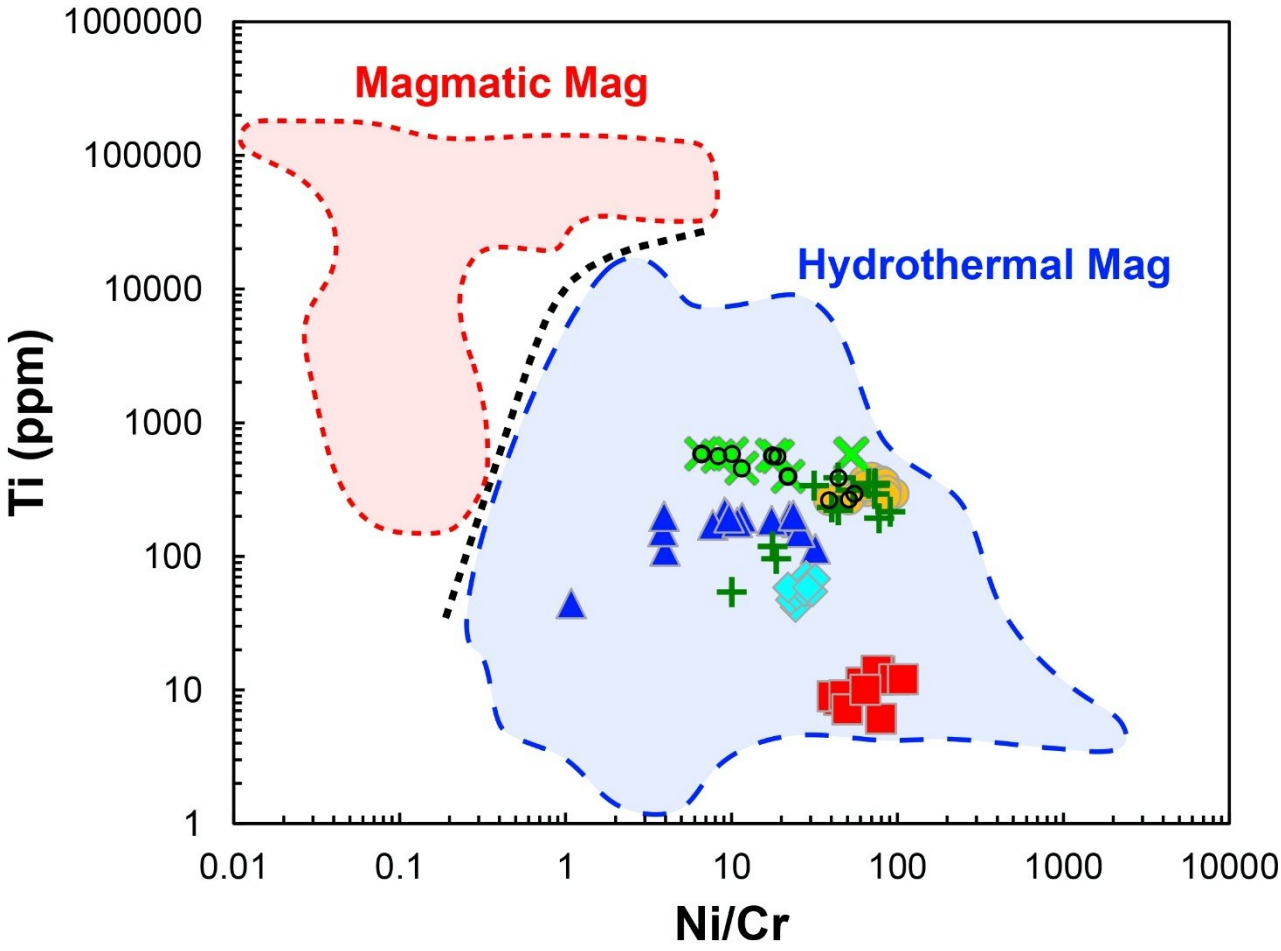

Fig. 14. Compositions of Cogne magnetites plotted in the discrimination diagram by Dare et al., 2014. Magnetites with Cr contents above detection limit are circled. The other data points are plotted assuming a Cr value equal to the detection limit of 8 ppm. Although this may have unduly shifted the points to lower Ni/Cr ratios, the strong hydrothermal character of the Cogne magnetites remains evident. Symbols as in Fig. 11.

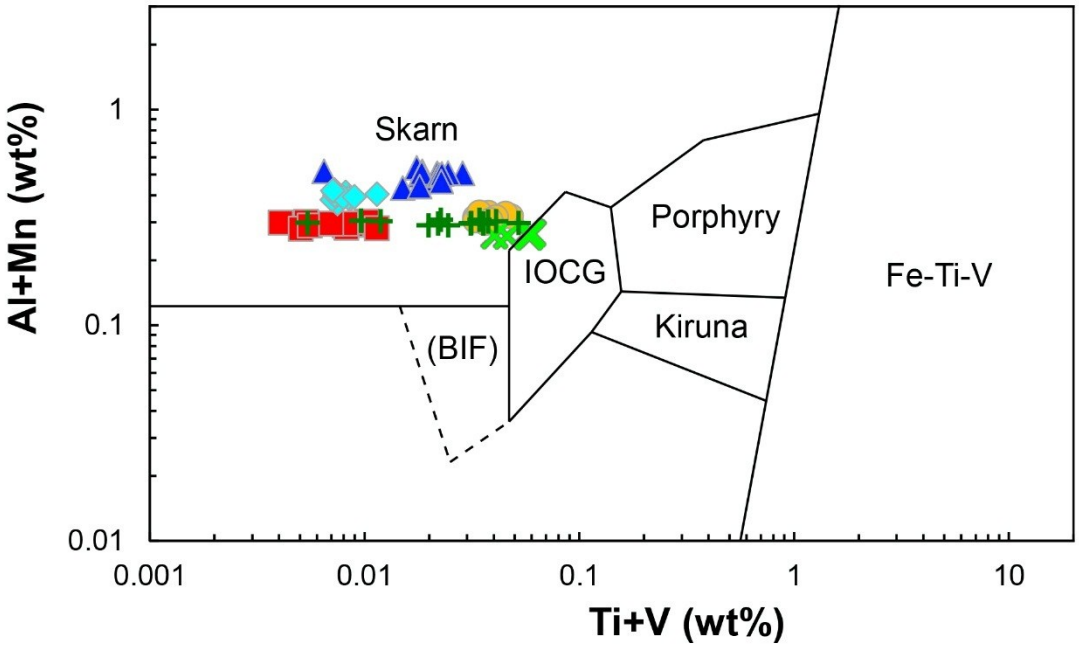

Fig. 15. Compositions of Cogne magnetites in the discrimination diagram of Dupuis and Beaudoin, 2011. LA-ICP-MS data are not available for Al (generally <<0.1 wt% based on EPMA data), therefore the plotted (Mn + Al) contents should be considered as minimum values. Symbols as in Fig. 11.

Table 7

Composition of model hydrothermal fluids and the Rainbow vent fluid (mmol/kg solution).

	Harzburgite-reacted	Fe-gabbro-reacted	Rainbow
Na	460.2	464.4	570.0
Ca	9.2	12.0	67.7
Mg	15.6	3.1	1.7
Si	0.3	17.5	7.3
Fe	10.8	25.8	22.2
Al	4.7	27.6	0.0029
Cl^-	535.4	527.3	757.0

5.2. Alternative hypotheses

As ultramafic rocks in ophiolitic massifs often contain accumulations of chromite (e.g., Bédard and Hébert, 1998), a potential origin of magnetite in Sites 1 and 3 could be by leaching of Cr from former chromitite bodies. Indeed, Cr appears to be mobile during high-temperature (>500-550°C) peridotite-water interactions, as shown by Arai and Akizawa (2014) for the Oman ophiolite. Also, in the Mt. Avic massif, some small-scale magnetite ores were apparently formed after former chromitites (Diella et al., 1994; Rossetti et al., 2009). There are two lines of evidence against this hypothesis for the Cogne magnetite. First, in the Mt. Avic ores, chromite is still preserved in the cores of the magnetite grains (Diella et al., 1994; Fontana et al., 2008; Rossetti et al., 2009), whereas neither chromite relicts nor Cr-rich magnetite cores are found in nodular and vein ores at Cogne. Second, there is no evidence for a high-temperature alteration at Cogne such as that described in the Oman ophiolite by Arai and Akizawa (2014). At the temperatures under which serpentinization and successive hydrothermal metasomatism at Cogne took place (200-300°C and 300°-400°C, respectively; Carbonin et al., 2014), Cr is essentially immobile and any Cr dissolved at higher temperatures deeper in the system should be precipitated (Arai and Akizawa, 2014). The immobility of Cr during magnetite mineralization is testified by the mantle peridotites containing the fine-grained disseminated magnetite from Site 2, which have similar Cr contents as their magnetite-poor counterparts (Fig 6). In these rocks, the original Mg-Al-rich chromite (the main source of Cr) was replaced *with no Cr loss* by Fe-rich chromite + Cr-rich chlorite, according to reactions of the type

$2(Mg,Fe)(Al,Cr)_2O_4 + 3/2(Mg,Fe,Al)_3Si_2O_5(OH)_4 + H_2O + 1/12\ O_2 \rightarrow$

Mg-Al-rich chromite serpentine

$(Mg,Fe,Al,Cr)_5(Si_3Al)O_{10}(OH)_8 + 7/6(Mg,Fe)(Cr,Fe,Al)_2O_4$

Cr-rich chlorite Fe-rich chromite

(cf. Mellini et al., 2005; Merlini et al., 2009), and then overgrown by Cr-poor magnetite (Fig. 5d). The P-T conditions for the subsequent Alpine metamorphism at Cogne are not precisely known. However, assuming a typical subduction geothermal gradient (<10°C/km), the coexistence of lizardite and antigorite in both serpentinized peridotites and pegmatoid serpentinites suggests temperatures not exceeding 390°C (Schwartz et al., 2013), which are too low to determine significant mobilization of Cr.

Iron (Mn) oxide/oxyhydroxides (hematite and goethite) and Fe sulphide deposits are the most common forms of Fe accumulation in modern seafloor hydrothermal settings (e.g., Rona, 1988). In principle, magnetite may form by reduction and dehydration of Fe-oxide/oxyhydroxides or by desulphurization of Fe-sulphides during metamorphism. However, the geochronological data collected here demonstrate that the magnetite-forming event was coeval with the spreading of the Piedmont-Liguria ocean and thus predates Alpine metamorphism. Also the geochemistry of Cogne magnetite ores and associated rocks contradicts the metamorphic hypothesis. In fact, in Fe-oxyhydroxides accumulations an enrichment in trace elements such as P and Sr is typically observed (e.g., Puteanus et al., 1991; Hekinian et al., 1993). A similar enrichment is indeed preserved in seafloor hydrothermal Mn-(Fe) deposits in southern Valle d'Aosta ophiolites (median P_2O_5 = 0.06 wt%, median Sr = 1650 ppm; Tumiati et al., 2010), which were metamorphosed up to eclogite-facies conditions (T = 550 ± 60°C, P = 2.1 ± 0.3 GPa; Martin et al., 2008; Tumiati et al., 2015), but it is not observed in Cogne ores ($P_2O_5 \leq 0.01$ wt%, median Sr = 1.6 ppm). In the same ophiolites, sulphide (pyrite + chalcopyrite) deposits show no evidence of S mobilization and depletion linked to subduction metamorphism (Giacometti et al., 2014). Consistently, serpentinized mantle peridotites overlying the Cogne magnetite orebody are not depleted in S (Table 4).

5.3. The role of the Alpine event

The present structural position of the Cogne serpentinite, the lithological associations and the shape of the orebodies are in part the result of the tectonic activity that accompanied the Alpine orogenesis. The main magnetite orebodies at Site 1 and Site 3 behaved as rigid masses during the early ductile deformation events and they were affected by only low degrees of shear deformation, thus preserving the original textures and the proportions between magnetite and gangue minerals. The Alpine deformation was more intense at Site 2, which was probably located in a peripheral position with respect to the main orebody, where the fine-grained disseminated ores and the associated veins were dismembered into lenses. The Alpine metamorphism did not promote significant magnetite remobilization, as testified by the lack of isotopic resetting in uraninite inclusions in magnetite. The Alpine metamorphism is possibly responsible for the transformation of lizardite into antigorite, which is observed also in rocks that do not contain hydrothermal mineralization (i.e. magnetite-poor serpentinized peridotites and pegmatoid serpentinites). In any case the metamorphic temperatures were not sufficient to cause significant serpentine dehydration, since neoblastic forsterite is not widespread and is only found within the nodular ore at Site 1. The restriction of neoblastic forsterite to this specific site suggests that its formation could be related to higher temperature conditions (~400°C) being attained locally during the magnetite hydrothermal event, rather than to the subsequent metamorphism. Based on the above considerations, I conclude that Alpine metamorphism did not play a significant role in concentrating magnetite, although Alpine deformation may have pulled away portions of the deposit (now exposed at sites 1, 2 and 3) that could have been much closer to one another in their original oceanic setting.

5.4 Stages of formation of the Cogne deposit

Considering all available data, I propose the following sequence of events for the formation of the Cogne deposit (Fig. 16):

1) Formation of an oceanic core complex made of mantle peridotites, containing bodies of gabbros and Cr-poor melt-impregnated peridotites (troctolites).

2) Extensive low-temperature serpentinization, producing lizardite serpentinites containing a first generation of disseminated magnetite (Cr-bearing in mantle peridotites and Cr-free in melt impregnated peridotites). This process probably occurred at high water/rock ratios and determined the complete serpentinization of the primary silicates and an extensive loss of Ca.

3) Production of a high-temperature, Fe-rich hydrothermal fluid by reaction of downwelling seawater with substrate rocks. The involvement of Fe-gabbros in the reaction zone is likely, as this would enhance the content of Fe in the fluid.

4) Phase separation in the upwelling hydrothermal fluid, producing a more Fe-rich brine.

5) Reaction of the upwelling hot brine (~300–400°C) with various lithologies (serpentinites after mantle peridotites and troctolites) at various fluid/rock ratios, producing the dissolution of lizardite and the precipitation of abundant nodular to massive magnetite along with antigorite and clinochlore (± brucite and forsterite). Further upwelling of the magnetite-buffered fluid produced magnetite + Cu-sulphide + antigorite veins and fine-grained disseminations in shallower serpentinites.

6) Circulation of late fluids with higher pH and/or higher Ca^{2+} activity, producing diopside-rich, magnetite-bearing metasomatic rocks.

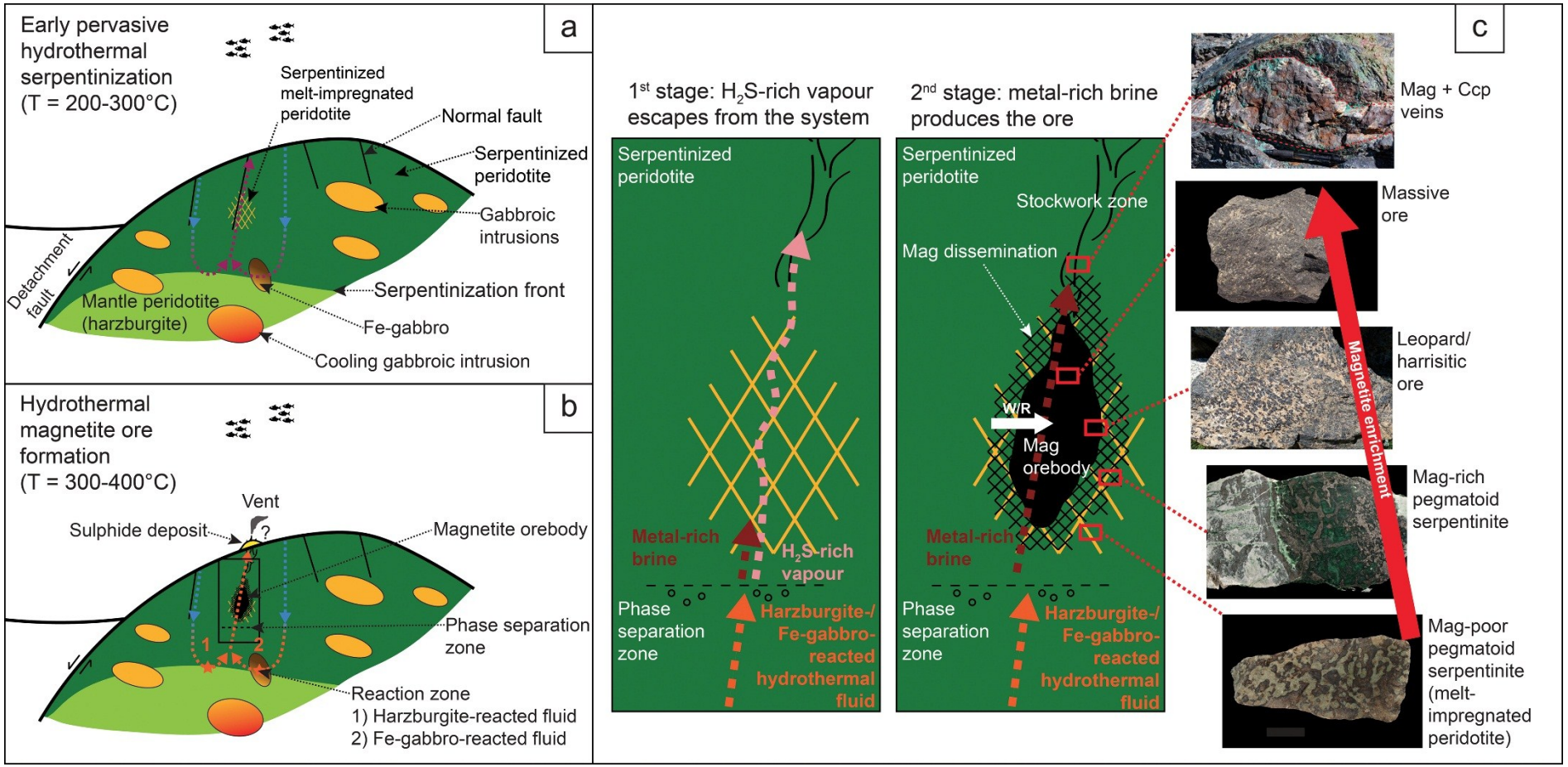
a
Early pervasive hydrothermal serpentinization (T = 200-300°C)
Serpentinized melt-impregnated peridotite
Normal fault
Serpentinized peridotite
Gabbroic intrusions
Detachment fault
Mantle peridotite (harzburgite)
Serpentinization front
Fe-gabbro
Cooling gabbroic intrusion
b
Hydrothermal magnetite ore formation (T = 300-400°C)
Vent
Sulphide deposit
Magnetite orebody
Phase separation zone
1
2
Reaction zone
1) Harzburgite-reacted fluid
2) Fe-gabbro-reacted fluid
1st stage: H2S-rich vapour escapes from the system
2nd stage: metal-rich brine produces the ore
Serpentinized peridotite
Metal-rich brine
H2S-rich vapour
Phase separation zone
Harzburgite-/Fe-gabbro-reacted hydrothermal fluid
Stockwork zone
Mag dissemination
W/R
Mag orebody
c
Mag + Ccp veins
Massive ore
Leopard/ harrisitic ore
Mag-rich pegmatoid serpentinite
Mag-poor pegmatoid serpentinite (melt-impregnated peridotite)
Magnetite enrichment

Fig. 16. Interpreted schematic evolution of the Cogne deposit. a) Formation of an oceanic core complex made up of mantle peridotites intruded by gabbros and Fe-gabbros, and locally impregnated by melts. Early circulation of hydrothermal fluids produces extensive serpentinization at relatively low-T (lizardite stability field). High water/rock ratios are possibly attained thanks to fluid focussing along fractures and faults. b) Convective circulation of seawater produces high-T hydrothermal fluids that leach metals from harzburgites and Fe-gabbros. These fluids undergo phase separation and produce a magnetite-rich body at depth and a sulphide mound on the seafloor. A magnetite-sulphide stockwork zone marks the transition between the magnetite orebody and the sulphide mound. c) Close-up of the framed region in b). Phase separation produces an H_2S-rich vapour that quickly escapes from the system and a dense metal-rich brine. Then, the upwelling brine reacts with the serpentinites at various fluid/rock ratios and precipitates magnetite, producing fine-grained disseminated, nodular and replacive massive ores. Further upwelling of the magnetite-saturated fluids along fractures produce magnetite + chalcopyrite veins (stockwork zone) and fine-grained disseminations in shallower serpentinites.

6. Conclusion

The Cogne magnetite deposit was formed at ~150 Ma by hydrothermal processes during an advanced stage of the opening of the Piedmont–Liguria ocean. Based on geological and petrographic features and on geochemical and mineralogical similarities with some modern ultramafic-hosted VMS deposits on mid-ocean ridges, the exposed mineralized section at Cogne may represent the deep segment of a seafloor, high-temperature (~300–400°C) hydrothermal system, which was possibly associated with shallower, now eroded, sulphide-rich bodies (Fig. 16). As suggested by thermodynamic modelling, simple seawater-rock interactions cannot produce the Fe endowment observed at Cogne. Fractionation processes such as phase separation were probably critical to generate sufficiently Fe-rich hydrothermal fluids capable to precipitate large amounts of magnetite in various types of mantle host-rocks. The possible occurrence of similar ultramafic-hosted magnetite deposits in present-day oceanic settings could contribute to explain the presence of significant magnetic anomalies centred on active and inactive ultramafic-hosted hydrothermal fields (Tivey and Dyment, 2010; Szitkar et al., 2014; Fujii et al., 2016).

Acknowledgements

I thank Raul Carampin (CNR, IGG, Padua) and Andrea Risplendente (Earth Sciences Department, University of Milan) for the technical assistance with the electron microprobe analyses. I'm grateful to Prof. Catherine Mével (Institut de Physique du Globe de Paris) for the constructive discussions when preparing my PhD project and for introducing me to the world of marine geosciences. I also thank Drs. Andreas Klügel and Patrick Monien ("Petrology of the Ocean Crust" research group, University of Bremen, Germany) for providing scientific and technical support during LA-ICP-MS measurements. I thank "Assessorato Territorio e Ambiente" of the Valle d'Aosta region for providing access to the archives of the Cogne mine. A special thank goes to the POC (Petrology of the Ocean Crust, University of Bremen) team (Wolfgang, Karin, Wolf, Christian, Nikki, Andreas, Alex, Bastian, Stefan) for having welcomed me in their group and for making my stay in Bremen a truly beautiful experience. Last but not least, I thank my parents for having supported me during many difficult moments that occurred in these last years.

References

Aitchison J (1986) The statistical analysis of compositional data. Chapman and Hall, New York

Alexandre P and Kyser TK (2005) Effects of cationic substitutions and alteration in uraninite, and implications for the dating of uranium deposits. Can Mineral 43:1005–1017

Andreani M, Escartin J, Delacour A, Ildefonse B, Godard M, Dyment J, Fallick AE, Fouquet Y (2014) Tectonic structure, lithology, and hydrothermal signature of the Rainbow massif (Mid-Atlantic Ridge 36° 14′ N). Geochem Geophy Geosy 15:3543–3571

Arai S, Akizawa N (2014) Precipitation and dissolution of chromite by hydrothermal solutions in the Oman ophiolite: New behavior of Cr and chromite. Am Mineral 99:28–34

Bach W, Klein F (2009) The petrology of seafloor rodingites: insights from geochemical reaction path modeling. Lithos, 112:103–117

Bédard JH, Hébert R (1998) Formation of chromitites by assimilation of crustal pyroxenites and gabbros into peridotitic intrusions: North Arm Mountain massif, Bay of Islands ophiolite, Newfoundland, Canada. J Geophys Res-Sol Ea 103:5165–5184

Benciolini L, Lombardo B, Martin S (1988) Mineral chemistry and Fe/Mg exchange geothermometry of ferrogabbro-derived eclogites from the Northwestern Alps. Neues Jb Miner Abh 159:199–222

Berkenbosch HA, de Ronde CEJ, Gemmel JB, McNeil AW, Goemann K (2012) Mineralogy and formation of black smoker chimneys from Brothers submarine volcano, Kermadec Arc. Econ Geol 107:1613–1633

Berndt ME, Seyfried WE, Janecky DR (1989) Plagioclase and epidote buffering of cation ratios in mid-ocean ridge hydrothermal fluids: experimental results in and near the supercritical region. Geochim Cosmochim Ac 53:2283–2300

Bischoff JL, Rosenbauer RJ (1987) Phase separation in seafloor geothermal systems; an experimental study of the effects on metal transport. Am J Sci 287:953–978

Blackman DK, Ildefonse B, John BE, Ohara Y, Miller DJ, MacLeod CJ and Expedition 304/305 Scientists (2006) Proceedings of the Integrated Ocean Drilling Program, Volume 304/305, College Station, Texas, Integrated Ocean Drilling Program Management International, Inc.

Bocchio R, Benciolini L, Martin S, Tartarotti P (2000) Geochemistry of eclogitised Fe-Ti gabbros from various lithological settings (Aosta Valley ophiolites, Italian western Alps). Protolith composition and eclogitic paragenesis. Period Mineral 69:217–237

Bodinier J-L and Godard M (2003) Orogenic, ophiolitic, and abyssal peridotites. In: Turekian KK and Holland HD (eds) The Mantle and Core: Treatise on Geochemistry, 2nd edn. Elsevier, Oxford, pp 103-167

Boschi C, Früh-Green GL, Delacour A, Karson JA, Kelley DS (2006) Mass transfer and fluid flow during detachment faulting and development of an oceanic core complex, Atlantis Massif (MAR 30°N). Geochem Geophy Geosys 7

Boutroy E, Dare SA, Beaudoin G, Barnes SJ, Lightfoot PC (2014) Magnetite composition in Ni-Cu-PGE deposits worldwide: application to mineral exploration. J Geochem Explor 145:64–81

Bowles JFW (1990). Age dating of individual grains of uraninite in rocks from electron microprobe analyses. Chem Geol 83:47–53

Bowles JF (2015) Age Dating from Electron Microprobe Analyses of U, Th, and Pb: Geological Advantages and Analytical Difficulties. Microsc Microanal 21:1114–1122

Carbonin S, Martin S, Tumiati S, Rossetti P (2014) Magnetite from the Cogne serpentinites (Piemonte ophiolite nappe, Italy). Insights into seafloor fluid–rock interaction. Eur J Mineral 27:31–50

Caruso LJ, Chernosky JV (1979) The stability of lizardite. Can Mineral 17:757–769

Castello P, Dal Piaz GV, Gosso G, Kienast JR, Martin S, Natale P, Nervo R, Polino R, Venturelli G (1980) The Piedmont ophiolite nappe in the Aosta Valley and related ore deposits. In: Gruppo di Lavoro sulle Ofioliti Mediterranee. VI ophiolite field conference, Firenze. Field excursion book, pp. 171–192

Castello P (1981) Inventario delle mineralizzazioni a magnetite, ferro-rame e manganese del complesso piemontese dei calcescisti con pietre verdi in Valle d'Aosta. Ofioliti 6:5–46

Charlou JL, Donval JP, Fouquet Y, Jean-Baptiste P, Holm N (2002) Geochemistry of high H_2 and CH_4 vent fluids issuing from ultramafic rocks at the Rainbow hydrothermal field (36°14′N, MAR). Chem Geol 191:345–359

Cocherie A and Albarede F (2001) An improved U-Th-Pb age calculation for electron microprobe dating of monazite. Geochim Cosmochim Ac 65:4509–4522

Compagnoni R, Elter G, Fiora L, Natale P, Zucchetti S (1979) Nuove osservazioni sul giacimento di magnetite di Cogne in Valle d'Aosta. Rend Soc Min Petr 35:755–766

Compagnoni R, Elter G, Fiora L, Natale P, Zucchetti S (1981) Magnetite deposits in serpentinized lherzolites from the ophiolitic belt of the Western Alps, with special reference to the Cogne deposit (Aosta Valley). In: Proceedings of the Intern. Symp. Mafic and Ultramafic Complexes, Athens, pp 376–394

Cordey F, Tricart P, Guillot S, Schwartz S (2012) Dating the Tethyan Ocean in the Western Alps with radiolarite pebbles from synorogenic Oligocene molasse basins (southeast France). Swiss J Geosci 105:39–48

Cross A, Jaireth S, Rapp R, Armstrong R (2011). Reconnaissance-style EPMA chemical U–Th–Pb dating of uraninite. Austr J Earth Sci 58:675–683

Dal Piaz G, Cortiana G, Del Moro A, Martin S, Pennacchioni G, Tartarotti P (2001) Tertiary age and paleostructural inferences of the eclogitic imprint in the Austroalpine outliers and Zermatt–Saas ophiolite, western Alps. Int J Earth Sci 90:668–684

Dal Piaz GV, Bistacchi A, Massironi M (2003) Geological outline of the Alps. Episodes 26:175-180

Dal Piaz GV, Gianotti F, Monopoli B, Pennacchioni G, Tartarotti P, Schiavo A (2010) Note illustrative della carta geologica d'Italia alla scala 1:50.000 Chatillon F. 91. Ispra-Servizio Geologico d'Italia, Treviso

Dare SA, Barnes SJ, Beaudoin G, Méric J, Boutroy E, Potvin-Doucet C (2014) Trace elements in magnetite as petrogenetic indicators. Miner Deposita 49:785–796

Debret B, Andreani M, Muñoz M, Bolfan-Casanova N, Carlut J, Nicollet C, Schwartz S, Trcera N (2014) Evolution of Fe redox state in serpentine during subduction. Earth Planet Sci Lett 400:206–218

De Giusti F, Dal Piaz GV, Massironi M, Schiavo A (2003) Carta geotettonica della Valle d'Aosta. Mem Sci Geol 55:129–49

Della Giusta A, Carbonin S, Russo U (2011) Chromite to magnetite transformation: compositional variations and cation distributions (southern Aosta Valley, Western Alps, Italy). Period Mineral 80:1–17

de Ronde CEJ, Massoth GJ, Butterfield DA, Christenson BW, Ishibashi J, Ditchburn RG, Hannington MD, Brathwaite RL, Lupton JE, Kamenetsky VS, Graham IJ, Zellmer GF, Dziak RP, Embley RW, Dekov VM, Munnik F, Lahr J, Evans LJ, Takai K (2011) Submarine hydrothermal activity and gold-rich mineralization at Brothers Volcano, Kermadec Arc, New Zealand. Miner Deposita 46:541–584

Di Colbertaldo D, Di Furia E, Rossi F (1967) Il giacimento a magnetite di Cogne in Val d'Aosta. Istituto Lombardo, A101:361–394

Diella V, Ferrario A, Rossetti P (1994) The magnetite ore deposits of the southern Aosta Valley: chromitite transformed during an Alpine metamorphic event. Ofioliti 19:247–256

Ding K, Seyfried WE (1992) Determination of Fe-Cl complexing in the low pressure supercritical region (NaCl fluid): Iron solubility constraints on pH of subseafloor hydrothermal fluids. Geochim Cosmochim Ac 56:3681–3692

Douville E, Charlou JL, Oelkers EH, Bienvenu P, Colon CJ, Donval JP, Fouquet Y, Prieur D, Appriou P (2002) The rainbow vent fluids (36 14′ N, MAR): the influence of ultramafic rocks and phase separation on trace metal content in Mid-Atlantic Ridge hydrothermal fluids. Chem Geol 184:37–48

Drouin M, Godard M, Ildefonse B, Bruguier O, Garrido CJ (2009) Geochemical and petrographic evidence for magmatic impregnation in the oceanic lithosphere at Atlantis Massif, Mid-Atlantic Ridge (IODP Hole U1309D, 30 N). Chem Geol 264:71–88.

Dupuis C, Beaudoin G (2011) Discriminant diagrams for iron oxide trace element fingerprinting of mineral deposit types. Miner Deposita 46:319–335

Edmonds H (2010) Chemical signatures from hydrothermal venting on slow spreading ridges. In: Rona PA, Devey CW, Dyment J, Murton BJ (eds) Diversity of hydrothermal systems on slow spreading ocean ridges, American Geophysical Union, Washington, DC, pp. 27–42

Elter G (1971) Schistes lustrés et ophiolites de la zone piémontaise entre Orco et Doire Baltée (Alpes Graies). Hypothèses sur l'origine des ophiolites. Géologie Alpine 47, 147–169.

Evans BW (2004) The serpentinite multisystem revisited: chrysotile is metastable. Int Geol Rev 46:479–506

Evans BW (2010) Lizardite versus antigorite serpentinite: magnetite, hydrogen, and life (?). Geology 38:879–882

Fantone I, Grieco G, Strini A, Cavallo A (2014) The effect of Alpine metamorphism on an oceanic Cu-Fe sulfide ore: the Herin deposit, Western Alps, Italy. Period Mineral 83:345–365

Filzmoser P, Hron K, Reimann C (2009) Principal component analysis for compositional data with outliers. Environmetrics 20:621–632

Filzmoser P, Hron K (2011) Robust statistical analysis. In: Pawlowsky-Glahn V, Buccianti A (eds) Compositional data analysis. Theory and applications. John Wiley & Sons, Chichester (UK), pp. 59-72

Fontana E, Panseri M, Tartarotti P (2008) Oceanic relict textures in the Mount Avic serpentinites, Western Alps. Ofioliti 33:105–118

Fontana E, Tartarotti P, Panseri M, Buscemi S (2015) Geological map of the Mount Avic massif (Western Alps Ophiolites). Journal of Maps 11:126–135

Fouquet Y, Cambon P, Etoubleau J, Charlou JL, Ondréas H, Barriga FJAS, Cherkashov G, Semkova T, Poroshina I, Bohn M, Donval JP, Henry K, Murphy P, Rouxel1 O (2010) Geodiversity of hydrothermal processes along the Mid-Atlantic Ridge and ultramafic-hosted mineralization: a new type of oceanic Cu-Zn-Co-Au volcanogenic massive sulfide deposit. In: Rona PA, Devey CW,

Dyment J, Murton BJ (eds) Diversity of hydrothermal systems on slow spreading ocean ridges, American Geophysical Union, Washington, DC, pp. 321–367

Foustoukos DI, Seyfried WE (2007) Fluid phase separation processes in submarine hydrothermal systems. Rev Mineral Geochem 65:213–239

Frost BR, Beard JS (2007) On silica activity and serpentinization. J Petrol 48:1351–1368

Fujii M, Okino K, Sato T, Sato H, Nakamura K (2016) Origin of magnetic highs at ultramafic hosted hydrothermal systems: Insights from the Yokoniwa site of Central Indian Ridge. Earth Planet Sci Lett 441:26–37

Gahlan HA, Arai S, Ahmed AH, Ishida Y, Abdel-Aziz YM, Rahimi A (2006) Origin of magnetite veins in serpentinite from the Late Proterozoic Bou-Azzer ophiolite, Anti-Atlas, Morocco: An implication for mobility of iron during serpentinization. J Afr Earth Sci 46: 318–330

Giacometti F, Evans KA, Rebay G, Cliff J, Tomkins AG, Rossetti P, Vaggelli G, Adams DT (2014) Sulfur isotope evolution in sulfide ores from Western Alps: Assessing the influence of subduction-related metamorphism. Geochem Geophys Geosys 15:3808–3829

Govindaraju K (1994) compilation of working values and sample description for 383 geostandards. Geostandard Newslett 18:1–158

Groppo C, Rinaudo C, Cairo S, Gastaldi D, Compagnoni R (2006) Micro-Raman spectroscopy for a quick and reliable identification of serpentine minerals from ultramafics. Eur J of Mineral 18:319–329

Hekinian R, Hoffert M, Larque P, Cheminee JL, Stoffers P, Bideau D (1993) Hydrothermal Fe and Si oxyhydroxide deposits from South Pacific intraplate volcanoes and East Pacific Rise axial and off-axial regions. Econ Geol 88:2099–2121

Hiess J, Condon DJ, McLean N, Noble SR (2012) 238U/235U systematics in terrestrial uranium-bearing minerals. Science 335:1610–1614

Ho PC, Palmer DA, Mesmer RE (1994) Electrical conductivity measurements of aqueous sodium chloride solutions to 600 C and 300 MPa. J Solution Chem 23:997–1018

Ho PC, Bianchi H, Palmer DA, Wood RH (2000) Conductivity of dilute aqueous electrolyte solutions at high temperatures and pressures using a flow cell. J Solution Chem 29: 217–235

Ho PC, Palmer DA, Gruszkiewicz MS (2001) Conductivity measurements of dilute aqueous HCl solutions to high temperatures and pressures using a flow-through cell. J Phys Chem B 105:1260–1266

Jaffey AH, Flynn KF, Glendenin LE, Bentley WT., Essling AM (1971) Precision measurement of half-lives and specific activities of ^{235}U and ^{238}U. Phys Rev C 4:1889

Janecky, D.R., Seyfried, W.E., 1984. Formation of massive sulfide deposits on oceanic ridge crests: Incremental reaction models for mixing between hydrothermal solutions and seawater. Geochim. Cosmochim. Ac 48, 2723–2738.

Johnson JW, Oelkers EH, Helgeson HC (1992) SUPCRT92: A software package for calculating the standard molal thermodynamic properties of minerals, gases, aqueous species, and reactions from 1 to 5000 bar and 0 to 1000 C. Comput Geosci 18:899–947

Jupp TE, Schultz A (2004) Physical balances in subseafloor hydrothermal convection cells. J Geophys Res-Sol Earth 109(B5)

Klein F, Bach W, Jöns N, McCollom T, Moskowitz B, Berquó T (2009) Iron partitioning and hydrogen generation during serpentinization of abyssal peridotites from 15 N on the Mid-Atlantic Ridge. Geochim Cosmochim Ac 73:6868–6893

Le Roux LJ, Glendenin LE (1963). Half-life of 232Th. In: Proceedings of the National Meeting on Nuclear Energy: Application of Isotopes and Radiation, Pretoria, pp 83–94

Lombardo B, Pognante U (1982) Tectonic implications in the evolution of the Western Alps ophiolite metagabbros. Ofioliti 2:371–394

Lombardo B, Rubatto D, Castelli D (2002) Ion microprobe U-Pb dating of zircon from a Monviso metaplagiogranite: implications for the evolution of the Piedmont-Liguria Tethys in the Western Alps. Ofioliti 27:109–117

Ludwig K. R. (2012) User's manual for ISOPLOT 3.75, a geochronological toolkit for Microsoft Excel. Berkeley Geochronology Center, Spec. Pub. 5

Manatschal G, Müntener O (2009) A type sequence across an ancient magma-poor ocean–continent transition: the example of the western Alpine Tethys ophiolites. Tectonophysics 473:4–19

Manatschal G, Sauter D, Karpoff AM, Masini E, Mohn G, Lagabrielle Y (2011) The Chenaillet Ophiolite in the French/Italian Alps: an ancient analogue for an oceanic core complex? Lithos 124:169–184

Marques AFA (2005) Geology and genesis of sulfide mineralization in the Rainbow ultramafic-hosted seafloor hydrothermal system. Dissertation, University of Lisbon

Marques AFA, Barriga FJ, Chavagnac V, Fouquet Y (2006) Mineralogy, geochemistry, and Nd isotope composition of the Rainbow hydrothermal field, Mid-Atlantic Ridge. Miner Deposita 41:52–67

Marques AFA, Barriga FJ, Scott SD (2007) Sulfide mineralization in an ultramafic-rock hosted seafloor hydrothermal system: From serpentinization to the formation of Cu–Zn–(Co)-rich massive sulfides. Mar Geol 245:20–39

Martin S, Rebay G, Kienast J, Mével C (2008) An eclogitised oceanic palaeo-hydrothermal field from the St. Marcel Valley (Italian Western Alps). Ofioliti 33:49–63

McCaig AM, Cliff RA, Escartin J, Fallick AE, MacLeod CJ (2007) Oceanic detachment faults focus very large volumes of black smoker fluids. Geology 35:935–938

McDonough WF, Sun S (1995) The composition of the Earth. Chem Geol 120:223–253

Melekestseva IY, Zaykov VV, Nimis P, Tret'yakov GA, Tessalina SG (2013) Cu–(Ni–Co–Au)-bearing massive sulfide deposits associated with mafic–ultramafic rocks of the Main Urals Fault,

South Urals: Geological structures, ore textural and mineralogical features, comparison with modern analogs. Ore Geol Rev 52:18–36

Melekestseva IY, Tret'yakov GA, Nimis P, Yuminov AM, Maslennikov VV, Maslennikova SP, Kotlyarov VA, Beltenev VE, Danyushevsky LV, Large R (2014) Barite-rich massive sulfides from the Semenov-1 hydrothermal field (Mid-Atlantic Ridge, 13°30.87'N): Evidence for phase separation and magmatic input. Mar Geol 349:37–54

Mellini M, Rumori C, Viti C (2005) Hydrothermally reset magmatic spinels in retrograde serpentinites: formation of "ferritchromit" rims and chlorite aureoles. Contrib Mineral Petr 149:266–275

Merlini A, Grieco G, Diella V (2009) Ferritchromite and chromian-chlorite formation in mélange-hosted Kalkan chromitite (Southern Urals, Russia). Am Mineral 94:1459–1467

Mével C (2003) Serpentinization of abyssal peridotites at mid-ocean ridges. C R Geosci 335:825–852

Montel JM, Foret S, Veschambre M, Nicollet C, Provost A (1996) Electron microprobe dating of monazite. Chem Geol 131:37–53

Nadoll P, Koenig AE (2011) LA-ICP-MS of magnetite: methods and reference materials. J Anal Atom Spectrom 26:1872–1877

Nadoll P, Angerer T, Mauk JL, French D, Walshe J (2014) The chemistry of hydrothermal magnetite: a review. Ore Geol Rev 61:1–32

Nadoll P, Mauk JL, Leveille RA, Koenig AE (2015) Geochemistry of magnetite from porphyry Cu and skarn deposits in the southwestern United States. Miner Deposita 50:493–515

Niu Y (2004) Bulk-rock major and trace element compositions of abyssal peridotites: implications for mantle melting, melt extraction and post-melting processes beneath mid-ocean ridges. J Petrol 45:2423–2458

O'Neill HSC, Palme H (1998) Composition of the silicate Earth: implications for accretion and core formation. In: Jackson I (ed) The Earth's mantle: composition, structure and evolution, Cambridge University Press, pp. 3–126

Panseri M, Fontana E, Tartarotti P (2008) Evolution of rodingitic dykes: metasomatism and metamorphism in the Mount Avic serpentinites (Alpine Ophiolites, southern Aosta Valley). Ofioliti, 33:165–185

Paraskevopoulos GM, Economou M (1980) Genesis of magnetite ore occurrences by metasomatism of chromite ores in Greece. Neues Jb Miner Abh 140:29–53

Paulick H, Bach W, Godard M., De Hoog JCM, Suhr G, Harvey J (2006) Geochemistry of abyssal peridotites (Mid-Atlantic Ridge, 15 20′ N, ODP Leg 209): implications for fluid/rock interaction in slow spreading environments. Chem Geol 234:179–210

Pester NJ, Ding K, Seyfried WE (2014) Magmatic eruptions and iron volatility in deep-sea hydrothermal fluids. Geology 42:255–258

Piccardo, G-B. (2008) The Jurassic Ligurian Tethys, a fossil ultraslow-spreading ocean: the mantle perspective. In: Coltorti M, Grégoire M (Eds) Metamorphism in oceanic and continental lithospheric mantle. Geological Society, London, Special Publication, vol. 293, pp. 11–33

Polino R, Martin S, Malusà M, Mosca P, Bonetto F, Baggio P, Baster I, Bertolo D, Carraro F, Fontan D, Gianotti F, Monopoli B, Perello P, Schiavo A, Venturini G, Vuillermoz R (2014) Note illustrative della carta geologica d'Italia alla scala 1:50.000 Aosta F. 90. Ispra-Servizio Geologico d'Italia

Puteanus D, Glasby GP, Stoffers P, Kunzendorf H (1991) Hydrothermal iron-rich deposits from the Teahitia-Mehitia and Macdonald hot spot areas, Southwest Pacific. Mar Geol 98:389–409

Renna MR, Tribuzio R (2011) Olivine-rich troctolites from Ligurian ophiolites (Italy): evidence for impregnation of replacive mantle conduits by MORB-type melts. J Petrol 52:1763–1790

Rollinson H (1993) Using geochemical data. Longman, London

Rona PA (1988) Hydrothermal mineralization at oceanic ridges. Can Mineral 26:431–465

Rossetti P, Gatta GD, Diella V, Carbonin S, Della Giusta A, Ferrario A (2009) The magnetite ore districts of the southern Aosta Valley (Western Alps, Italy): a mineralogical study of metasomatized chromite ore. Mineral Mag 73:737–751

Routhier P (1963) Les gisements métallifères: géologie et principes de recherche. Masson, Paris

Sanfilippo A, Tribuzio R, Tiepolo M (2014) Mantle–crust interactions in the oceanic lithosphere: Constraints from minor and trace elements in olivine. Geochim Cosmochim Ac 141:423–439

Sawyer GM, Oppenheimer C, Tsanev VI, Yirgu G (2008) Magmatic degassing at Erta'Ale volcano, Ethiopia. J Volcanol Geoth Res 178:837–846

Schmid SM, Fügenschuh B, Kissling E, Schuster R (2004) Tectonic map and overall architecture of the Alpine orogen. Eclogae Geol Helv 97:93–117

Schwartz S, Guillot S, Reynard B, Lafay R, Debret B, Nicollet C, Lanari P, Auzende AL (2013) Pressure–temperature estimates of the lizardite/antigorite transition in high pressure serpentinites. Lithos 178:197–210

Seyfried Jr WE (1987) Experimental and theoretical constraints on hydrothermal alteration processes at mid-ocean ridges. Annu Rev Earth Pl Sc 15:317

Seyfried WE, Foustoukos DI, Allen DE (2004) Ultramafic-hosted hydrothermal systems at mid-ocean ridges: chemical and physical controls on pH, redox and carbon reduction reactions. In: German CR, Lin J, Parson LM (eds) Mid-ocean ridges: hydrothermal interactions between the lithosphere and oceans, American Geophysical Union, Washington, DC, pp. 267–284

Seyfried WE, Pester N, Fu Q (2010) Phase equilibria controls on the chemistry of vent fluids from hydrothermal systems on slow spreading ridges: reactivity of plagioclase and olivine solid solutions and the pH-silica connection. In: Rona PA, Devey CW, Dyment J, Murton BJ (eds) Diversity of hydrothermal systems on slow spreading ocean ridges, American Geophysical Union, Washington, DC, pp. 297-320

Seyfried WE, Pester NJ, Ding K, Rough M (2011) Vent fluid chemistry of the Rainbow hydrothermal system (36 N, MAR): phase equilibria and in situ pH controls on subseafloor alteration processes. Geochim Cosmochim Ac 75:1574–1593

Singh SC, Crawford WC, Carton H, Seher T, Combier V, Cannat M, Canales JP, Düsünür D, Escartin J, Miranda JM (2006). Discovery of a magma chamber and faults beneath a Mid-Atlantic Ridge hydrothermal field. Nature 442:1029–1032

Suhr G, Hellebrand E, Johnson K, Brunelli D (2008) Stacked gabbro units and intervening mantle: A detailed look at a section of IODP Leg 305, Hole U1309D. Geochem Geophy Geosy 9

Szitkar F, Dyment J, Fouquet Y, Honsho C, Horen H (2014) The magnetic signature of ultramafic-hosted hydrothermal sites. Geology 42:715–718

Stella A (1916) Le miniere di Cogne (Val d'Aosta). S.A.I.G. A. Barabino, Genova

Stella A (1921) Le miniere di ferro d'Italia. Lattes, Torino.

Tartarotti P, Festa A, Benciolini L, Balestro G (2015) Mantle-cover sequence in the Western Alps metaophiolites: a key to recognize remnants of an exhumed Oceanic Core Complex (OCC). Rend Online Soc Geol It, Suppl. n. 2, Vol. 35

Templ M, Hron K, Filzmoser P (2011) robCompositions: an R-package for robust statistical analysis of compositional data. In: Pawlowsky-Glahn V, Buccianti A (Eds.), Compositional Data Analysis. Theory and Applications. John Wiley & Sons, Chichester (UK), pp. 341–355.

Tivey MA, Dyment J (2010) The magnetic signature of hydrothermal systems in slow spreading environments. In: Diversity of Hydrothermal Systems on Slow Spreading Ocean Ridges. In: Rona PA, Devey CW, Dyment J, Murton BJ (eds) Diversity of hydrothermal systems on slow spreading ocean ridges, American Geophysical Union, Washington, DC, pp. 43–66

Tumiati S, Martin S, Godard G (2010) Hydrothermal origin of manganese in the high-pressure ophiolite metasediments of Praborna ore deposit (Aosta Valley, Western Alps). Eur J Mineral 22:577–594

Tumiati S, Godard G, Martin S, Malaspina N, Poli S (2015) Ultra-oxidized rocks in subduction mélanges? Decoupling between oxygen fugacity and oxygen availability in a Mn-rich metasomatic environment. Lithos 226:116–130

Von Damm KL (2004) Evolution of the hydrothermal system at East Pacific Rise 9°50'N: geochemical evidence for changes in the upper oceanic crust. In: German CR, Lin J, Parson LM (eds) Mid-ocean ridges: hydrothermal interactions between the lithosphere and oceans, American Geophysical Union, Washington, DC, pp. 285–304

Werner CD (1997). Data report: geochemistry of rocks and minerals of the gabbro complex from the Kane area (MARK). In: Karson JA, Cannat M, Miller DJ, Elthon D (eds) Proceedings of the Ocean Drilling Program. Scientific Results (Vol. 153). Ocean Drilling Program, pp. 457–470

Whitney DL, Evans BW (2010) Abbreviations for names of rock-forming minerals. Am Mineral 95:185–187

Wolery TJ, Jarek RL (2003) Software User's Manual EQ3/6 (Version 8.0). Sandia National Laboratories, Albuquerque, New Mexico

Wolery TJ (2013) EQ3/6 - Software for Geochemical Modeling, Version 8.0a. Lawrence Livermore National Laboratory, Livermore, California

Yıldırım N, Dönmez C, Kang J, Lee I, Pirajno F, Yıldırım E, Günay K, Seo JH, Farquhar J, Chang, SW (2016) A magnetite-rich Cyprus-type VMS deposit in Ortaklar: A unique VMS style in the Tethyan metallogenic belt, Gaziantep, Turkey. Ore Geol Rev 79:425–442

Appendix

List of samples

Sample	Locality	Rock type	Mineral assemblage (gangue for magnetite ores)	Inclusions	Deformation style	Additional information
CO1	SITE1	Brecciated massive magnetite ore	Mag, Atg, Lz (vein), rare Sp and Apy in Srp vein	Srp, Brc, Po in Mag	Cataclasis	Lz veins
CO2	SITE1	Massive magnetite ore	Mag, Atg, Brc, Fo	Atg, Brc in Mag	Faint foliation	
CO4	SITE1	Marble with clasts of serpentinite (footwall of the deposit)	Cal, Atg		Cataclasis	
CO5	SITE1	Coarse grained leopard magnetite ore	Mag, Atg, Lz, Fo, Brc, Clc	Atg, Brc, Clc, Cal, Lz, very rare Po in Mag	Cataclasis (fractured magnetite nodules)	
CO6	SITE1	Fine-grained leopard magnetite ore	Mag, Atg, Fo, Brc	Atg, Brc, Clc, rare Fo in Mag	Cataclasis (fractured magnetite nodules)	Lz veins
CO7	SITE1	Fine-grained leopard magnetite ore	Mag, Atg, rare Po	Atg, Brc, Clc in Mag	Cataclasis (fractured Mag nodules)	Lz + Brc veins
CO8	SITE1	Rodingite (hangingwall of the deposit)	Di, Grs, Czo, Cal		Cataclasis	Cal veins
CO9	SITE1	Marble (footwall of the deposit)	Cal		Dynamic recrystallization	
CO10	SITE1	Fine-grained leopard magnetite ore	Mag, Atg, Cal, rare Ap, sulphides	Atg, Brc, Clc in Mag	nd	Late Cal impregnations
CO11	SITE1	Brucite rock including a band of leopard magnetite ore	Brc; Mag , Atg, Fo, rare Cal in the ore	Atg, Brc, rare Fo in Mag	Foliation	
CO12	SITE1	Massive magnetite ore	Mag, Atg, Lz, Fo, rare Cc, Clc	Atg, Brc, Clc, Fo, Lz, sulphides, very rare Urn in Mag	Foliation	
CO13	SITE1	Rodingite (hangingwall of the deposit)	Cal, Grs, Di, Czo, rare Ap, Ttn, Po, Py		Foliation	
CO14	SITE1	Mag-rich diopsidite	Mag, Di, Atg, Di, Adr, Cal, rare Chl	Clc, Adr, Atg, Cal, rare Ap in Mag	nd	Atg + Adr replace Di; late Cal veins and impregnations
CO15	SITE1	Massive Mag-poor serpentinized peridotite	Mesh-textured Lz, Atg, Mag, Mg-Al-Chr, sulphides (Py, Po, Pn)	Chl in Mg-Al-Chr relicts	nd	Mesh texture and bastites
CO16	SITE1	Mag ore	Mag, Atg, Fo, Lz	Atg, Fo in Mag	Strong foliation	
LICONI	SITE1	Leopard ore	Mag, Atg, Fo, Lz, Clc, very rare Xtm and Ap	Atg, Brc, Clc, Cal very rare Urn, Xtm in Mag	Cataclasis (fractured Mag nodules)	
LIC1A	SITE1	Rodingite (hangingwall of the deposit)	Di, Chl, Cal, Atg		Strong foliation and folding; late Cal veins	
LIC1B	SITE1	Mag poor serpentinized peridotite in contact with LIC1A	Atg, Mag		Strong foliation and folding; late Cal veins	
LIC2	SITE1	Calcschist (hangingwall of the deposit)	Qtz, Cal, Ab, white mica, Chl, Ttn	Gr inclusions in Ab	Strong foliation and folding	
LIC3	SITE1	Leopard ore with variable texture	Not cut			
LIC4	SITE1	Tremolitite with Py blasts	Tr, Tlc, Chl, Py,	Ccp and Bn inclusions in Py	Lineation	
LIC5	SITE1	Tremolitite with Py blasts	Tr, Tlc, Py, Ccp	Ccp and Mag inclusion in Py	Lineation	
LIC6	SITE1	Rodingite (hangingwall of the deposit)	Grs, Di, Ep, Cal, Py, rare Ccp	Ccp, Bn and Mag inclusions in Py	Cataclasis	
LIC7	SITE1	Rodingite (hangingwall of the deposit)	Ep, Cal, Di, Ttn		Cataclasis	Late Cal veins
LIC8	SITE1	Cal + Brc + Ti-Chn vein in serpentinite	Vein: Cal, Brc, Ti-Chn, rare Mag and Py; Serpentinite: Atg, Mag	Po in Mag; Bn and Ccp in Py		Late Lz vein
LIC9	SITE1	Massive magnetite ore	Mag, Tr, Py, Tlc	Mag, Ccp, Bn in Py; Clc in Mag	Foliation	
LIC12	SITE1	Massive Mag-poor serpentinized peridotite	Lz, Atg, Mag, Mg-Al-Chr, sulphides (Py, Po, Pn), Tlc			Mesh texture and bastites
LIC13	SITE1	Massive Mag-poor serpentinite	Atg, Cal, rare Mag			
LIC14	SITE1	Harrisitic magnetite ore	Mag, Atg, Fo, Lz, Brc, Cb (Cal, Dol, Mgs), Clc, rare Ti-Chn, very rare Xtm and Ap	Atg, Brc, Clc, Cal, rare Po, Sp, Ap and Urn in Mag	Faint foliation	
LIC15	SITE1	Leopard magnetite ore	Mag, Atg, Lz, Cal	Atg, Brc, Clc, Cal in Mag		Late Cal veins and impregantions
LIC16	SITE1	Leopard magnetite ore	Mag, Atg, Fo, Lz, Brc, Clc, rare Ti-Chn, very rare Xtm and Ap	Atg, Brc, Clc, Cal, rare Sp, very rare Urn in Mag		
LIC17	SITE1	Leopard to massive magnetite ore	Mag, Atg, Fo, Lz, Brc	Atg, Brc, Clc, Cal in Mag	Faint foliation	Late Cal veins
FLIC2	SITE1	Massive serpentinite	Lz, Atg, Mag, rare sulphides			Srp veins
FLIC9	SITE1	Leopard magnetite ore	Mag, Atg, rare sulphides		Foliation	
CDP1	SITE1	Marble with quartz bands (footwall of the deposit)	Cal, Qtz			
CDP2	SITE1	Prasinite (footwall of the deposit)	Chl, Ab, Ep, Hem, rare white mica	Chl, Ep in Ab	Strong foliation	
CDP7	SITE1	Leopard magnetite ore	Mag, Atg, Fo, Lz, Clc, Po	Atg, Brc, Clc, rare Urn in Mag		Anti-nodular texture
CDP10	SITE1	Massive magnetite ore	Mag, Atg, Lz	Atg, Brc, Clc in Mag	Faint foliation	
CDP15	SITE1	Mag-poor pegmatoid serpentinite	Atg, Lz, Mag, Po			Interlobate Atg and Atg + Lz + Mag domains with Atg coronae
MZ18	SITE1	Mag-poor pegmatoid serpentinite	Atg, Lz, Mag			Interlobate Atg + Lz and Atg + Lz + Mag domains with Atg coronae
CRY1	SITE2	Mag + Ccp vein in serpentinte	Mag, Atg, Ccp	Ccp, Po, Bn, Co-Pn, Sp, Chl, Adr in Mag; Mag in Ccp		

CRY2	SITE2	Mag + Ccp vein in serpentinte	Mag, Atg, Ccp	Ccp, Po, Bn, Co-Pn, Sp, Chl, Adr in Mag; Mag in Ccp		
CRY3	SITE2	Clinopyroxenite boudin in serpentinized peridotite	Cpx, Atg, Di (II), Adr, Chl, Ti-Chu, rare sulphides (Po, Pn)			Late Lz + Mag veins, Adr + Mag + Di (II) form along cleavages and fractures of Cpx
MZL1	SITE2	Mag + Ccp vein in serpentinte	Mag, Atg, Ccp in the vein; Atg, Lz, rare Di in the host serpentinite	Ccp, Po, Bn, Co-Pn, Sp, Chl, Adr in Mag; Mag in Ccp		
MZL2 (two samples)	SITE2	Mag-poor serpentinite	Lz, Atg, Mag, Tlc		Foliation	Late Srp veins
MZL3 (two samples)	SITE2	Massive magnetite impregnation ore	Mag, Atg, Di, Lz, sulphides (altere			Srp pseudomorphs after silicates preserved in Mag
MZL4 (two samples)	SITE2	Mag-impregnated serpentinite close to Mag + Ccp vein	Mag, Atg, Lz, Di, rare Chr	Ccp in Mag		Srp pseudomorphs after silicates preserved in Mag
ECL1	SITE2	Mag-impregnted serpentinite	Mag, Atg, Di, Lz, Mg-Al-Chr	Atg and Di in Mag	Foliation	Chl bands concordant with schistosity; Atg pseudomorphs after silicates; Mg-Al-Chr altered to Fe-Chr + Chl and Chl + Mag
ECL6	SITE2	Mag-poor serpentinized peridotite	Atg, Mt, Po		Foliation	Bastites
CGN3	SITE3	Di-rich leopard magnetite ore	Mag, Di, Clc, Atg	Clc, Adr and very rare Urn in Mag; Mag, Adr in Di	Foliation	Late Atg veins
CGN8	SITE3	Leopard magnetite ore	Mag, Atg, rare Tlc	Atg, Adr, very rare Di in Mag	Foliation	
LAR1	SITE3	Boudin of leopard magnetite ore in Mag-poor serpentinized preidotite	Mag, Atg in the boudin; Atg, Lz, Mag in the serpentinite		Foliation	Bastite texture in the peridotite
LAR2A	SITE3	Mag-rich pegmatoid serpentinite	Atg, Lz, Mag, Clc, Di	Atg, Clc inclusions in Mag		Interlobate Atg and Lz + Atg+ Clc + Mag domains with Atg coronae; late Lz + Di veins
LAR2B	SITE3	Mag-rich pegmatoid serpentinite	Atg, Lz, Mag, Clc, Di, rare Ap	Atg, Clc, Lz inclusions in Mag; Mag, Atg in Di		Interlobate Atg and Lz + Atg+ Clc + Mag domains with Atg coronae; late Lz + Di veins; two Mag generations
LAR2C	SITE3	Mag-rich diopsidite in contact with Mag-rich pegmatoid serpentinite (LAR2B)	Mag, Di, Atg, rare Adr		Foliation	
LAR3	SITE3	Di-rich leopard magnetite ore	Mag, Di, Atg	Atg, Di and very rare sulphides in Mag; Mag in Di		Late Lz + Di veins
LAR4A	SITE3	Mag-poor serpentinized peridotite	Atg, Mag, Chl,		Foliation	Bastites
LAR4B	SITE3	Marble in contact with LAR4A	Cal, Atg		Foliation, dynamic recrystallization of Cal	
LAR5	SITE3	Leopard ore crosscut by a 3 cm-thick Di vein	Mag, Atg, Clc in the ore; Di, Lz, Clc, Mag, rare Ttn in the vein		Shear deformation	Vein selvage made of fine-grained Di + Atg
LAR6	SITE3	Massive Mag-poor serpentinized peridotite	Atg, Lz, Mag, Cal		Foliation	Mesh texture and bastites; late Cal impregantions and veins
LAR7	SITE3	Fibrous serpentinite in carbonate-rich shear zone in massive ore	Atg, Cal; Mag, Atg, Chl in the ore	Atg, Chl in Mag	Strong foliation	Late Cal impregnations
LAR8	SITE3	Mag-rich diopsidite	Di, Mag, Atg, Clc, Lz, Adr	Mag, Adr in Di; Atg, Clc in Mag		Late Lz + Di ± Mag veins
LAR9	SITE3	Diopsidite vein in contact with Mag-rich serpentinite	Di, Lz, Mag in the vein; Mag, Atg, Clc in the serpentinite			Vein selvage made of fine-grained Di + Atg
LAR10	SITE3	Mag-poor schistose serpentinite	Atg, Mag, Chr		Strong foliation	
LAR11	SITE3	Leopard magnetite ore	Mag, Atg		Faint foliation	Lobate domains with Atg coronae recognizable